Magnons and Phonons in Nanostructures



Alex D Carr, MPHYS
School of Physics and Astronomy
University of Nottingham

Thesis submitted to the
University of Nottingham
for the degree of

Doctor of Philosophy

December 2025

Acknowledgements

I want to thank my supervisor, Dr Andrew Rushforth, for his invaluable assistance throughout my PhD, from providing ideas and support to my writing, experimental design, device fabrication, and theoretical understanding. I also need to thank Dr Sarah Heywood for all her help with sample fabrication and for being the postdoc on my project; without her, I think I would still be in the cleanroom to this day. I also want to thank the team at E2 Technical University of Dortmund, specifically Dr Alexey Scherbakov, Dr Tatiana Linnik, and Dr Anton Samusev, for their support during my time in Germany and for helping me become familiar with pump-probe time-resolved experiments. On the note of pump-probe experiments, I'd also like to thank Dr Anthony Kent and Dr Andrey Akimov of the Nottingham THz Acoustics group for their help with manuscript preparation and, ultimately, for allowing me to use their pump-probe kit.

I want to thank my friends in the spintronics office for many fruitful discussions and for broadening my coffee and beer horizons; thank you, Alfred, Ollie, and Stu. My friends outside of work have also helped keep me grounded and allowed me to rest in my free time, whether by inviting me to come up to Wakefield for a weekend or just down to the local pub for a few pints. Thank you, Pip, Lars, Callum and Tash.

Finally, the last few people who need to be thanked include my wonderfully supportive girlfriend, Vick, who always listens, even when she has no idea what I'm talking about, and then helps me find the right words to explain it better. And my parents, Donna and Adrian, for putting up with me living at home for the past four years (although I think my acting as a personal chef and living in the garden makes up for this) and for all the support a parent generally provides to their children.

Publications

A. V. Scherbakov, **A. D. Carr**, T. L. Linnik, S. M. Kukhtaruk, A. D. Armour, A. Nadzeyka, A. W. Rushforth, A. V. Akimov, M. Bayer. Hybrid coherent control of magnons in a ferromagnetic phononic resonator excited by laser pulses. *Physical Review Research*, 6(1):L012019,2024.

A. D. Carr, C. Ruppert, A. K. Samusev, G. Magnabosco, N. Vogel, T. L. Linnik, A. W. Rushforth, M. Bayer, A. V. Scherbakov, A. V. Akimov. Enhanced Photon–Phonon Interaction in WSe2 Acoustic Nanocavities. *ACS photonics*, 11(3):1147-1155.

Conferences

The 17^{th} International Conference on Phonon Scattering in Condensed Matter (2023), Paris, France. Poster: 'Interference of Magnons Excited by Coherent Phonons and Ultrafast Spin Torque'

2^{nd} Transnational Round Table on Magnonics, High-Frequency Spintronics and Ultrafast Magnetism (2025), Exeter, UK. 45 min oral presentation: 'Hybrid coherent control of magnons in a ferromagnetic phononic resonator excited by laser pulses'

Abstract

Coupling between quantum systems allows for the discovery of interference-based effects in materials or between different systems, including Fano interferences and amplification due to constructive interference. Strong coupling is a regime in which interacting quasiparticles can exchange energy coherently, with potential applications in quantum computing for manipulation and for extending the decoherence time. To be useful for application, these devices need to be fabricated on-chip. In this thesis, the coupling between magnons and phonons and between phonons and excitons is investigated in nanoscale systems fabricated on-chip.

For the magnon-phonon coupling, the material of interest is Galfenol, which is chosen due to its high magnetostriction coefficient of 395 ppm and ease of growth and device fabrication. A nanograting with a trough depth of 7 nm, a width of 48 nm, and a period of 120 nm is fabricated in a 20 nm thick Galfenol layer such that the excited magnon and phonon modes are spatially confined and overlap, and have similar frequencies. The device can then be excited optically via a pump laser with a wavelength of 1050 nm and probed by a probe laser with a wavelength of 780nm, enabling the use of the polar magneto-optical Kerr effect and the photoelastic effect to observe magnons and phonons, respectively. Using the polar magneto-optical Kerr effect and increasing the external magnetic field from 200 mT t0 400 mT in 10 mT steps, the dynamics of magnons are investigated, including the magnon-phonon interaction. It is observed that at high pump laser fluence (10 mJ/cm^2) the magnon-phonon interaction exhibits a Fano-like interference effect which is controllable by adjusting the pump laser fluence.

Alternatively, the device can be electrically excited via a microwave antenna which operates at frequencies between 10 to 20 GHz, and the microwaves generated have a power of 18 dBm. The microwave-generated magnons are then detected via the inverse spin Hall effect. In this work, the magnon spectra change with the orientation of the external field relative to the Galfenol bar, with measured orientations of 0°, 45° and 90°. The origins of this spectral change are explored, including the localisation of different magnon modes within the bar; this was achieved using Ubermag to simulate the magnons.

This thesis also explores the coupling of phonons and excitons, where the material of choice is WSe_2, which is a transition metal dichalcogenide and a van der Waals material. This material is chosen because the direct exciton resonance (1.62 eV) is close in energy

to the probe laser photon energy (1.60 eV). This results in amplification of the phonon resonance via the photoelastic effect, which depends on the exciton resonance and the Bragg condition.

Contents

1 Introduction and Overview **1**
- 1.1 Introduction . . . 1
- 1.2 Overview . . . 2
- 1.3 Magnetic Phenomena . . . 3
  - 1.3.1 Ferromagnetism . . . 4
  - 1.3.2 Exchange . . . 5
  - 1.3.3 Spin Orbit Coupling . . . 6
  - 1.3.4 Magnetocrystalline Anisotropy . . . 7
  - 1.3.5 Anistropic Magnetoresistance . . . 10
  - 1.3.6 Magnetostriction . . . 11
  - 1.3.7 Spin Current . . . 15
  - 1.3.8 Inverse Spin Hall Effect . . . 15
  - 1.3.9 Magneto-Optical Kerr effect . . . 16
- 1.4 Micromagnetism . . . 20
  - 1.4.1 Landau-Lifshitz-Gilbert Equation . . . 21
  - 1.4.2 Magnetic Free Energy Density . . . 21
  - 1.4.3 Simulation . . . 22
- 1.5 Quasiparticles . . . 23
  - 1.5.1 Magnons . . . 23
  - 1.5.2 Phonons . . . 31
  - 1.5.3 Excitons . . . 34
  - 1.5.4 Coupling . . . 35
- 1.6 Fano Resonance . . . 36
- 1.7 ASOPS . . . 37
- 1.8 Current Works in Magnon-Phonon and Phonon-Exciton Coupling . . . 39

2 Fano-like Interference Effects in a Coupled Magnon-Phonon Resonator **45**
- 2.1 Introduction . . . 45
- 2.2 Methods . . . 46
  - 2.2.1 Set-up . . . 46
  - 2.2.2 Materials . . . 49
  - 2.2.3 Techniques . . . 50
- 2.3 Results . . . 52
- 2.4 Simulation and Modelling of Rayleigh Waves and Magnon Modes in Galfenol Nanogratings . . . 58
- 2.5 Conclusion . . . 68

3 Enhanced Phonon-Photon Interaction in Acoustic Nanocavities **70**
3.1 Introduction . . . 70
3.2 Current Works in Phonon Nanocavities . . . 72
3.3 Methods . . . 74
3.3.1 Setup . . . 74
3.3.2 Materials . . . 75
3.3.3 Techniques . . . 78
3.4 Results . . . 80
3.5 Simulation and Modelling of the Amplitude of Longitudinal Phonon Modes in WSe_2 . . . 85
3.6 Conclusion . . . 90

4 Electrical Excitation and Detection of Magnons **92**
4.1 Introduction . . . 92
4.2 Methods . . . 93
4.2.1 Setup . . . 93
4.2.2 Materials and Devices . . . 95
4.3 Results . . . 99
4.3.1 Data Analysis . . . 99
4.3.2 Simulations . . . 118
4.4 Classifying the Origin and Type of Magnon Modes Observed Within 3 μm Galfenol Bars . . . 122
4.5 Conclusion . . . 124

5 Conclusion **127**

References **129**

Appendix **153**

1 Introduction and Overview

1.1 Introduction

The strong strong coupling of quasiparticles is an area of interest due to the combined particle gaining properties of the composite particles, in the case of magnons the advantageous property is the ease of tunability with an external magnetic field, for phonons it is the potential for relatively long lifetimes (33 ns [1]) therefore strong coupling of magnons and phonons would produce tuneable long lifetime particles, which could be used for stable data storage in quantum computers. Furthermore, weak coupling of quasiparticles results in driving interactions that can produce novel interference-based effects, which can be used to amplify signals for improved detection and excitation.

This thesis presents three different investigations that explore phonons and magnons in nanostructures. To explore magnon systems, galfenol is used due to its high magnetostriction. This increases the coupling between the magnetisation and strain in the material, and therefore between magnons and phonons. To further improve the coupling between magnons and phonons in this material, nanostructures are produced to confine the phonon modes spatially and to define the phonon frequency. In these works, a nanograting milled into the galfenol surface is used, as well as a superlattice in which the galfenol film is deposited on top.

The work presented in Chapter 2 examined the optical excitation of magnons and phonons in a galfenol nanograting, using a pump-probe technique in which two lasers with different repetition rates asynchronously excite and probe the sample; this technique is known as asynchronous optical sampling (ASOPS). Using ASOPS, a Fano-like interference effect is observed that can be controlled by varying the pump laser fluence, with 10 mJ/cm^2 yielding the strongest interference.

In Chapter 3, phonons and excitons were investigated in flakes of the transition metal dichalcogenide WSe_2. These materials are also van der Waals materials, meaning that the interaction between the atomic layers is weak; therefore, different flake thicknesses can be readily exfoliated. To observe the phonons in these flakes, the asynchronous optical sampling technique is again utilised. In this work, the probe laser was tuned to an energy near the exciton resonance, resulting in two regions in which the phonon detection was amplified. The first region is for phonons with frequencies < 25 GHz; in this region, the Bragg condition, as well as the increase in the pho-

toelastic constant due to the proximity of the exciton resonance, enhances phonon detection. In the second region for phonons of frequencies > 60 GHz, the increased generation of excitons, driven by the decrease in the exciton energy band gap due to reduced layer thickness and strain, strongly amplifies the sensitivity of the phonon measurement.

Chapter 4 explores electrically excited magnons and phonons. In these works, both a galfenol nanograting and a superlattice with galfenol deposited on top are measured. The electrical excitation is provided by a microwave antenna fabricated in close proximity to the galfenol devices. In this work, only magnons were observed via the electrical excitation; however, an optical pump-probe measurement was done to observe the phonon modes. We did not observe any interaction between magnons and phonons, interactions between different magnon modes excited within the sample were observed; therefore, simulations were undertaken to explore the origin, location and type of these magnons.

1.2 Overview

This thesis is separated into three distinct investigation chapters, plus the introduction and conclusion chapters.

Chapter 1 examines the motivations for the work and the background physics of key phenomena and experimental techniques required for understanding this thesis. The chapter is further split into subchapters. The first is an introduction discussing ferromagnetism and its historical and present importance. The next section presents a literature review of the state of the field, specifically the coupling of magnons, phonons, and excitons in nanoscale structures. The following subchapter reviews important magnetic phenomena that are relevant to the material used, the phenomena investigated, and the experimental techniques applied. The subsequent three chapters describe the investigations carried out. Due to the distinct nature of each investigation, the relevant experimental methods have been described within each chapter. Where there is use of the same method in more than one chapter, the method is described in detail in one chapter, then cross-referenced in the subsequent chapter.

Chapter 2 discusses the use of the Asynchronous Optical Sampling (ASOPS) technique to detect and measure phonons and magnons and their interaction in a galfenol nanograting. This experiment observes a weak-coupling interaction in which the phonon-magnon system exhibits a Fano-like resonance, controlled by the fluence of the initial laser excitation pulse. The mechanisms behind this

interference-based effect are theoretically shown to be due to the ultrafast demagnetisation of the material and spin current-induced spin transfer torques.

Chapter 3 discusses the use of the ASOPS technique to explore the amplification of the reflectivity due to the increase of the photoelastic constants of multilayers of the TMD material, tungsten diselenide, when the probe laser photon energy approaches the direct exciton energy. This work shows that, across different phonon-frequency regimes, detection sensitivity varies with material and physical effects. In the phonon frequency range 10 - 30 GHz, the sensitivity of the phonon detection is directly controlled by the refractive index and photoelastic constant, and the Bragg condition for constructive interference of reflected light is satisfied. In the phonon frequency range greater than 60 GHz, excitons excited by the pump laser have a decrease in energy level due to the strain from the phonons. Since the excitons emit photons equal to their energy when they decay, the reflectivity of the photons from phonons is amplified by exciton decay. Therefore, this effect could theoretically allow for the detection of single phonons

Chapter 4 discusses the excitation of magnons and phonons in a galfenol nanograting via a microwave antenna using the inverse spin Hall effect and the anisotropic magnetoresistance (AMR). This chapter further delves into the different types of excited magnons, including Damon-Eshbach, backwards volume, and Kittel magnons, and their dependence on the sample geometry, the external field, and the excitation direction. Simulations were conducted to model the samples used and to explore the localisation and dominant interactions underlying the different magnon modes observed in the experimental data.

1.3 Magnetic Phenomena

Magnetic phenomena arise from the combined orbital and spin angular momenta of the electrons. When the net total angular momentum of an atom is non-zero, the atom is said to have an atomic magnetic moment [2]. In ferromagnetic materials, the exchange interaction leads to neighbouring magnetic moments aligning, which produces an ordered state. This net alignment allows for the magnetic material to create a magnetic field; the macroscopic alignment direction of the magnetic moments that produces the magnetic field is the magnetisation. The magnetisation is temperature dependent; when the temperature is raised above the critical Curie temperature, the ordered structure breaks down, and the net magnetisation

is reduced to zero. Further magnetic effects arise from the crystal symmetries of the material and produce favourable crystallographic axes for the magnetisation to align with.

1.3.1 Ferromagnetism

A ferromagnet is a material that, due to the net alignment of the magnetic moments, has a magnetisation, which produces an external magnetic field. The most common elemental ferromagnetic materials are iron, nickel and cobalt, although other ferromagnetic materials occur. Historically, ferromagnets have held great importance, with references to lodestones dating back to ancient Greece and China [3]; these lodestones were pivotal for navigation using compasses. Following this, during the Middle Ages, steel was widely used in forging to produce weapons such as swords and arrow tips [3]. Today, ferromagnetic materials play a vital role in our technological and scientific advancements.

In the 19^{th} century, due to advancements from the Industrial Revolution, a more thorough investigation into the origins of electromagnetism began [4]. Much of this early work is credited to Michael Faraday and his experimental observations, including that of electromagnetic induction [5]. Around the same time, Lord Kelvin observed that the resistance of magnetic materials changes depending on the axis of measurement [6]; this phenomenon later became known as anisotropic magnetoresistance (AMR), which set the basis of the field of spintronics, where both the spin and the charge of the electrons are used. Toward the latter end of the 19^{th} and beginning of the 20^{th} century, quantum mechanics began to explain the origins of magnetism [7], with Curie experimentally showing that ferromagnets undergo a phase change above a specific temperature known as the Curie temperature [8]. Ewing showed that magnetic materials experience hysteresis [9]. The theory was then developed by Langevin, resulting in a statistical framework to explain paramagnetism [10]. Next, Weiss developed his molecular field theory, which built on Langevin's ideas and included domain formation [11]. Heisenberg then derived the origin of the molecular field [12], leading to the exchange interaction. To further explain the magnetic properties of materials accurately, the energetics arising from the material's crystallographic structure must be accounted for. This was explored by Beck [13], Webster [14, 15] and Honda and Kaya [16].

Understanding the theory behind ferromagnetic materials enables the development of technologies that utilise them. These in-

clude magnetic sensing devices, such as AMR sensors [17], which were first designed in 1971 [18]. AMR sensors have a maximum information density of 5 Gb/in^2 [19]. GMR (giant magnetoresistance) sensors are the next iteration of this technology, which occurred in the 1990s [20] and have an information density of 100 Gb/in^2 [21]. TMR (tunnelling magnetoresistance) sensors are the most recent iteration of this type of device. Although discovered in 1975 [22], this discovery was made at low temperatures. More practical applications of this effect were demonstrated in 1995 [23]. These are used in readheads; with each iteration, the size of the readheads is reduced, allowing a greater storage density to be achieved.

There are also spin-valve devices called magnetic tunnel junctions (MTJs). MTJs utilise TMR to produce MTJ-TMR devices [24], in which the magnetisation of the free ferromagnetic layer serves as the bit. MTJs have produced information densities up to 300 Gb/in^2 [25]. MTJ-TMRs are used in hard drives and magnetoresistive random access memory (MRAM) [26], where MRAM stores binary information and, like RAM, must be accessed quickly. MRAM was first commercially available in 2006 [27]. Following this idea of minimising the size of these technologies leads to the concept of the quantisation of a spin wave, which is the magnon and is discussed in Chapter 1.5.1.

1.3.2 Exchange

The exchange energy defines the interaction between neighbouring electrons, causing their spins to be anti-aligned for anti-ferromagnets or aligned for ferromagnets, depending on whether the exchange integral is negative or positive, respectively. The energy takes the form:

$$E_{ex} = -2J\boldsymbol{s}_1 \cdot \boldsymbol{s}_2 \tag{1}$$

where J is the exchange integral, $\boldsymbol{s}_1$ and $\boldsymbol{s}_2$ are the spin operators of the two neighbouring electrons. A classical approximation can also be take which reduces the spin operators to classical angular momentum vectors with identical magnitudes this results in

$$E_{ex} = -2JS^2 cos(\phi) \tag{2}$$

where, S is the magnitude of the spin, and ϕ is the angle between the spins of neighbouring electrons.

Exchange energy has quantum mechanical origins [28, 29]. By exchanging two identical particles, we expect to see either no change in the wavefunction if the particles are bosons ($\psi(x_1, x_2) = \psi(x_2, x_1)$)

and a change in sign if the particles are fermions ($\psi(x_1, x_2) = -\psi(x_2, x_1)$). This implies that the wavefunction for fermions is antisymmetric, and for bosons, it is symmetric. Now, focusing only on the antisymmetric fermions the total wavefunction can be written as

$$\psi(x_1, x_2) = \psi_1(x_1)\psi_2(x_2) - \psi_1(x_2)\psi_2(x_1). \tag{3}$$

Each wavefunction, ψ_i can be further split into two parts: a spatial and a spin part. Each part can be symmetric or antisymmetric, but the overall wavefunction must be antisymmetric. Therefore, when the spatial part is symmetric (the electrons are in the same orbital), the spin part must be antisymmetric (the spins must be opposite) and vice versa. However, factoring in the Coulomb interaction between different orbitals means electrons fill separate orbitals within the subshell before filling an orbital, in order to reduce the Coulomb repulsion as explained through Hund's rule. The spin term, the spatial term and the Coulomb term can be used to formulate the Heisenberg Hamiltonian [30], which is given by

$$E = C - \frac{J}{2} - 2J\langle \boldsymbol{s}_1 \cdot \boldsymbol{s}_2 \rangle \tag{4}$$

The last term in this Hamiltonian is the exchange term. An exchange constant, A, can be introduced to characterise the strength of the coupling between the spins.

$$A = \frac{n}{a} J S^2 \tag{5}$$

n is the number of atoms per unit cell, and a is the lattice parameter.

1.3.3 Spin Orbit Coupling

Spin-orbit coupling (SOC) is a relativistic quantum mechanical effect that comes from the interaction between the spin and orbital angular momenta of an electron [2, 31]. SOC is observed by changing the reference frame of an atom from a static nucleus to the moving frame of the electron [32]. This change of reference frame induces an effective magnetic field that acts on the electron. The Lorentz transformation of the magnetic field produces the equation

$$\boldsymbol{B}_{eff} = \frac{\boldsymbol{\varepsilon} \times \boldsymbol{v}}{c^2}. \tag{6}$$

Here, $\boldsymbol{\varepsilon}$ is the electric field vector, $\boldsymbol{v}$ is the velocity of the nucleus and c is the speed of light. By using cylindrical coordinates, the electric field can be written as

$$\boldsymbol{\varepsilon} = -\nabla V(r) = -\frac{\boldsymbol{r}}{r}\frac{dV(r)}{dr}, \tag{7}$$

where V(r) is the electric potential as a function of position r. Substituting this and then using $\hbar \boldsymbol{L} = m_e \boldsymbol{r} \times \boldsymbol{v}$, where $\hbar$ is the reduced Planck's constant, m_e is the mass of the electron and $\boldsymbol{L}$ is the orbital angular momentum in unit of $\hbar$. produces an effective magnetic field of the form

$$\boldsymbol{B}_{eff} = -\frac{\hbar}{m_e r c^2} \frac{dV(r)}{dr} \boldsymbol{L} \tag{8}$$

This magnetic field and $\boldsymbol{m} = ge\hbar \boldsymbol{s}/2m_e$ modifies the Zeeman hamiltonian of the electron to become

$$\begin{aligned} H_{el} &= -\frac{1}{2} \boldsymbol{m} \cdot \boldsymbol{B}_{eff} \\ &= -\frac{1}{2} (\frac{ge\hbar}{2m_e} \boldsymbol{s}) \cdot (-\frac{\hbar}{r m_e c^2} \frac{dV(r)}{dr} \boldsymbol{L}) \\ &= \frac{ge\hbar^2}{4 r m_e^2 c^2} \frac{dV(r)}{dr} \boldsymbol{s} \cdot \boldsymbol{L}. \end{aligned} \tag{9}$$

Here, the factor of a half arrives due to the relativistic Thomas precession [33], and g is the Lande g-factor, which is approximately equal to 2 for the bare electron. g is also equal to 2 for the iron group salts. This is due to the crystal field produced between the magnetic electrons and the atomic ions, decoupling the orbital and spin angular momentum and also quenching the orbital angular momentum. This results in the total angular momentum being equal to the spin angular momentum only. [34] SOC is responsible for extra splitting in the electronic band structure and causes many magnetic phenomena, such as magnetocrystalline anisotropy [35], the spin hall effect and anisotropic magnetoresistance [36].

1.3.4 Magnetocrystalline Anisotropy

There are magnetic phenomena that result from the crystal structure of the material. There are two types of crystallographic anisotropies in the materials described in this thesis: uniaxial and cubic anisotropies. These are caused by SOC, and its effects on the Fermi surface [37], producing regions of high symmetry that are more or less energetically favourable. These regions are the easy and hard magnetic axes.

Uniaxial anisotropy is the result of there being one axis of high symmetry within the lattice; this is given by

$$E_{uni} = -K_u \cos^2(\theta) \quad [38] \tag{10}$$

Here, E_{uni} is the uniaxial magnetic free energy density of the system, K_u is the uniaxial anisotropy constant, and θ is the angle between

the easy axis and the magnetisation. Equation 10 can be reformulated to:

$$E = -K_u(\boldsymbol{m} \cdot \boldsymbol{u})^2 \tag{11}$$

Where here, $\boldsymbol{m}$ is the magnetic moment, and $\boldsymbol{u}$ is the direction of the easy axis. This form of the uniaxial anisotropy is typically used in micromagnetic simulations. However, this form of the equation illustrates the effect of uniaxial anisotropy on the magnetisation, as it encourages the alignment of the magnetisation and the easy axis direction.

Cubic anisotropy is similar to uniaxial anisotropy; however, in this case, there are three axes of high symmetry. Following a similar operation used above, the energy density of a system with this symmetry is given by:

$$\begin{aligned} E_{cubic} =& K_{c1}[(\boldsymbol{m} \cdot \boldsymbol{u_1})^2(\boldsymbol{m} \cdot \boldsymbol{u_2})^2 + (\boldsymbol{m} \cdot \boldsymbol{u_2})^2(\boldsymbol{m} \cdot \boldsymbol{u_3})^2 \\ &+(\boldsymbol{m} \cdot \boldsymbol{u_1})^2(\boldsymbol{m} \cdot \boldsymbol{u_3})^2] + K_{c2}[(\boldsymbol{m} \cdot \boldsymbol{u_1})^2(\boldsymbol{m} \cdot \boldsymbol{u_2})^2(\boldsymbol{m} \cdot \boldsymbol{u_3})^2]. \end{aligned} \tag{12}$$

E_{cubic} is the cubic magnetic free energy density, K_{c1} and K_{c2} are the cubic anisotropy constants, and $u_{1,2,3}$ are perpendicular axes, which are used to define the easy axes. To observe the effects of this energy, assume the easy axes are the x, y, and z directions, and the magnetisation first lies in the x direction; clearly, the energy is zero. Next, take the magnetisation to be [m,m,0]; the resultant energy is $E_{cubic} = K_{c1}m^4$, which, for $K_{c1} > 0$, requires more energy, suggesting that this term aligns the magnetisation along the easy axes. The cubic anisotropy can be written in terms of the direction cosines, which are the cosines of the angle between the crystal axes and the magnetisation, defined as $\alpha_i = \cos\theta = \boldsymbol{m} \cdot \boldsymbol{x_i}/|\boldsymbol{m}|$. This allows the cubic anisotropy energy to be written as

$$E_{cubic} = K_{c1}(\alpha_1^2\alpha_2^2 + \alpha_2^2\alpha_3^2 + \alpha_1^2\alpha_3^2) + K_{c2}(\alpha_1^2\alpha_2^2\alpha_3^2). \tag{13}$$

When using spherical coordinates, the direction cosines in the first term can be written as

$$E_{cubic} = K_{c1}(\frac{\sin^4(\theta)\sin^2(2\phi) + \sin^2(2\theta)}{4}). \tag{14}$$

Here, θ is the polar angle and ϕ is the azimuthal angle; this coordinate transformation is shown in Figure 1. Typically, a first-order term is sufficient, so the cubic anisotropy is written as

$$E_{cubic} = \frac{K_{c1}}{4}\sin^2(2\theta). \tag{15}$$

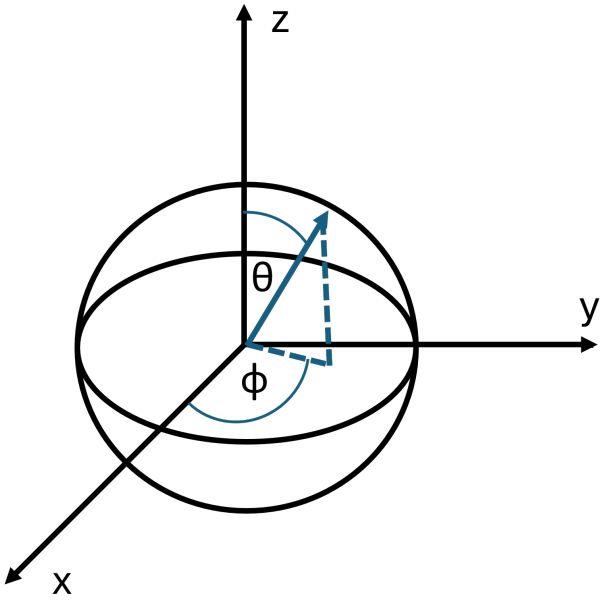


Figure 1: The coordinate system used to transform the cubic anisotropy from Cartesian to spherical. This coordinate transform allows for the first-order term in $\sin^2$ to be taken. Here the radius of the sphere is taken to be 1.

The samples used within these experiments have both uniaxial and cubic anisotropies, so the total magnetocrystalline magnetic free energy density term is

$$E = \frac{K_{c1}}{4} sin^2(2\theta) + K_u sin^2(\theta) \tag{16}$$

1.3.5 Anistropic Magnetoresistance

The fractional change of the electrical resistivity of a sample when a magnetic field is applied is given by

$$\frac{\Delta\rho}{\rho} = \frac{R(H) - R(0)}{R(0)} \tag{17}$$

where $\Delta\rho$ is the change in resistivity in the absence of a magnetic field, ρ is the resistivity, and R(H) is the resistance dependent on the magnetic field applied. Within ferromagnetic materials, this idea can be extended further, with magnetoresistance depending on the direction of the magnetisation with respect to the applied current. SOC is responsible for the anisotropic magnetoresistance (AMR) through its effects on the Fermi surface, density of states and scattering rates [37]. When the magnetisation and the spin of the conduction electrons are parallel or antiparallel, the scattering rate is maximised as the scattering rate is proportional to $|\boldsymbol{M} \cdot \boldsymbol{s}|$ [39, 40]. This understanding allowed Campbell, Fert and Jaoul to derive their formula for AMR.

$$\frac{\Delta\rho}{\rho} = \frac{\rho_{\parallel} - \rho_{\perp}}{\rho} \tag{18}$$

where $\rho_{\parallel}$ is the resistivity when the current is applied parallel to the magnetisation and $\rho_{\perp}$ is the resistivity when the current is applied perpendicular to the magnetisation.

Phenomenologically, the longitudinal AMR, ρ_{xx}, is shown to have non-crystalline components that give the traditional AMR. They can also have crystalline components due to symmetries in the crystal structure. The equation that factors in all these terms is [40]

$$\frac{\Delta\rho_{xx}}{\rho_{av}} = C_I cos(2\phi) + C_U cos(2\psi) + C_C cos(4\psi) + C_{I,C} cos(4\psi - 2\phi). \tag{19}$$

$\Delta\rho_{xx}$ is the difference between the longitudinal resistivity and the average resistivity, ρ_{av} is the averaged longitudinal resistivity over 360°, C_I, C_U, C_C and $C_{I,C}$ are the coefficients for each component

of the AMR, which are non-crystalline, uniaxial, cubic and a term which accounts for the interaction between the non-crystalline and the crystalline effects, respectively. ϕ is the angle between the current direction and the magnetisation, and ψ is the magnetisation angle from the [110] direction. S. Roy [41] has shown that for galfenol, the non-crystalline components dominate over the crystalline component by at least an order of magnitude; therefore, it's reasonable to discount the crystalline terms. The coefficients used for galfenol are $C_I = 0.02\%$ and $C_{I,C} = 0.14\%$ [41].

1.3.6 Magnetostriction

Magnetostriction is a phenomenon that occurs in magnetic materials, where the strain within the material changes when a magnetic field is applied. This is typically due to the crystal lattice of the material being distorted, caused by the rotation of the magnetisation and the rearrangement of the domain structure [42]. Therefore, since there is a saturation of the magnetisation, there is a maximum distortion reached at the saturation field; this is the saturation strain, λ_s. Magnetostriction is an anisotropic property of the material. For example, the $\langle 100 \rangle$ direction is an easy axis in galfenol with a corresponding λ_{100} value of 395 ppm [43] whereas, the $\langle 110 \rangle$ direction has a λ_{110} value of -16 ppm [43].

The strain within the material can be either compressive or tensile, which is reflected by the sign of the magnetostriction variable, with a negative corresponding to compressive strain and a positive to tensile strain. The inverse effect, known as the Villari effect [44], is also possible. This describes the change in magnetic anisotropy induced within the material when a strain is applied. The energy density contribution due to magnetostriction is given by

$$\begin{aligned} E = B_1[\varepsilon_{xx}(\alpha_1^2 - \frac{1}{3}) + \varepsilon_{yy}(\alpha_2^2 - \frac{1}{3}) + \varepsilon_{zz}(\alpha_3^2 - \frac{1}{3})] \\ + B_2[\varepsilon_{xy}\alpha_1\alpha_2 + \varepsilon_{yz}\alpha_2\alpha_3 + \varepsilon_{xz}\alpha_1\alpha_3] \end{aligned} \tag{20}$$

where B_1 and B_2 are the magnetoelastic constants, α_n are again the direction cosines of the magnetisation vector and ε_{ij} are the components of the strain tensor. For the works presented in this thesis, a laser induces strain within the sample. It can be shown, via COMSOL simulation, that the shearing forces are confined to the GaAs substrate [45]. This implies the shearing forces can be disregarded, which justifies allowing the off-axis elements of the strain tensor to be 0. Furthermore, thin films of galfenol are used in Chapters 2 and 4, meaning that α_3 can be taken to be 0. This means a reduced

form of equation 20 can be used,

$$E = B_1[\varepsilon_{xx}(\alpha_1^2 - \frac{1}{3}) + \varepsilon_{yy}(\alpha_2^2 - \frac{1}{3})]. \tag{21}$$

The value of B_1 is given by

$$B_1 = \frac{3}{2}\lambda_{100}(c_{12} - c_{11}) \tag{22}$$

here c_{12} and c_{11} are the elastic constants of bulk galfenol; these were found to be $c_{11} = 195$ GPa and $c_{12} = 155$ GPa by Clark [43].
In this thesis, the material of interest is galfenol, an iron-gallium alloy. Galfenol was developed as a cheaper, less brittle alternative to other magnetostrictive materials such as terfenol-D and was first produced by the U.S. Navy in 1998. When increasing the gallium concentration within the alloy, the crystal structure of the material changes from A2, which is the standard structure of iron, to $D0_3$ and finally into the $L1_2$ phase. As gallium content increases, the magnetostriction constant exhibits two peaks: one at 19% and the other at 28%. The first peak is due to nano-inclusions of gallium [46]; however, the effect of these nano-inclusions on the A2 structure of iron is an area of active research [47, 48]. It has been theorised that the inclusions form a $D0_3$ structure within the A2 iron lattice, and under the influence of an external magnetic field, this structure deforms into the $D0_{22}$ structure. More recently, another theory has suggested that fixed Ga-Ga neighbour pairs in the $\langle 100 \rangle$ direction induce a tetragonal transformation of the A2 iron structure [49, 50]. The second peak is caused by a decrease in the material's elastic constants [51]. Following this second peak, the crystal structure changes to the $L1_2$ structure, which is the equilibrium structure when annealing temperatures are below 600°C [52]. The crystal phases mentioned in this work are shown in Figure 3. Since both the elastic constants and the magnetostrictive strain should be maximised to achieve the greatest magnetoelastic energy, the gallium concentration will be 19% for this work. Comparing the magnetostriction variable of galfenol ($Fe_{81}Ga_{19}$) to the magnetic elements shows a greatly increased value; this is shown in table 1

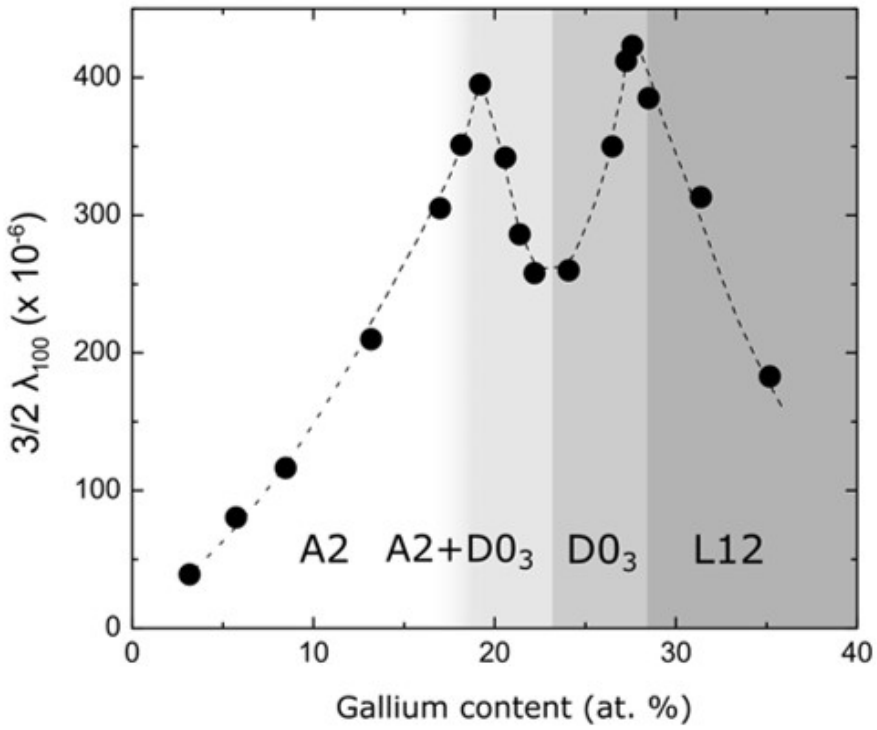


Figure 2: The change in the magnetostriction parameter of Fe-Ga alloys with increasing gallium concentration. There are two peaks in the figure at 19% and 28%, which occur due to the structures the gallium forms within the iron lattice. This figure also shows the different crystal phases the alloy has at the different gallium concentrations. figure taken from [36]

Material	$\frac{3}{2}\lambda_{100}$ (10^{-6})
$Fe_{81}Ga_{19}$	395 [43]
Fe	30 [43]
Ni	-46 [42]
Co	-75 [53]

Table 1: The magnetostriction variables for galfenol compared to the ferromagnetic elements iron, nickel and cobalt

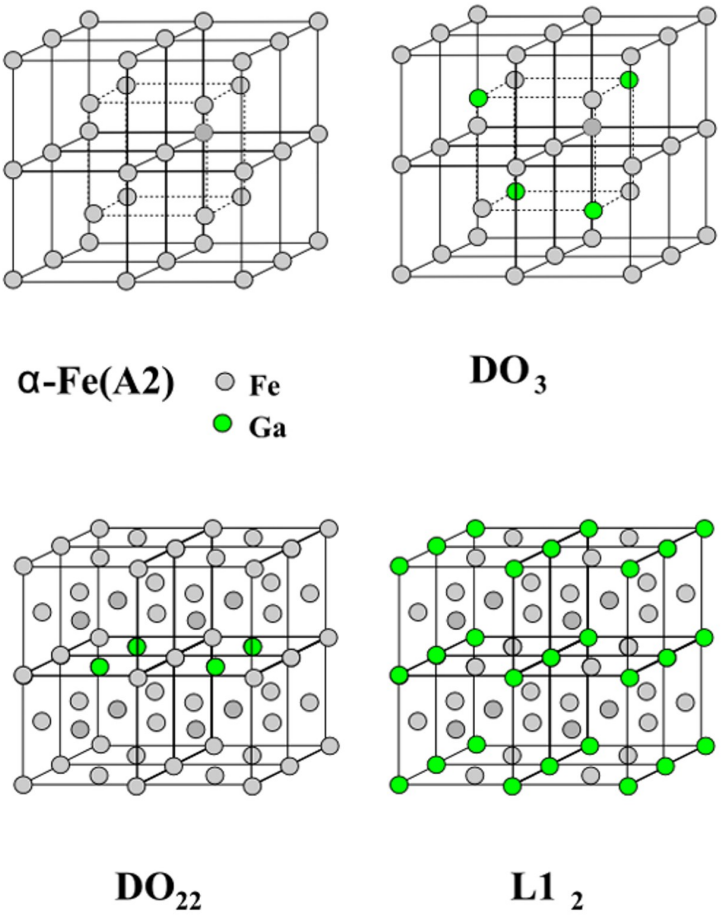


Figure 3: The crystal structures that the galfenol exhibits with different gallium concentrations for the samples used. Iron atoms are illustrated by the grey circles, and gallium atoms are represented by the green circles. A2 is the standard α-Fe BCC structure. DO_3 is still a BCC structure, but some of the centre iron atoms are replaced with gallium. DO_{22} is a FCC structure where some of the face atoms are replaced with gallium. Finally, $L1_2$ is a FCC structure where the corner iron atoms are replaced by gallium; this is the equilibrium crystal structure. Figure adapted from [36]

1.3.7 Spin Current

The net movement of electrons produces charge currents. This occurs in metals under the influence of an electric field. In non-magnetic materials, the average of all the electron spins is zero; however, if the material is ferromagnetic, the spins tend to align due to the exchange interaction, and there is a net spin-polarisation in the conduction band. This means that a charge current in a ferromagnetic material is spin-polarised. The spins, or local moments, can, however, be transferred spatially via the exchange interaction or via spin waves (magnons). This does not require the net movement of any charge carriers; this is a spin current. Spin currents originating from the exchange interaction take the form [54]

$$\boldsymbol{J}_s = 2\frac{Ja^2}{\gamma}\boldsymbol{m}(\boldsymbol{r}) \times \nabla \boldsymbol{m}(\boldsymbol{r}). \tag{23}$$

Here, $\boldsymbol{J}_s$ is the spin current, J is the exchange integral, a is the lattice constant, γ is the gyromagnetic ratio, and $\boldsymbol{m}(\boldsymbol{r})$ is the magnetic moment dependent on the position. This equation for the spin current is derived by solving the undamped Landau-Lifschitz-Gilbert (LLG) (see equation 28 below), where the only term contributing to the effective field is from the exchange interaction. Spin currents, which originate from exchange spin waves, take the form [54]

$$\boldsymbol{J}_s = \hbar \sum_k \boldsymbol{v}_k n_k. \tag{24}$$

where k are the wavevectors, $\boldsymbol{v}_k$ is the group velocity for a particular wavevector, and n_k is the distribution function of the magnons for a particular wavevector. The benefits of spin currents over charge currents include less energy wastage due to heating, as there is reduced resistance from the movement of electrons. However, there are potential problems with spin currents, such as short diffusion lengths.

1.3.8 Inverse Spin Hall Effect

The inverse spin Hall effect (ISHE) and the spin Hall effect (SHE) arise from SOC. Spin Hall materials are a specific class of non-magnetic metals or semiconductors which deflect conduction electrons based on their spin orientation. After injecting a spin current, the spin Hall material produces a charge current longitudinally to the spin current. SHE requires charge currents, which, through the influence of SOC, cause the opposing spins of the electrons to scatter

in different directions transverse to the applied current. This generates a spin current within the spin hall material, which can be used to induce magnetisation precession in a neighbouring ferromagnetic material. ISHE and SHE are characterised by the SHE angle, θ_{SH}, which is defined as

$$\boldsymbol{J}_C = \theta_{SH} \frac{2e}{\hbar} \boldsymbol{J}_s \times \boldsymbol{\sigma}. \tag{25}$$

This defines how effective the conversion is between a spin current, $\boldsymbol{J}_s$, in units of joules per square metre, and a charge current, $\boldsymbol{J}_c$, in units of amps per square metre. σ is the spin polarisation vector. A spin current is generated via magnetisation precession and injected into the spin Hall material. The spin Hall material used within these works is platinum. There are two types of SHE: intrinsic and extrinsic effects. The extrinsic effect is due to the spin-dependent scattering rates caused by SOC [55, 56, 57]. This results in spins being selectively scattered off of material impurities, causing the separation of the two spin directions. The intrinsic effect is due to the Berry curvature derived from the material band structure [58, 59, 60].

1.3.9 Magneto-Optical Kerr effect

Light is known to consist of perpendicularly oscillating electric and magnetic field waves. By convention, the direction of electric field oscillations is used to define the polarisation of the light. The polarisation of light comes in 3 flavours: linear, which occurs when one of the horizontal or vertical components of the electric field has a magnitude of 0, or when the phase and magnitude difference between these components is 0. If the magnitudes of both of these components are non-zero and the phase difference between these fields satisfies $0° < \phi < 90°$, the resultant polarisation is elliptical; finally, when the electric field vectors have a phase difference of $\phi = 90°$ and are equal in magnitude, the polarisation is circular. Mathematically, the polarisation can be modelled by an ellipse circumscribed by a rectangle, with a major axis, a, and a minor axis, b. Figure 4 shows this polarisation ellipse. The tilt angle of the ellipse from the x-axis is θ and defines the magnitude of the electric field components; when $\theta = \pm 45°$, the magnitude of the components is equal. The elliptic angle, $\chi = \arctan(b/a)$, defines how elliptic the ellipse is, with 0 being a line and $\pm 45°$ being a circle; χ is related to the phase difference by $\chi = \phi/2$. The x and y axes represent the

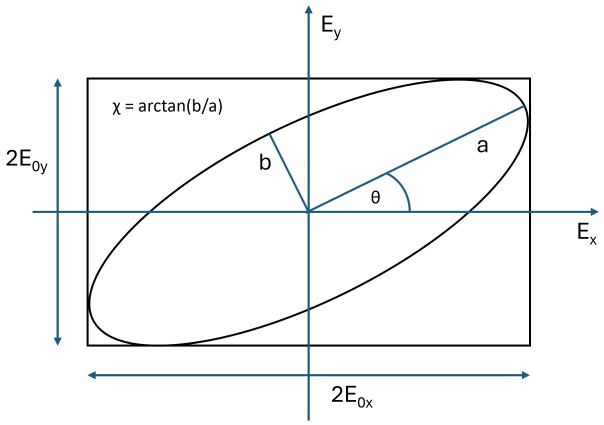


Figure 4: The polarisation ellipse when the x and y components of the electric field are the x and y axes of the figure. The lengths of the electric field components define the length of the sides of the rectangle. The inscribed ellipse has a major and minor axis denoted by a and b, respectively. The tilt angle of the ellipse is denoted by θ, and the elliptic angle, χ, is the arctangent of the ratio of the minor axis to the major axis and defines whether the ellipse is a line, at $\chi = 0°$, an ellipse, $0° < \chi < 45°$, or a circle, $\chi = 45°$.

corresponding components of the electric field vector [61]

$$\begin{aligned} E_x &= E_{0x}\cos(\boldsymbol{k}\cdot\boldsymbol{r} - \omega t) \\ E_y &= E_{0y}\cos(\boldsymbol{k}\cdot\boldsymbol{r} - \omega t - \phi) \end{aligned} \tag{26}$$

where E_x, E_y and E_{0x}, E_{0y} are the x and y components of the electric field and their corresponding magnitudes, k is the wavevector, r is the position vector, ω is the angular frequency and t is time. When the phase difference is set to 0°, the elliptic angle is also 0°, and therefore the minor axis is zero; therefore, this is the case for linearly polarised light. When the phase difference is set to 90°, the elliptic angle is 45°. When the tilt angle is also 45°, the resultant polarisation is circular. A figure illustrating these different polarisations of light is given by Figure 5.

The polarisation of the incident light relative to the sample surface is also important; this is referred to as s or p polarisation. P polarisation occurs when the incident light is polarised parallel to the sample surface, whereas s polarisation occurs when the incident light is polarised perpendicular to the sample surface.

The magneto-optical Kerr effect (MOKE) arises from the interaction between the polarisation of light and the magnetisation of a material. This interaction was first observed in 1877 by John Kerr [63]. There are three distinct types of MOKE, which depend on the

Phase shift ϕ [deg]	0	11.2	22.6	33.8	45	56.2	67.6	78.8	90	78.8	67.6	56.2	45	33.8	22.6	11.2	0
Ellipse																	
Orientation θ [deg]	45	45	45	45	45	45	45	45	45	-45	-45	-45	-45	-45	-45	-45	-45
Ellipticity χ [deg]	0	5.6	11.3	16.9	22.5	28.1	33.8	39.4	45	39.4	33.8	28.1	22.5	16.9	11.3	5.6	0

Figure 5: An illustration of the different polarisations of light based on the phase shift of the components of the electric field vector. From left to right, there is linearly polarised light where the electric field vector oscillates in one direction. Elliptically polarised light occurs when the difference in magnitude of the electric field components is non-zero, and the phase difference between the components is given by $0° < \phi < 90°$. Next, Circularly polarised light occurs when the components of the electric field are of equal amplitude and have a phase difference of 90°. θ is the orientation of the ellipse shown in Figure 4 and varies between $\pm 45°$, and χ is the elliptic angle, which defines how circular the ellipse is and varies from 0 to 45°. Figure adapted from [62]

magnetisation direction within the material. A diagram illustrating each type is shown in Figure 6, where the incident electric field has a polarisation given by $E^i_{s/p}$ and a wavevector, k, and the reflected electric field is similarly given by $E^r_{s/p}$ where the angle of incidence is θ and finally the magnetisation is M.

Polar MOKE occurs when the magnetisation is out of the plane of the material and is characterised by a change in the polarisation of the reflected light. This type of MOKE is maximised when the angle of the incident light is perpendicular to the surface.

Longitudinal MOKE occurs when the magnetisation is longitudinal to the sample and is also characterised by a change in the polarisation of the reflected light. This type of MOKE is minimised when the angle of incidence is 0° and increases with angle.

Transverse MOKE occurs when the magnetisation is transverse to the sample and is characterised by a change in the intensity. This type of MOKE is also minimised when the angle of incidence is 0°, with increasing magnitude when the angle of incidence increases. For polar and longitudinal MOKE, the polarisation can be either s or p. By having the incident light linearly polarised, the change in polarisation is easier to quantify. For transverse MOKE, the polarisation of the incident light must be parallel to the sample surface; therefore, p-polarised light must be used [61]. The change in polarisation (known as the Kerr angle Φ_K) and the change in intensity (δ_p)

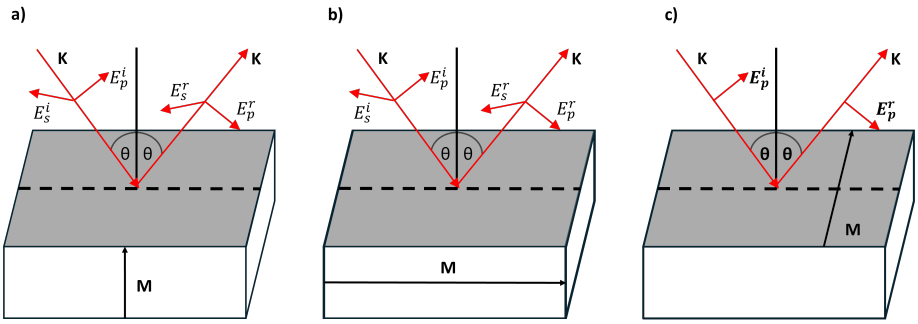


Figure 6: Illustration showing the different geometries of MOKE with the surface of the material shaded. a) Polar MOKE, where either incident light that is s or p polarised with respect to the sample surface can be used, and the reflected light has a Kerr rotation imparted such that the polarisation is elliptical. The magnetisation of the sample is out of the plane of the sample. Polar MOKE is optimised when θ is 0°. b) Longitudinal MOKE, either incident light that is s or p polarised with respect to the sample surface can be used, and the reflected light has a Kerr rotation imparted such that the polarisation is elliptical. The magnetisation of the sample is parallel to both the reflection surface and the plane of incidence. c) Transverse MOKE, where the incident light must be p-polarised with respect to the sample surface, and the reflected light has a change in intensity, but the polarisation remains unchanged. The magnetisation of the sample is parallel to the reflection surface and perpendicular to the plane of incidence.

after the reflection can be rigorously derived by considering the incident electric field vector and multiplying this by the Jones matrix for the material to get the reflected electric field vector, where Jones matrices are matrices that act on the electric field vectors and its polarisation and transforms the polarisation depending on the matrix parameters, which are determined via the material, namely the refractive index. However, the calculation of the Jones matrix is not important for the final result.

The general equations for the Kerr angle in the polar and longitudinal regimes and the change of intensity in the transverse regime are given by [61]

$$\begin{aligned}
\Phi_K^{polar} &= \Im\frac{(n_2/n_1)^2(((n_2/n_1)^2-\sin^2(\theta))^{1/2}\mp\sin(\theta)\tan(\theta))}{((n_2/n_1)^2-1)((n_2/n_1)^2-\tan^2(\theta))}Q \\
\Phi_K^{long} &= \Im\frac{\sin(\theta(n_2/n_1)^2)(\sin(\theta)\tan(\theta)\pm\sqrt{(n_2/n_1)^2-\sin^2(\theta)})}{((n_2/n_1)^2-1)((n_2/n_1)^2-\tan^2(\theta)\sqrt{(n_2/n_1)^2-\sin^2(\theta)}}Q \\
\delta_p^{trans} &= -\Im\frac{4\tan(\theta(n_2/n_1)^2)}{((n_2/n_1)^2-1)((n_2/n_1)^2-\tan^2(\theta))}Q
\end{aligned} \tag{27}$$

$\Im$ denotes that the imaginary part of this equation is taken. n_i is the complex refractive index of the incident medium (n_1) or the medium reflected off of (n_2), θ is the angle of incidence, and Q is the Voigt parameter, which is dependent on the magnetisation of the medium reflected off and is a measure of how strongly the polarisation is rotated [61]. The upper and lower branches (+ or -) produce the Kerr angles for electric field components perpendicular and parallel to the plane of the material, respectively.

This thesis utilises polar MOKE. Typically, MOKE is used to either spatially resolve domain structures within a magnetic material or to temporally observe the precession of the magnetisation vector. The temporal approach is of interest in this thesis because, by measuring the oscillating polarisation, the lifetime, frequency, and amplitude of the generated magnons can be determined.

1.4 Micromagnetism

Micromagnetism explains macroscale magnetic phenomena by exploring the micro- and submicroscale dynamics of the magnetisation within a material, treating the quantum magnetic moments as part of a vector field and taking the continuum limit (where the cell size is larger than the discrete unit, which in this case is the atomic magnetic moment). This technique is usually used to simulate a magnetic system based on the magnetic free energy of the

system and the equation of motion of the magnetisation, $\boldsymbol{M}$. This requires that the different energy density terms be defined, along with a region (the sample dimensions) and a mesh (the size of each magnetisation cell). The equation of motion, in this case, is the Landau-Lifshitz-Gilbert (LLG) equation [64].

1.4.1 Landau-Lifshitz-Gilbert Equation

The LLG equation is

$$\frac{\partial \boldsymbol{M}}{\partial t} = -\gamma \boldsymbol{M} \times \boldsymbol{H}_{\text{eff}} - \alpha \frac{\gamma}{M_s} \boldsymbol{M} \times (\boldsymbol{M} \times \boldsymbol{H}_{\text{eff}}) \tag{28}$$

where γ is the gyromagnetic ratio, α is the damping parameter, M_s is the saturation magnetisation, $\boldsymbol{H}_{eff}$ is the effective magnetic field and $\boldsymbol{M}$ is the magnetisation. The first term of the LLG equation describes precessional motion. This can be derived by first considering a classical torque caused by a magnetic field,

$$\boldsymbol{\tau} = \frac{\partial \boldsymbol{L}}{\partial t} = \mu_0 (\boldsymbol{m} \times \boldsymbol{H}) \tag{29}$$

$\boldsymbol{\tau}$ is a torque, $\boldsymbol{L}$ is the angular momentum, m is the magnetic moment, and μ_0 is the permeability of free space. This, along with the knowledge that the magnetic moment is intrinsic angular momentum, can take the form.

$$\boldsymbol{m} = \gamma_0 \boldsymbol{L} \tag{30}$$

Where γ_0 is a scaled gyromagnetic ratio. Equating these two relations and taking the combined magnetic moment of the system (the magnetisation) produces the first term of the LLG equation, which results in a rotational motion. The second term introduced by Gilbert is a damping term. This term has phenomenological origins and allows the precession of the magnetisation to diminish over time. The effective magnetic field parameter is defined by

$$\boldsymbol{H}_{eff} = -\frac{1}{\mu_0} \frac{\partial E}{\partial \boldsymbol{M}} \tag{31}$$

where $\boldsymbol{E}$ is the total magnetic free energy density of the system.

1.4.2 Magnetic Free Energy Density

The total magnetic free energy density is formed from the sum of the magnetic free energy density terms. The terms of relevance are

$$E = E_{uniaxial} + E_{cubic} + E_{exchange} + E_{magnetoelastic} + E_{Zeeman} + E_{demag} \tag{32}$$

The new terms here are the Zeeman energy and the demagnetising energy. The Zeeman energy used in the simulation has the form

$$E_{Zeeman} = -\mu_0 \boldsymbol{M} \cdot \boldsymbol{H}_{ext} \tag{33}$$

This energy term describes the effect of an external magnetic field on the magnetisation. The magnetisation aligns with the field, where the strength of the interaction depends on the magnitude of the magnetic field.

The demagnetising energy is more complicated. The basic form used in the simulation is similar to the Zeeman energy, being

$$E_{demag} = -\frac{1}{2}\mu_0 \boldsymbol{M} \cdot \boldsymbol{H}_{int} \tag{34}$$

where $\boldsymbol{H}_{int}$ is the internal magnetic field, which arises from the magnetisation itself [38].

A final key parameter to consider is the exchange length, which defines the length over which the exchange interaction acts. When defining a micromagnetic simulation, the mesh size must be less than or equal to the exchange length for the effects of the exchange interaction to be observed. The exchange length is given by

$$l_{ex} = \sqrt{\frac{A}{K}} \tag{35}$$

where l_{ex} is the exchange length, A is the exchange stiffness, and K is the anisotropy coefficient.

1.4.3 Simulation

In micromagnetic simulations, a continuous approach to modelling the LLG equation is not feasible; therefore, a discretised method is used, known as the finite-difference method. This method works by taking an initial known magnetisation at a point ($\boldsymbol{r}$), $\boldsymbol{M}_i(\boldsymbol{r})$, and having the new magnetisation at the next time step but at the same point, Δt, be $\boldsymbol{M}_{i+1}(\boldsymbol{r})$. This allows the time derivative in the LLG equation to be written as:

$$\frac{\partial \boldsymbol{M}(\boldsymbol{r})}{\partial t} = \frac{\boldsymbol{M}_{i+1}(\boldsymbol{r}) - \boldsymbol{M}_i(\boldsymbol{r})}{\Delta t}. \tag{36}$$

This allows the LLG equation to be written as a finite-difference equation, which is sufficiently discretised to be solved by a computer. To achieve an appropriate level of detail, the time step should be sufficiently small, depending on the timescale of the expected effect.

The LLG is first solved for one position on the mesh; following this, the neighbouring points are solved. This continues until all the elements of the mesh have been solved for. The process is repeated until the change in magnetisation at each point of the mesh falls below a preset threshold. After this process, the solution for the magnetisation is used as the new initial magnetisation in the next iteration of the simulation. This process is repeated until the total time is run.

This demonstrates the simplest case; within this thesis, Ubermag [65] is used for simulations, and the equation used for each time step is RK4; this is chosen as it is more accurate and, more importantly, avoids instabilities. The RK4 equations are:

$$\begin{aligned} \boldsymbol{M}_{i+1}(\boldsymbol{r}) &= \boldsymbol{M}_i(\boldsymbol{r}) + \frac{\Delta t}{6}(k_1 + 2k_2 + 2k_3 + k_4) \\ k_1 &= \boldsymbol{H}_{eff}(\boldsymbol{M}_i(\boldsymbol{r}), t_i) \\ k_2 &= \boldsymbol{H}_{eff}(\boldsymbol{M}_i(\boldsymbol{r}) + k_1\frac{\Delta t}{2}, t_i + \frac{\Delta t}{2}) \\ k_3 &= \boldsymbol{H}_{eff}(\boldsymbol{M}_i(\boldsymbol{r}) + k_2\frac{\Delta t}{2}, t_i + \frac{\Delta t}{2}) \\ k_4 &= \boldsymbol{H}_{eff}(\boldsymbol{M}_i(\boldsymbol{r}) + k_3\Delta t, t_i + \Delta t) \end{aligned} \tag{37}$$

where the k-parameters are used to determine the gradient at various points within the time step, thereby increasing accuracy and removing divergences.

1.5 Quasiparticles

Quasiparticles are the result of a technique that is used to simplify many-body interactions, allowing them to be treated as a single particle. This includes the vibrations of coupled atoms in a lattice (phonons), the oscillations of coupled magnetic moments (magnons) and bound electron-hole pairs (excitons).

1.5.1 Magnons

Magnons are the quasiparticles that result from the quantisation of spin waves, which are the coherent oscillations in the magnetic moments of electrons within the lattice of a material. To derive the dispersion relation, consider a ferromagnet in the ground state (all the spins are aligned). If a 1D line of this ferromagnet is taken and we assume all the spins interact only through the exchange interaction, we can use a sum of the exchange energy given by equation 1 over each neighbouring spin. This type of spin wave is illustrated

in Figure 7. By examining a single spin with coordinates p and its two nearest neighbours, the energy can be written as.

$$E = -2J\boldsymbol{s}_p \cdot (\boldsymbol{s}_{p-1} + \boldsymbol{s}_{p+1}) \tag{38}$$

The magnetic moment of $\boldsymbol{s}_p$ is given by $\boldsymbol{m}_p = -g\mu_B \boldsymbol{s}_p$. The following equation is obtained by substituting this in for $\boldsymbol{s}_p$.

$$E = -\boldsymbol{m}_p \cdot [(-2\frac{J}{g\mu_B})(\boldsymbol{s}_{p-1} + \boldsymbol{s}_{p+1})] \tag{39}$$

The second term acts like a magnetic field due to the exchange interaction and can be defined as $\boldsymbol{B}_p$. The torque on $\boldsymbol{s}_p$ can now be defined as:

$$\hbar\frac{d\boldsymbol{s}_p}{dt} = \boldsymbol{m}_p \times \boldsymbol{B}_p. \tag{40}$$

This can be rewritten as

$$\hbar\frac{d\boldsymbol{s}_p}{dt} = 2J(\boldsymbol{s}_p \times \boldsymbol{s}_{p-1} + \boldsymbol{s}_p \times \boldsymbol{s}_{p+1}). \tag{41}$$

By splitting this vector equation into its Cartesian components, taking the initial magnetised state to be aligned in the z direction and by making the assumption that the x and y components are small due to a low-amplitude excitation, the z component can be taken to be equal to the total magnitude of the spin, S, and a set of linear equations can be acquired.

$$\begin{aligned} \frac{ds_p^x}{dt} &= (\frac{2JS}{\hbar})(2s_p^y - s_{p-1}^y - s_{p+1}^y) \\ \frac{ds_p^y}{dt} &= (-\frac{2JS}{\hbar})(2s_p^x - s_{p-1}^x - s_{p+1}^x) \\ \frac{ds_p^z}{dt} &= 0 \end{aligned} \tag{42}$$

We make the ansatz that the solutions to the equations take the form of a travelling wave given by:

$$\begin{aligned} s_p^x &= ue^{i(pka-\omega t)} \\ s_p^y &= ve^{i(pka-\omega t)} \end{aligned} \tag{43}$$

where u and v are constants, $\boldsymbol{k}$ is the wavevector, a is the lattice constant and ω is the angular frequency. By substituting these travelling wave solutions into the differential equations, it can be shown that

$$\hbar\omega = 4JS(1 - \cos(\boldsymbol{k}a)). \tag{44}$$

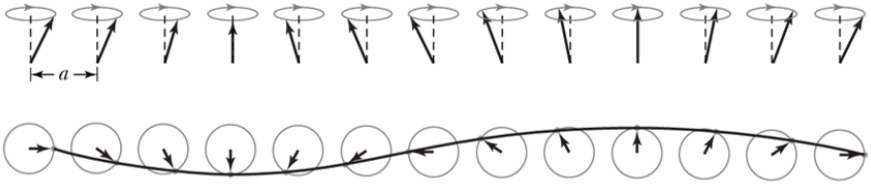


Figure 7: An illustration of a one-dimensional spin wave from two viewpoints. The distance between the neighbouring spins is a, which is determined by the crystal structure. Figure adapted from [34]

Assuming that the wavelengths are larger than the spin spacing, a, the small-angle approximation can be used, yielding the final form of the 1D magnon dispersion relation [34]. This can be used to produce Figure 8.

$$\hbar\omega = 2JSa^2k^2. \tag{45}$$

This form of the dispersion relation does not account for dipolar interactions or the sample's shape.

Within the works presented in Chapter 4, the sample is a thin rectangular film, implying that it can be magnetised in either the longitudinal or transverse direction. It is assumed that the sample magnetisation is saturated by an external field applied in either direction and that the sample is thin enough that the change in the z-component of the magnetic moment is approximately zero. This allows the reduced magnetisation ($\boldsymbol{m} = \boldsymbol{M}/M_s$) to be written as [66]

$$\boldsymbol{m}(x,y,t) = M_s\hat{\boldsymbol{x}} + m_y(x,y,t)\hat{\boldsymbol{y}} + m_z(x,y,t)\hat{\boldsymbol{z}}. \tag{46}$$

In this case, the external field direction is the x direction. By including the Zeeman term, the exchange term, and the demagnetising term, the effective field can now be defined as

$$\begin{aligned}\boldsymbol{H}_{eff}(x,y,t) =& \boldsymbol{H}_{ex} + \frac{2A}{M_s^2}\nabla^2_{x,y}\boldsymbol{M}(x,y,t) + \\ & 4\pi\int \hat{\boldsymbol{G}}(x,y,x',y')\cdot M(x',y',t)dx'dy'\end{aligned} \tag{47}$$

where the first term is the Zeeman field, the second term is the exchange field with $A = J(Sa)^2/2$ and the 2D laplacian being derived by taking the continuum limit of the exchange energy and the above assumption that the sample is a thin film, and the final term is the demagnetising field with $\hat{\boldsymbol{G}}$ being the Green's function that

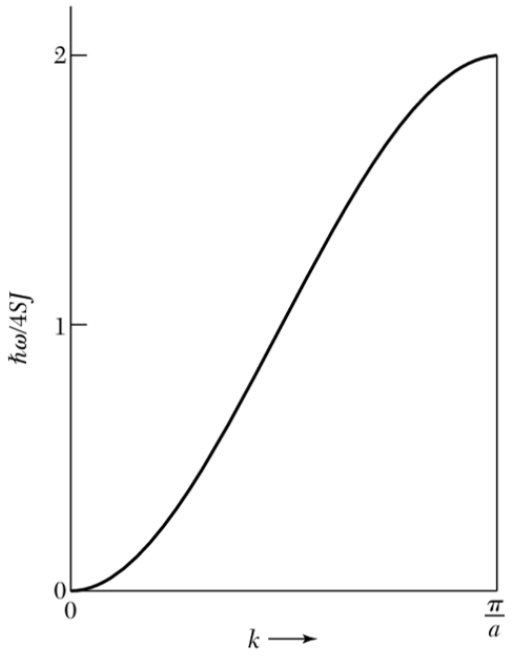


Figure 8: The dispersion relation of a magnon from a 1D ferromagnet with nearest-neighbour interactions considered. This applies to positive wavevectors within the first Brillouin zone. Figure taken from [34]

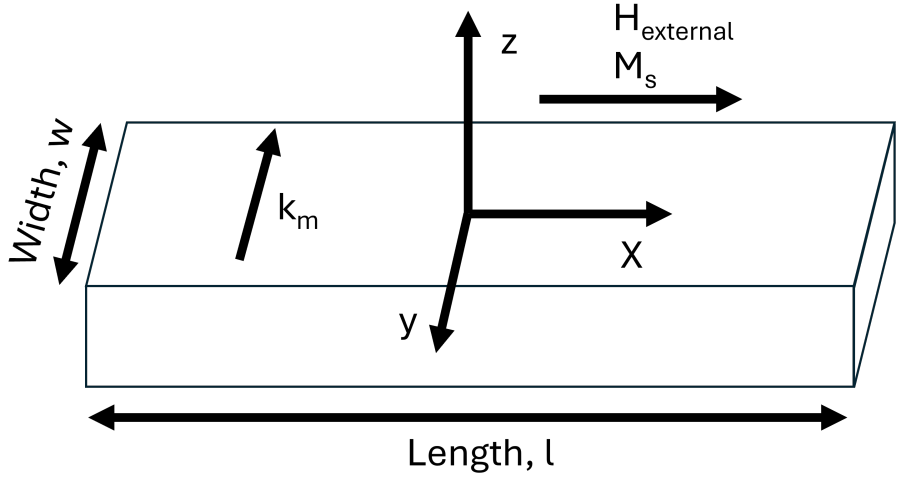


Figure 9: An illustration of the geometry for DE mode magnons. Here, the length is much greater than the width. The external field and the magnetisation are parallel to each other, and the wavevectors are perpendicular to them.

describes the dipolar interactions between spins. These terms can then be used to solve the LLG equation; the full derivation of each of these solutions is beyond the scope of this thesis, so only the relevant results are presented here. First, consider a stripe where the length of the stripe is much greater than its width, such that the length can be approximated as infinite and the magnetisation is longitudinal. This is illustrated in Figure 9. For wavevectors in the transverse direction, the resultant dispersion relation for this geometry is

$$(\frac{\omega_m}{\omega_M})^2 = (\frac{\omega_H}{\omega_M} + \alpha k_m^2 + 1 + \frac{\lambda_m}{4\pi})(\frac{\omega_H}{\omega_M} + \alpha k_m^2 - \frac{\lambda_m}{4\pi}). \quad m = 1, 2, 3, ... \tag{48}$$

Here $\omega_M = \gamma 4\pi M_s$, $\alpha = A/2\pi M_s$, $\omega_H = \gamma H_{in}(x, y)$ is a demagnetising field variable dependent on the internal fields, λ_m are the eigenvalues found from the dipolar interaction integral. k_m are the wavevectors, which are scaled by the effective pinning parameter, $d(p)$, which is a function dependent on p, where p is the thickness, t, divided by the width, w, of the sample stripe.

$$k_m = \frac{m\pi}{\omega} \frac{d(p) - 2}{d(p)} \tag{49}$$

$d(p)$ is given by:

$$d(p) = \frac{2\pi}{p(1 + 2ln(1/p))}. \tag{50}$$

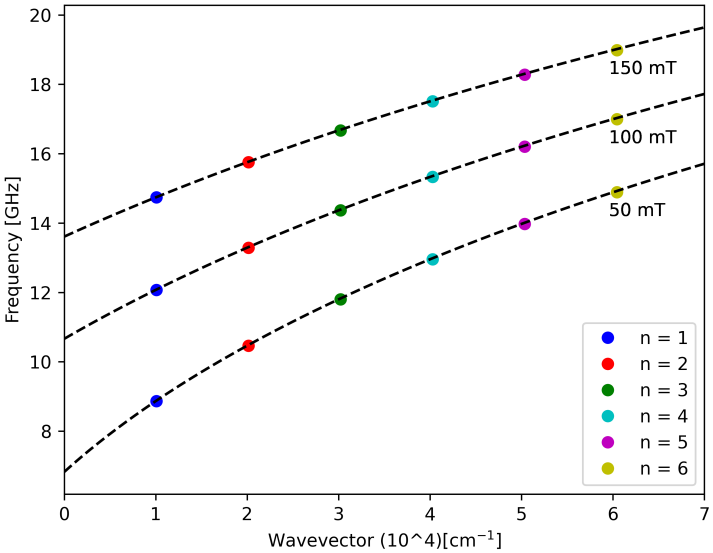


Figure 10: The dispersion curve for the DE modes in a galfenol bar of width 3 μm, length 20 μm and thickness 36 nm. In this figure, the dashed lines represent the dispersion if the wavevector were continuous. The dots are the discrete values of the wavevector, which are discretised due to the confinement from the width of the bar. Equation 48 is implemented in Python to compute the first 6 DE modes; only discrete wavevectors are used. To produce the continuous curve, wavevectors varying from 0 to 7×10^4 cm^2 with 1000 steps in between were used. The dispersion relation is shown for three different magnetic fields of 50, 100 and 150 mT

Spin waves in this geometry are known as Damon-Eshbach (DE) modes [67]. The calculated dispersion relation for the samples described in Chapter 4 is shown in Figure 10.

In the transverse case, take the width to be much greater than the length, again such that the width can be considered infinite, illustrated in Figure 11. In this geometry, there are modes localised in two regions of the sample: the edges and the centre. The edge modes are exchange-dominated [68], with the region separating the edges and the centre determined by the inhomogeneous internal field. This results in an area where spin waves cannot be excited due to there being no wavevectors that satisfy the phase relation [69].

$$\phi = \int k[H_{int}(x), \omega]dx = m\pi \quad m = 1, 2, 3... \tag{51}$$

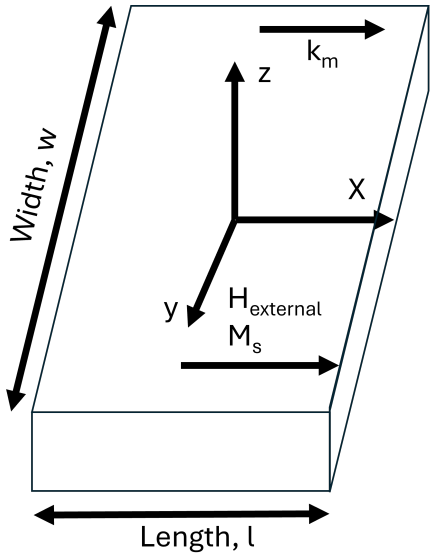


Figure 11: An illustration of the geometry for BV mode magnons. Here, the width is much greater than the length. The external field, magnetisation, and wavevectors are all parallel.

Here, ϕ is the phase of the magnons and k is the wavevector that depends on the internal field H_{int} and the frequency. The centre modes are dipolar-dominated [68]. Due to the pinning at the edges of the sample, the magnetisation is pinned parallel to the edges and therefore perpendicular to the applied field and the wavevectors, suggesting that the modes localised at the edges are DE modes. The modes localised in the centre of the stripe are backward volume (BV) modes [68]. The dispersion relation for BV spin wave modes is given by [66]

$$(\frac{\omega}{\omega_M})^2 = (\frac{\omega_H}{\omega_M} + \alpha k^2)(\frac{\omega_H}{\omega_M} + \alpha k^2 + 1 - P(kL)). \tag{52}$$

Where $P(kL)$ is given by $P(kL) = 1 - \frac{1-\exp(-kL)}{kL}$, and L is the thickness of the sample. The dispersion relation for these modes for the galfenol samples is shown in Figure 12. Magnons exist in ferromagnets and antiferromagnets. Ferromagnetic magnons are typically of the order GHz, and antiferromagnetic magnons are of the order THz.

Current research focuses on manipulating these quasiparticles and on producing on-chip devices that utilise magnon properties [70]. The work in this area has led to the development of magnonic crystals [71, 72, 73], where periodic variations in the spatial structure of a material manipulates the band structure of the excited

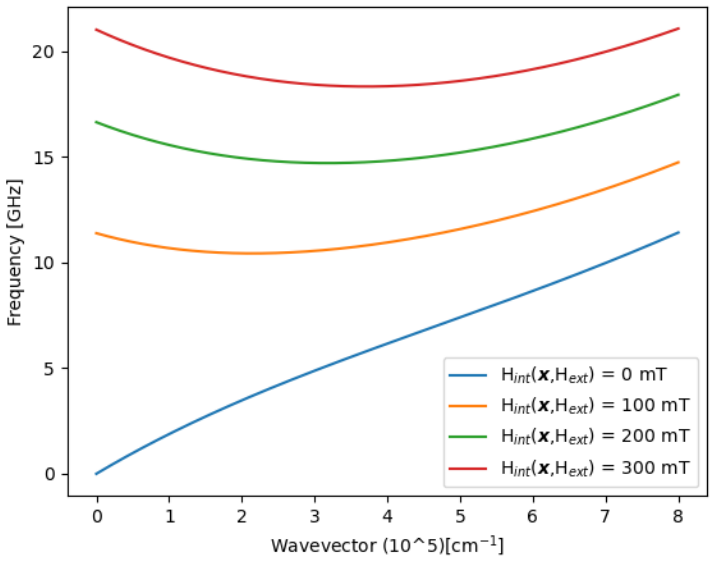


Figure 12: The dispersion curve for the BV modes in a galfenol bar with width 20 μm, length 3 μm, and thickness 36 nm. This figure is produced in Python by modelling equation 52. In this figure, each line represents a different internal field. The internal field depends on the position in the bar and the external field. To simplify the equation, the explicit position dependence and the external field are neglected, and the internal field is set directly with the values taken being 0, 100, 200 and 300 mT. The wavevectors varied from 0 to 8×10^5 cm^2.

magnons. This allows for confinement of specific modes and desired frequencies. By tuning the band structure through the fabrication of on-chip devices, logic gates can be developed, with XNOR and NAND gates being first realised [74], followed by NOT [75], AND [76], and OR [77] gates. Magnon transistors have also been demonstrated, enabling the realisation of an XOR gate [78]. With these developments, the transfer and manipulation of binary information via magnons is now realisable. There has also been progress in making read heads which utilise spin waves [79], where the amplitude and the phase information of the wave can be used to interpret the magnetic state of the magnetic storage device.

1.5.2 Phonons

Phonons are quasiparticles that arise from the quantisation of vibrations within the lattice of any crystalline material. The dispersion relation for this quasiparticle can be derived from a similar model to that of magnons. Consider a 1D chain of particles with mass, m, connected via spring-like bonds with spring constant, C. Taking a similar approach to the magnons and defining a particle, p, at the position, x_p, and only considering the interactions with its two nearest neighbours, it can be shown that the equation of motion for this system is

$$m\frac{d^2x_p}{dt^2} = C(x_{p+1} + x_{p-1} - 2x_p). \tag{53}$$

By taking an ansatz that the time dependence of the position takes the form $e^{-i\omega t}$, substituting this into the left side of the equation results in

$$-m\omega^2 x_p = C(x_{p+1} + x_{p-1} - 2x_p). \tag{54}$$

Letting $x_{p\pm1} = xe^{ika(p\pm1)}$ allows the above equation to take the form

$$m\omega^2 = -C(e^{ika} + e^{-ika} - 2). \tag{55}$$

Which can be simplified to be

$$\omega^2 = \frac{4C}{m}sin^2(\frac{ka}{2}). \tag{56}$$

This form of the dispersion relation describes the simplest case in which the lattice comprises identical atoms with identical interactions. To model the more complex problem of two different atoms in the basis, multiple masses can be used by modelling a pair of coupled equations, both of the form of equation 53 but with different masses m_1 and m_2. An illustration of this situation is shown in

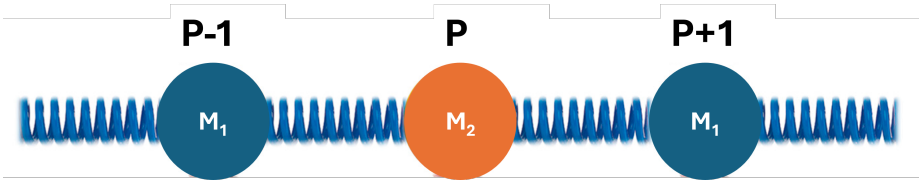


Figure 13: An illustration of a one-dimensional chain of atoms connected via springs, where the central atom is at position p and the neighbours are at p-1 and p+1. The central atom has mass M_2 and the neighbours have mass M_1. This figure is adapted from [80].

Figure 13. The dispersion relation of the model with two different masses allows for the observation of two distinct phonon modes: the optical and the acoustic modes where the dispersion relation is given by:

$$\begin{aligned} \omega^2 =& 2C\left(\frac{1}{m_1}+\frac{1}{m_2}\right) \text{ (optical branch)} \\ \omega^2 =& \frac{C}{2(m_1+m_2)}k^2a^2 \text{ (acoustic branch)} \end{aligned} \tag{57}$$

This dispersion relation is shown in Figure 14.

The phonon modes previously discussed are bulk crystal modes; however, phonon modes can also be localised only on the surface of a material or in thin films. These are surface acoustic waves (SAWs). Starting with Newton's second law and Hooke's law, the equation of motion can be written as:

$$\rho\frac{\partial^2 u_i}{\partial t^2} = \frac{\partial T_{ij}}{\partial x_j}. \tag{58}$$

Here, ρ is the mass density, u_i are the displacement components along each of the Cartesian axes x_i, and T_{ij} are components of the stress tensor. By taking equation 58 and imposing the conditions that the wave propagates in the plane of the sample along only the axis x_1 and the boundary condition, the amplitude and displacement decay rapidly in the x_2 direction such that $u_2 = 0$. It can be shown that the resultant displacement vectors for this wave are:

$$\begin{aligned} u_1 &= A_1 cos(k(x_1 - vt)) \\ u_3 &= A_3 sin(k(x_3 - vt)). \end{aligned} \tag{59}$$

Where A_i is the amplitude of the displacement component, and v is the phase velocity. These equations indicate that in these waves, the particles exhibit elliptical motion out of the sample plane; this type of SAW is known as a Rayleigh wave [81]. The second-order

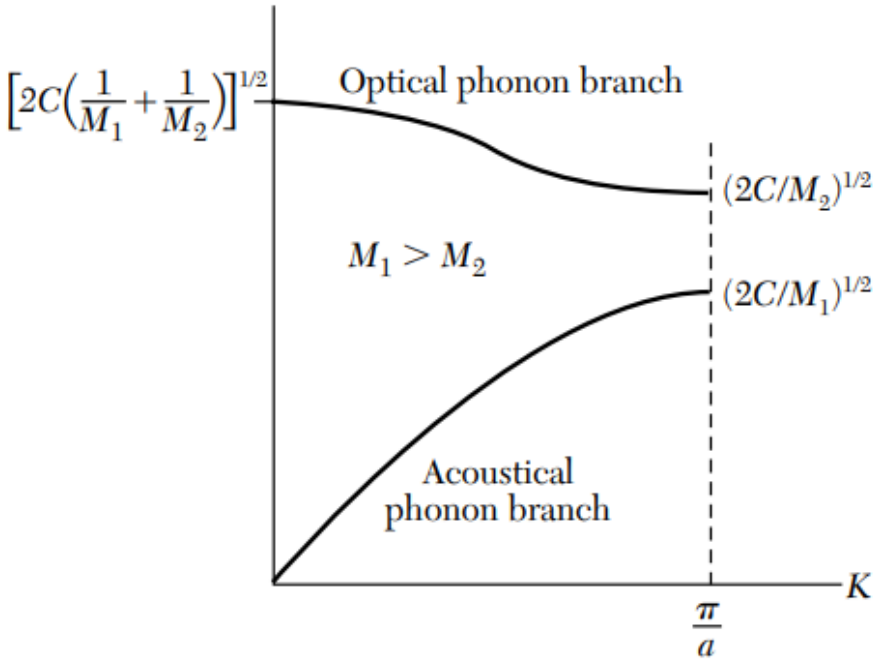


Figure 14: The first Brillouin zone of the dispersion relation for phonons in a crystal where there are two different atoms of different masses comprising the crystal. The resulting dispersion produces two branches: the upper branch is the optical branch, and the lower branch is the acoustic branch. This figure is taken from [34].

mode of this type is called a Sezawa wave. There are other SAWs. These include: p-waves, where the particle motion is longitudinal; S-waves, where the particle motion is transverse but purely out of the plane; and Love waves, where the particle motion is transverse and in the plane. The only modes of interest in these experiments are the Rayleigh waves.

1.5.3 Excitons

The exciton is a quasiparticle that differs from the previously explored particles. This particle is found in semiconductor materials and is a bound electron-hole pair. This particle is derived from the Schroedinger equation, where the Hamiltonian term contains kinetic energy, potential energy and Coulomb interaction terms for both the hole and the electron [82]. The resulting time-independent Schroedinger equation takes the form:

$$[(E_c - \frac{\hbar^2}{2m_0 m_e}\nabla_e^2) - (E_v - \frac{\hbar^2}{2m_0 m_h}\nabla_h^2) - \frac{e^2}{4\pi\varepsilon_0\varepsilon_h|\boldsymbol{R}_e - \boldsymbol{R}_h|} + V_e(\boldsymbol{R}_e) + V_h(\boldsymbol{R}_h)]\psi(\boldsymbol{R}_e, \boldsymbol{R}_h) = E\psi(\boldsymbol{R}_e, \boldsymbol{R}_h). \quad (60)$$

E_c and E_v are the energies of the conduction band and the valence band, $m_0 m_e$ and $m_0 m_h$ are the effective masses of the electrons and the holes and ε_h is the relative permittivity of the holes. To solve a simplified version of the equation, the free-space solutions are explored (the potential energy terms are set to 0). With some substitutions, the equation can be rewritten as [83]:

$$[(-\frac{\hbar^2}{2m_0 M}\nabla_{cm}^2) + (E_g - \frac{\hbar^2}{2m_0 m_{eh}}\nabla^2 - \frac{e^2}{4\pi\varepsilon_0\varepsilon_b\boldsymbol{R}}]\psi = E\psi \quad (61)$$

M is the combined hole and electron mass, m_{eh} is the sum of the reciprocals of the masses, R is the difference between the electron and hole position vectors, and ∇_{cm}^2 is the Laplacian using the centre of mass coordinates. The terms in brackets can yield different solutions, with the first term providing a plane wave solution, whereas the other term describes a particle with hydrogen-like energy and exists within the band gap, just below the conduction band [84]. These excitons are known as Wannier-Mott excitons [83, 85]. The energy of these excitons is given by

$$E_n = E_g - \frac{r}{n^2} \quad (62)$$

where E_g is the band gap energy, n is an integer, and r is the scaled Rhyberg energy given by $r = (m_0 m_{eh}/2)(e^2/4\pi\varepsilon_0\varepsilon_b\hbar)^2$. There are

other types of excitons that are localised to singular atoms, known as Frenkel excitons [83]. Frenkel excitons are not explored within these works.

1.5.4 Coupling

Coupling is the interaction between particles or quasiparticles. There are two coupling regimes: weak and strong. Weak coupling occurs when the decay rate of the particles is lower than the energy exchange rate, resulting in no lasting interaction between the particles. Strong coupling enables coherent energy transfer between particles, allowing them to be treated as a single entity. This is beneficial since the positive attributes of both individual particles are now properties of the composite particle. Some attributes, such as particle lifetimes and controllability, are desirable for implementing particles in technologies. For example, phonons have lifetimes on the order of 10s of ns [1], whereas magnon lifetimes are on the order of 1 ns, so their composite particle would have a longer lifetime than magnons alone, and magnons are easily tuneable via an external field. To achieve strong coupling between magnons and phonons, the spatial overlap of the modes and their respective lifetimes should be optimised. This was accomplished by surface patterning a ferromagnetic film [1], which spatially confines the modes and allows for the frequency of the allowed phonons to be selected. To separate these two coupling regimes, cooperativity is defined as

$$C = \frac{\kappa^2}{\lambda_1 \lambda_2} \tag{63}$$

where κ is the coupling strength that is characterised by $\Delta/2$, which is half the frequency splitting between the systems when they are in resonance, and the λs are the decay rates of the individual particles, which are equivalent to the full width half maximum (FWHM) of the resonant peak in the power spectrum for each excitation. If the cooperativity is less than one, the weak-coupling regime applies; if the cooperativity is greater than or equal to one, the strong-coupling regime applies. There is also an ultra-strong coupling regime where C is orders of magnitude greater than one; this regime is, however, not reasonable to consider, as the particles used in these experiments have only recently been strongly coupled for the first time.

1.6 Fano Resonance

A Fano resonance is a resonant interaction between two weakly coupled systems whereby the lineshape of the produced resonance is asymmetric [86] as shown in Figure 15. Fano first described this type of resonance while exploring autoionisation in helium atoms, in which an electron-electron collision can excite an electron to an ionisation state [87]. Fano resonances are, however, a general effect.

The equation that Fano derived to describe the resonance is given by:

$$A = \frac{(q\Gamma/2 + \omega - \omega_0)^2}{(\Gamma/2)^2 + (\omega - \omega_0)^2} \tag{64}$$

where A is the amplitude of the resonance, q is a dimensionless quantity that determines how asymmetric the resonance is (if q is 0, the resonance is symmetric), Γ is the linewidth of the resonance, and ω_0 is the resonance frequency.

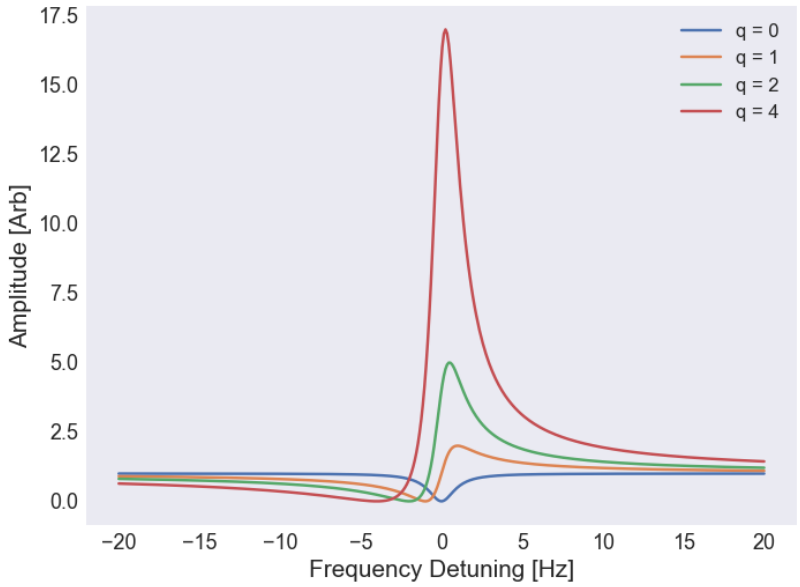


Figure 15: The shape of a general Fano excitation. There is a drop in the amplitude just before the resonant peak, and the amplitude before the resonance is also lower than the amplitude past the resonance. In this figure, the frequency detuning describes where the driving frequency and the harmonic frequency are the same, which is where the x-axis is 0, and the linewidth is 2 Hz. The broadband excitation frequency is swept from -20 Hz to 20 Hz. q is a dimensionless parameter which controls the asymmetry of the resonance.

Fano resonances can be classically modelled by two damped coupled harmonic oscillators in the weak coupling regime, with one of the oscillators also being driven [88]. If the oscillators are set up such that only the driven oscillator is damped and they have different natural frequencies (ω_1 and ω_2, where $\omega_1 < \omega_2$), then by coupling the oscillators, their natural frequencies are shifted by a factor proportional to the coupling parameter these new frequencies are $\bar{\omega}_1 < \omega_1$ and $\bar{\omega}_2 > \omega_2$. When the drive frequency of the driven oscillator passes through $\bar{\omega}_1$, a phase of π is imparted on the driven oscillator but not the free coupled oscillator. This change of phase causes the two oscillators to transition from being in phase and therefore constructively interfering to being out of phase and destructively interfering [86]. Therefore, when viewing the amplitude of the driven oscillator there is a symmetric peak when the drive frequency is equal to $\bar{\omega}_1$ but due to the imparted phase an asymmetric peak when the drive frequency is $\bar{\omega}_2$. In experimental systems, a Fano resonance arises from the interaction between a broadband excitation and a harmonic excitation. In the example the driven oscillator acts as a broadband excitation due to the damping and the free oscillator acts as a harmonic excitation.

In the work presented in Chapter 2 of this thesis, the broadband excitation is the laser-excited magnons, which are excited through two differing mechanisms, and the phonon excitation produces the harmonic excitation. The magnons excited in this work are out of phase below the phonon resonance and therefore destructively interfere. However, once the magnon eigenfrequency is raised above the phonon resonance, the magnons become in phase, producing constructive interference. This change in phase of the system and the lineshape of the magnon-phonon resonance suggests that a Fano resonance occurs.

1.7 ASOPS

ASOPS is an optical measurement technique that is used throughout this thesis. This technique utilises two lasers, which are the pump and probe, where the pump excites the sample, and the probe probes the changes in the sample from the excitation, including the change in the reflectivity and the change in the Kerr angle. The pump and probe have a small difference in the repetition rates, which is referred to as the offset frequency, which determines the time between the laser pulses, resynchronise and therefore defines the time resolution of the system.

The basic principle of ASOPS is illustrated in Figure 16. The two

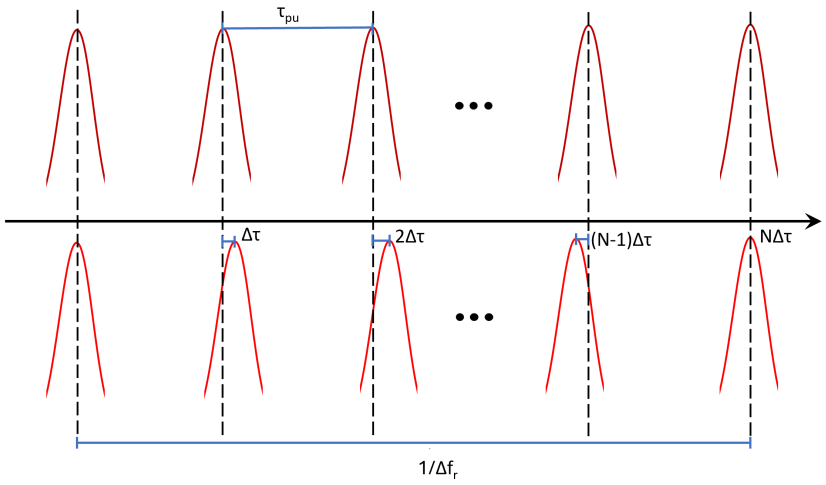


Figure 16: A schematic representation of the ASOPS measurement process. This figure illustrates the concept that the pump and probe lasers start with their pulses synchronised. Due to the difference in repetition rates between the two lasers, the first subsequent probe pulse arrives a time step of $\Delta\tau$ seconds after the pump. This process continues until the laser pulses realign after $1/\Delta f_r$ s [89].

laser pulses initially arrive at the sample simultaneously. However, due to the offset frequency between repetition rates of the pump and the probe, the second probe pulse arrives at the sample slightly behind the pump excitation. This process continues until the pump and probe synchronise their arrival again. This allows the sample to be probed at periodically spaced intervals following an excitation. The time between the two lasers resynchronising their arrivals is given by

$$\tau = \frac{\Delta f_r}{f_{r,\text{pump}}} t. \tag{65}$$

Where τ is the time between pulses, Δf_r is the offset frequency of the repetition rates between the lasers, $f_{r,\text{pump}}$ is the repetition rate of the pump laser, and t is the scan time, which is the time before the pulses resynchronise. For the ASOPS systems within this thesis, the scan time was 1.25 ms, and the time between pulses was 12.5 ns. To find the time resolution of the system

$$\Delta\tau = \frac{\Delta f_r}{f_{r,\text{pump}} f_{r,\text{probe}}}, \tag{66}$$

here, $f_{r,\text{probe}}$ is the repetition rate of the probe laser. This results in the time resolution being 0.125 ps.

1.8 Current Works in Magnon-Phonon and Phonon-Exciton Coupling

The strong coupling of quasiparticles is an area of interest due to the composite particle gaining properties of the constituent particles. These properties can include the particle's lifetime, tunability and polarisation, along with the coherent exchange of energy between each of the constituent particles.

In this thesis, the coupling of magnons and phonons to other quasiparticles is explored, which includes magnon-phonon, phonon-exciton, and magnon-phonon-photon coupling. The thesis builds upon previous work reported in the literature, as described below, in which these types of couplings have been investigated in bulk materials and nanoscale devices.

Magnon-phonon coupling in bulk structures, arising from the crossing of magnon and phonon dispersion curves, has been observed since 1968 [90]. Alloys of iron and nickel were used, with compositions ranging from $Ni_{0.81}Fe_{0.19}$ to $Ni_{0.65}Fe_{0.35}$, and each layer thickness was of the order 600 nm. For these experiments, the frequency range explored was 55 - 62.4 GHz. In this experiment, each of the films was cooled to 77 K and a microwave driving field was applied to each film at the frequencies previously mentioned. The difference between the measured magnetic field that induces a resonance for a chosen magnon mode and the expected magnetic field that induces a resonance calculated from the dispersion relation, defined as ΔH, is shown against the driving field frequency in Figure 2 of [90]. The greater the deviation of ΔH, the stronger the magnetoelastic coupling of the measured mode, as a deviation of 0 suggests there is no magnon-phonon interaction. The strongest coupling was measured in a film with composition $Ni_{70}Fe_{30}$, and the 24th-order spin wave mode is excited by microwave frequencies of 58.5 GHz and 62.2 GHz. This resulted in the strongest deviation from the uncoupled spin wave resonance, with ΔH being $\approx$ -50 Oe and $\approx$ 40 Oe, respectively. This work justifies the further exploration of magnon-phonon coupling.

More recently, magnon-phonon coupling effects have been observed in nanostructures, where the frequencies of the phonons can be tuned by confinement. Strong coupling has been shown in different nanostructures. One of these nanostructures is a nanomagnet, which has been achieved by [91, 92]. The first group used a nickel nanomagnet [91] with dimensions $330\times330\times30$ nm^3. The phonon modes are excited optically using a pump-probe type apparatus with a pump wavelength of 400 nm and a probe wavelength of 800 nm.

The excited phonons then couple to the magnons, which are tuned via an externally applied magnetic field which varies from 1 - 5 kOe. The phonon frequency is determined by the type of strain which produces the phonon (compressive or shear). There are three phonon modes which are detectable in this nanomagnet, with frequencies of $\approx$ 8, 11, 14.5 GHz. These phonon modes are characterised by indices (1,0), (1,1) and (2,0) respectively. The indices describe the direction of in-plane propagation (x, y). Phonon mode (2,0) is of particular interest, as when the in-plane component of the magnetisation of the nanomagnet is aligned with the wavevector of these phonon modes, the cooperativity, $C = \kappa^2/\lambda_1\lambda_2$ (where κ is the coupling strength and λ_i is the decay rate of each excitation), is 0.74, which is below the strong coupling regime at C = 1. However, when the angle between the in-plane component of the magnetisation and the wavevector is 45°, the cooperativity is increased to 1.65, which shows that the coupling of magnons and phonons is dependent on the in-plane angle and on the external magnetic field.

The other work utilising nanomagnets [92] used the magnetic material CoFe with dimensions 210×210×30 nm^3. The CoFe was prepared in both the polycrystalline phase and the single-crystal phase. The experimental setup is the same as in [91]. The phonons of interest in this work are the (1,0) and the (1,1) phonons with frequencies 13.6 and 20.7 GHz, respectively. The magnetic field was swept from 3 - 6 kOe and the in-plane angle between the magnetisation and the phonon wavevectors was 0°. For the polycrystalline CoFe, the (1,1) phonon exhibited the anticrossing connected to strong coupling, and the cooperativity was calculated to be 20. In the single-crystal CoFe, the (1,0) phonon strongly couples to the magnons with a cooperativity of 38. This shows that stronger magnon-phonon coupling occurs in single-crystal samples, but the phenomenon can also occur in polycrystalline materials.

Another type of nanostructure used to observe strong magnon-phonon coupling was shown by [1]. This work looked at nanogratings, where the periodicity of the nanograting determines the frequencies of the surface acoustic wave phonons, which are confined within the phonon cavity. The period was 200 nm in the [010] direction, which confines the static magnetisation to the [100] direction, which is an easy magnetic axis for this material. The corresponding phonon frequencies were 13 and 15 GHz for the transverse and longitudinal phonons, respectively. The magnetic material chosen was galfenol, due to its high magnetostriction [43]. Again, this experiment optically excites the phonons, which couple to the magnons. In this case, the pump and probe wavelengths were 1040 and 780

nm, respectively. The magnetic field was varied from 0 - 250 mT and was applied along the [110] direction. The measured cooperativity of the transverse phonon mode and the magnon mode was 7.8, which firmly lies in the strong coupling regime.

There are also examples of weakly coupled interactions (cooperativity < 1) between magnons and phonons that can be advantageous for observing interference-based effects, including tunable Fano interferences [93]. Z. Shen et al examined yttrium iron garnet (YIG) microspheres and opal silica microspheres in contact. For this experiment, the YIG spheres are excited via a vector network analyser, producing microwave frequency photons that excite both magnons and phonons in the YIG sphere, whereas the opal silica sphere is excited via a laser pulse. This shows that increasing the power of the microwave photons causes the system to evolve from the laser exciting phonons in the opal sphere, which then excites phonons in the YIG sphere at powers up to 3.2 mW. Above this power threshold, the microwave photons become the driving force, and the magnons are first excited in the YIG sphere, which drives the phonons in the YIG before transferring into the opal sphere. Figure 17 shows a schematic of the experimental setup. The work goes further and looks at changing the phase of the microwave drive and observes that when the phase is between 0 and π a Fano resonance interaction occurs between the phonons produced in the two spheres. This type of interaction is expanded on in this thesis with a Fano resonance produced directly between the magnon-phonon system, where the phase is tuned via the input power of the laser used to excite the system.

Due to the recent observation of strong magnon-phonon coupling in confined structures by C. Berk et al [91] and F. Godejohann et al [1], there is now interest in further strongly coupling these systems with photons, with work being conducted [94]. R.C. Shen et al used an optical cavity containing a YIG sphere, where the sphere is used to confine both the magnons and the phonons and observed a cooperativity of 9400, this suggests they have shown ultrastrong coupling is possible. The resonant frequency of the phonons and the cavity is 7.2 GHz, and the magnetic field (which is applied out of the plane of the cavity) is 257 mT. The cavity has dimensions $60\times25\times6$ mm^3 and the YIG sphere has a diameter of 0.25 mm. Based on the dimensions of the cavity and the operational frequency, this would be too large to work as an on-chip-based device; however, the cavity and phonon frequencies are close to the 10 GHz range of interest in this thesis.

To explore other options to achieve on-chip strong magnon-pho-

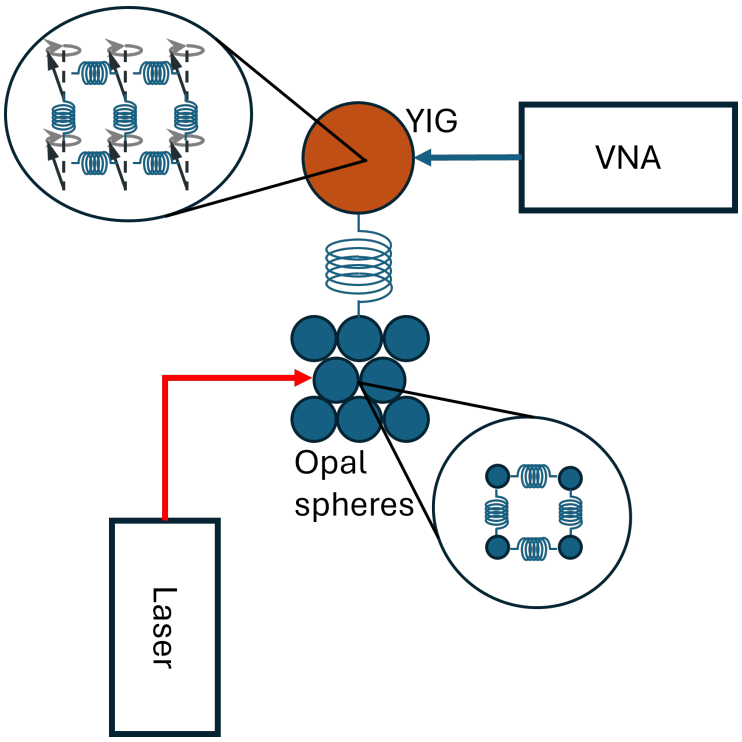


Figure 17: A schematic for the experiment undertaken by Z. Shen et al [93]. A yttrium iron garnet (YIG) sphere is placed on top of an opal microsphere substrate. The YIG sphere is excited via a microwave frequency photon from a vector network analyser (VNA); this results in both magnon and phonon excitations within the YIG sphere, and the phonons are able to pass into the opal. Furthermore, a laser is used to excite phonons in the opal, which then pass into the YIG and further excite the magnons.

non-photon coupling, works which accomplish strong magnon-photon coupling should be discussed. Coplanar waveguide geometries can be used to produce on-chip devices which exhibit strong magnon-photon coupling [95, 96, 97, 98, 99]. The work by Y. Li et al [96] uses a layer of permalloy with lateral dimensions 14×900 μm^2 and thickness 30 nm along with a superconducting niobium meandering coplanar waveguide with a resonant frequency of 5 GHz. The system was cooled to 1.4 K, and an external field is swept from -100 to 100 mT at 45° to the permalloy bar. At $\approx$ 20 mT the microwave photons strongly couple to the magnons with a cooperativity of 68. This work shows the dimensions of microwave-excited devices are much more suited for on-chip devices.

The work by IW. Haygood et al [97] again looked at superconducting coplanar waveguides; however, the waveguide used in these works was designed to have a resonant frequency of 13 GHz, allowing it to be smaller and have a resonant frequency closer to the region of interest. The material this group chose to use was $Fe_{75}Co_{25}$ due to its ultralow damping. It was observed that for a fixed volume of magnetic material (192 μm^3), by decreasing the centre width of the coplanar waveguide, the coupling strength increases from 100 MHz at 50 μm to 700 MHz at 6 μm, which results in a cooperativity at 6 μm of 720. The work in this thesis looks at the viability of using a microwave antenna instead of a waveguide to excite magnons and phonons in a galfenol stripe with a nanograting patterned into the surface. This is due to the much simpler fabrication and design steps, as well as the broader operational frequencies.

There are works that also explore the strong coupling interaction between excitons and phonons [100, 101]. Within these works, the experimental setup is a pump-probe type setup designed to utilise transient absorption spectroscopy. This technique requires a pump laser to excite the sample, where the wavelengths used in these works are 520 nm [100] and 532 nm [101]. Then, a spectrum of light is used as a probe to explore the absorption or photoluminescence spectra of the excited sample. Figure 18 shows the transient absorption spectroscopy experimental scheme. The internal energy of the sample can be varied in a multitude of ways, such as the temperature, as in [100], or the pump laser power, as in [101]. The results of these works produce photoluminescence plots, where excited particles decay and emit light with frequencies proportional to their energy. To explore coupling between systems, another parameter related to the system of interest can be varied in order to observe its impact on the spectra. For the case of phonon-exciton coupling, the excitons are excited when the probe energy is the same as the exciton excitation

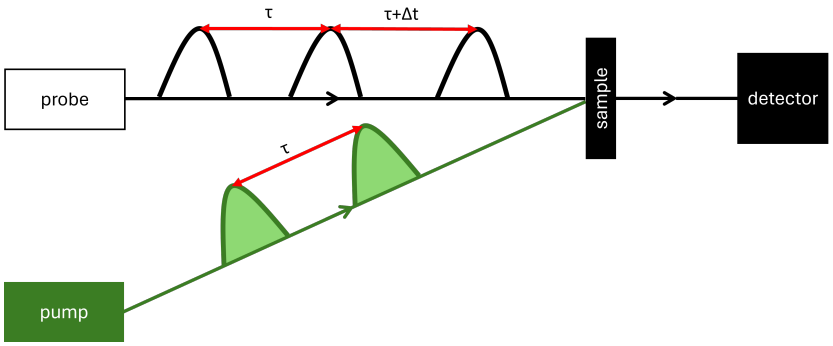


Figure 18: A general transient absorption spectroscopy setup utilising pump-probe techniques. The pump laser is used to excite the sample of interest. A source of multiple wavelengths is then used to probe the sample and observe the absorption spectrum. Furthermore, the setup uses a time delay between the pump and the probe such that the time dependence of the absorption spectrum can also be observed.

energy. To explore phonon-exciton coupling, the photoluminescence data is Fourier transformed. The strong coupling is observed in the transformed data as a nulling of the exciton excitation amplitude; if the exciton peak is broader than the phonon peak, it can also be observed as a splitting of the exciton excitation. The nulling occurs due to the newly formed combined particle no longer having the same energy as either composite particle alone.

K. Lin et al showed that [100], two materials are explored, the first being butylammonium lead iodide, which shows strong coupling between excitons and phonons with the phonon wavevector being 100 cm^{-1}, and the probe energy is between 600 - 625 nm. The second material was hexylammonium lead iodide, which exhibits weak coupling between two different phonons and excitons since no splitting occurs in the spectra, the excited phonon modes have wavevectors of 88 and 137 cm^{-1}. The works in this thesis explore a weak-coupling effect whereby strain, layer thickness, and the Bragg condition increase the sensitivity of phonon detection via the generation and decay of excitons.

2 Fano-like Interference Effects in a Coupled Magnon-Phonon Resonator

2.1 Introduction

This research was published in Physical Review Research [102] as hybrid coherent control of magnons in a ferromagnetic phononic resonator excited by laser pulses. The experimental measurements, results and analysis described in this chapter were conducted by the author in the laboratories of the Acoustics group at the Technical University of Dortmund under the supervision of Dr A. V. Scherbakov. The sample deposition and fabrication were carried out by A. Nadzeyka and A. W. Rushforth. Finally, the theoretical understanding was produced by T. L. Linnik. S. M. Kukhtaruk and A. D. Armour.

Magnon-phonon coupling is an emerging area of research due to the recent discovery of strong magnon-phonon coupling in a nanostructure [1, 91]. This previous work explored coupling in the magnetic material galfenol using nanostructures fabricated on the material's surface. Other recent work looks at using magnon-phonon coupling to produce high-sensitivity magnetic field sensors [103], subharmonic magnon generation [104], strong coupling in magnetic van der Waals materials [105] and on-chip hybrid systems [106]. Building on previous work, the effect of laser fluence on the excitation of magnon modes in magnetic structures with an acoustic resonator fabricated into the surface is explored.

For high laser fluence, this results in a Fano-like resonance that suppresses the magnon amplitude when the magnon frequency is 0.4 GHz detuned below the phonon resonance frequency, and amplifies the magnon amplitude when the magnon frequency is above the phonon frequency. However, for low laser fluence, the magnon amplitude follows the expected gradual decrease in amplitude with increasing external magnetic field. The amplification and suppression of the magnon signal in the high fluence case provides evidence of a Fano-like interaction. Fano interference requires both harmonic and broadband excitation of the system.

Within this work, the photons are used to excite both magnons and phonons in the structure. The phonons at the frequency of the acoustic resonator provide a finite-lifetime, quasi-harmonic excitation of the magnons. The laser pulse provides a broadband excitation to the magnons by inducing ultrafast electron-based effects, including demagnetising effects and spin current generation. These different methods of magnon generation are controlled via the

laser fluence, and each method produces magnons with a different phase. The difference in the origin of magnon excitation allows the phase relation and the eigenfrequency detuning between phonon and magnon excitation to be controlled, producing a Fano-like spectrum.

The appearance of the Fano interference, only at the high fluences, shows that the effect of increasing the fluence of the laser changes the phase of the initial magnon, thereby allowing for the interference effects to be tuned. Potential applications of this Fano-like interference effect include sensing applications, including use in temperature sensors [107, 108, 109, 110] and refractive index sensors [111, 112, 113]. Other applications of Fano interference include lasing [114] and hybrid coherent control of magnons mediated by photon fluence, analogous to coherent control in other systems. Examples of systems which could take advantage of hybrid coherent control include: multiple photonic cavities [115], single photonic cavities coupled to a mechanical oscillator [116], single spins [117, 118], spin ensembles [119], magnon-phonon and magnon-photon systems [120, 121, 122], spin-valve ferromagnetic structures [123], antiferromagnetic magnons [124, 125] and hydrogen molecules [126]. Advancements in hybrid coherent control systems can further quantum computing and communication technologies [127].

2.2 Methods

2.2.1 Set-up

This experiment makes use of ultrafast optical measurements, using a pump-probe type setup. The full optical setup is shown in Figure 19, where two TOPTICA Yb-doped fibre ring harmonic oscillator lasers are used. The pump laser has a central wavelength of 1050 nm, a repetition rate of 80 MHz, a 150 fs pulse duration, a spot diameter of 3 μm and a fluence varying from 1 - 10 mJ/cm^2. The probe laser is initially linearly polarised via a Glan-Taylor prism. It has a central wavelength of 780 nm, a repetition rate of 80 MHz, a 150 fs pulse duration, a spot diameter of 1 μm and a fluence of 1 mJ/cm^2.

A synchronisation unit from Laser Quantum is used to maintain an offset frequency of 800 Hz between the repetition rates of the two lasers. This experiment uses a backside excitation scheme since the pump photon energy is not great enough to surpass the band gap energy of GaAs, which results in the GaAs substrate being transparent from the perspective of the photon. The use of the backside excitation scheme means that two microscope objectives were used, which were both Mitutoyo NIR 20x lenses. The position

of the backside objective is adjusted manually, whereas the frontside objective is mounted on a piezotranslator (piezosystem jena, NV40 3CLE, Tritor 101), which is used to fine-tune the position of the laser spot. This translator features three-dimensional travel, with 100 µm of movement in each axis.

Both the light reflected off the sample and the light modified by the sample are detected by a balanced photoreceiver (Newport balanced photoreceiver, model 2107) (BPR). The BPR is set such that the low-pass filter is 100 Hz, the high-pass filter is 10 MHz, and the gain is set to 100. The low-pass filter is also set to the DC setting to measure the DC reflectivity while the pump laser is blocked. An oscilloscope (Techtronix DPO 5104) is connected to the BPR in order to read the electrical signal from the BPR. There are also non-polarising beam splitter cubes and a half-waveplate paired with a Wollaston prism, converting the elliptically polarised reflected light into linearly polarised light with s and p-polarisation components, which are separated by the Wollaston prism. To control the magnon frequency, a water-cooled dipole electromagnet (GMW, 3480) is placed around the sample, with a power supply (Ametek, XG 60-28) controlling the current and thereby the applied field. The field was varied between 200 and 400 mT in 10 mT steps. The pump excites the sample, and the probe laser periodically probes the sample; this is the ASOPS technique mentioned in Chapter 1.7. In this case, due to the bandwidth of the BPR being smaller than the repetition rate of the probe laser, the BPR bandwidth limits the resolution such that the time resolution is no longer given by equation 66, but is given by

$$\Delta\tau = \frac{\Delta f_r}{f_{r,\mathrm{pump}}} B^{-1} \tag{67}$$

where B is the bandwidth of the BPR, which changes the time resolution to be 1 ps.

Within this experiment, time-resolved polar MOKE (Chapter 1.2.8) is exploited to produce circularly polarised light, such that when the Wollaston prism is placed before the BPR, the s and p polarisations of the light are separated and received by the different detectors in the BPR. This allows the change in Kerr angle to be measured, which is equivalent to measuring the out-of-plane magnetisation component and, therefore, the spin wave oscillations. By placing a half-waveplate before the Wollaston prism, the polarisation of the light can be adjusted such that only one polarisation of the reflected light is maximised; this results in only one of the BPR detectors being used, which allows the change in intensity to be measured and allows for the phonon oscillations to be recorded

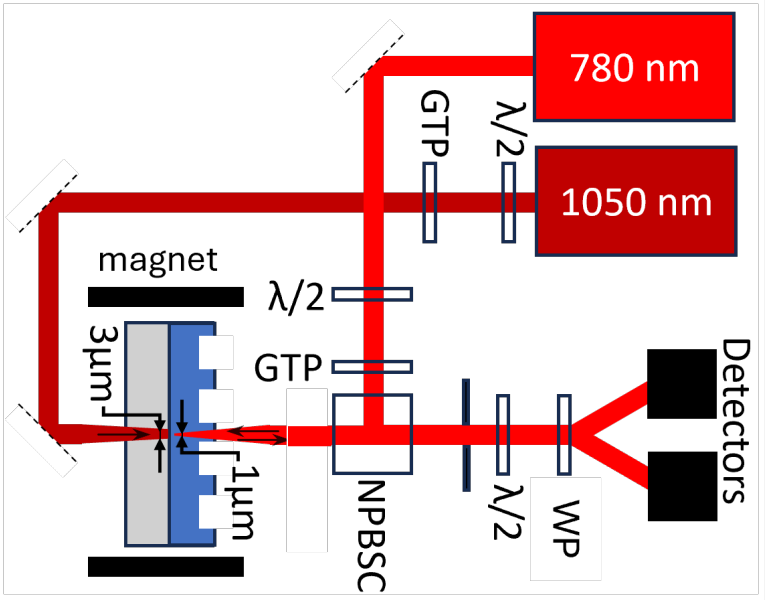


Figure 19: A schematic showing the ASOPS setup used for this experiment. The probe wavelength is 780 nm, and the pump is 1050 nm. The spot size of the pump was 3 μm, and the probe was 1 μm. A balanced photoresistor setup is used to detect the change in intensity and the change in Kerr angle. NPBSC is a non-polarising beam splitter cube, $\lambda/2$ is a waveplate, GTP is a Glan-Taylor prism, and WP is a Wollaston prism. The $\lambda/2$ and WP combination before the balanced photodetector allows for the phonon measurement scheme and magnon measurement scheme to be switched between without changing the WP.

after some processing, which will be elaborated on in Chapter 2.2.3.

2.2.2 Materials

The sample used was fabricated from a 20 nm layer of galfenol ($Fe_{0.81}Ga_{0.19}$), due to previous works [128] showing that the absorption depths of the pump and probe are 19 and 21 nm, respectively. The galfenol was deposited onto the GaAs substrate. The galfenol was produced by Dr Andrew Rushforth using DC magnetron sputtering. The sputtering process requires the chamber to be kept under ultra-high vacuum conditions until the sputtering takes place, when argon is injected into an electrically grounded shroud and then, due to the material being sputtered, a DC field is applied with a power of 27 W, which results in the argon becoming an ionised plasma. The sputtering head acts as a cathode, attracting argon ions, which results in bombardment of the target's surface and allows for the ejection of material from the target. To improve the efficiency of this process, magnets are placed within the sputtering head to produce a field perpendicular to the sputtering head surface [129]. This field is used to contain the argon plasma. The target material is deposited on the substrate, which is placed above the target, at a rate of 0.3 $Å s^{-1}$ until the sample is 20 nm thick.

Following this, a 3 nm Chromium capping layer is sputtered on top to prevent oxidation. To prepare the substrate for the sputtering process, the GaAs [001] substrate is first etched in HCl to remove any oxides that may have formed and then annealed at 500°C for 1 hour in ultra-high vacuum conditions; this provides a clean and smooth surface ready for deposition, which is speculated to be due to thermal desorption [130]; however, this has not been confirmed with these samples. The GaAs substrate was oriented with the surface in the [001] direction, which causes the surface layer of the GaAs to have a face-centred cubic crystal structure, which is similar to the surface of the $D0_3$ crystal structure of the composition of galfenol used. The lattice constant of GaAs is $a_0 = 0.565$ nm, and the out-of-plane lattice constant for galfenol is a = 0.287 nm. Therefore, the lattice matching between the two materials is 1.6%, which is low enough to ensure consistent growth of single-crystal thin films of galfenol (via molecular beam epitaxy as well as sputtering) with few dislocations and little impact on the internal strain of the galfenol layer but does induce a magnetic uniaxial anisotropy [131, 132]. Previous work conducted shows that the growth strain relaxes at the edges of the layer [36].

The sample was then ion-milled to produce nanogratings. The

ion milling was done via an external company, Raith nanofabrication, using their Raith Velion FIB-SEM (focused ion beam-scanning electron microscopy) system. The process uses Ga^+ ions to mill into the sample surface with sub-10 nm cutting resolution. The Raith process is automated and resistless due to the SEM attachment and the laser interferometer stage providing visual and translational feedback, which allows the mask design to be milled without affecting the surrounding areas. FIB milling utilises a similar process to SEM, where a beam of charged particles is focused into a beam and accelerated towards the sample surface by a larger potential difference. In this case, the charged particles are heavier than electrons. Therefore, they experience less scattering [133]. The acceleration voltage used was 35 kV with a beam current of 5.5 pA and a dose of 0.06 nC/μm^2 [134]. This ejects unwanted material from the surface. The resulting nanogratings have a period of 120 nm, with trough depths and widths of 7 nm and 48 nm, respectively. A scanning electron microscope (SEM) image of the nanograting is shown in Figure 20

2.2.3 Techniques

10000 averages of each of the time traces are taken to provide a good signal-to-noise ratio. For the intensity measurements, the thermal background must first be removed. This background is due to the pump pulse thermally exciting electrons and further electron-electron scattering. This energy is transferred to the lattice after a few ps [135]. This lattice excitation is the origin of the phonons. The energy transfer for the electrons to the lattice is given by a pair of coupled equations:

$$\begin{aligned} C_e\frac{\partial T_e}{\partial t} &= \kappa_e\frac{\partial^2 T_e}{\partial z^2} - g(T_e - T_l) + P(z,t) \\ C_l\frac{\partial T_l}{\partial t} &= g(T_e - T_l) \quad [135]. \end{aligned} \tag{68}$$

where C_e is the electron heat capacity, C_l is the lattice heat capacity, T_e is the electron temperature, T_l is the lattice temperature, κ_e is the electron thermal conductivity, g is the electron lattice coupling factor, and P(z,t) is a source term representing the laser pulse. This thermal background is removed by fitting the time trace beyond the initial intensity increase with exponential decay functions. The residuals of this fitting process result in purely the phonon excitation, where the time trace, fitting, and the residuals are shown in Figure 21. The time trace can then be Fourier transformed to find the frequency components using a rectangular window. Since the

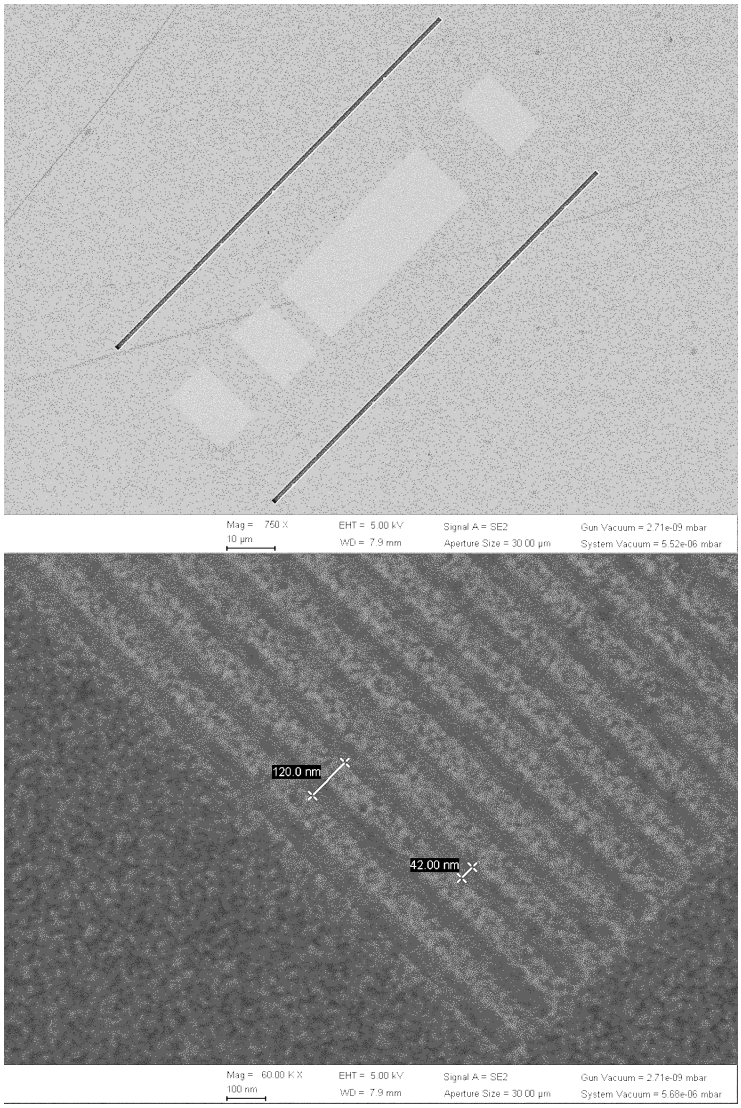


Figure 20: Scanning electron microscope images of the nanogratings in a galfenol sample; the contrast and brightness have been increased for increased visibility of the gratings. Top: 750x magnification showing all the gratings in the sample and the deeper grooves to locate the gratings. Bottom: 60000x magnification showing the period of the grating and the trough width.

measurements are taken on the nanograting, only phonon modes localised to this nanograting are excited. This suggests that the excited phonons are Rayleigh-type surface waves and that their frequencies are determined by the nanograting milled into the surface. A simplified calculation can give a rough estimate for the phonon frequency by taking the speed of sound in galfenol, v, as 4879 ms^{-1} [136] and the period of the grating, P, as 120 nm, the frequency is then $v/2P$ this results in the frequency being $\approx$ 20 GHz, which is in agreement with the experimental results. This rough calculation matching the experimental results provides strong evidence the detected phonon is a surface wave since the speed of sound is halved for surface waves compared to bulk waves [81].

Away from the grating surface, acoustic waves are still excited due to the thickness of the sample; however, the frequency is not limited by the periodicity of the nanograting. There is a second frequency in the intensity signal at $\approx$ 45 GHz; these are Brillouin oscillations. Brillouin oscillations occur when the propagation length of the probe pulse is greater than the thickness of the excited film. The probe penetration depth was determined to be 20 nm [128], which is the thickness of the sample. This results in the probe photons interacting with the longitudinal phonons in the GaAs substrate. Due to the different material properties of the substrate, the oscillations observed are of a different frequency, given by

$$f_{Brill} = \frac{2n_{GaAs}v}{\lambda_{pr}} \tag{69}$$

where n_{GaAs} is the refractive index of GaAs equal to 3.679, v is the longitudinal speed of sound in GaAs and equal to 4.731 nm/ps [137]. This results in a Brillouin oscillation frequency of 45 GHz, which is in agreement with the experimental results. The magnon signal is collected via measuring the change in the Kerr angle; this measurement does not require any background removal process, and the Fourier transform can be done directly. An example of a magnon time trace and Fourier transform is shown in Figure 22. The frequency of the magnon excitation can be directly controlled by the external magnetic field.

2.3 Results

By increasing the magnetic field and collecting the Fourier transforms of the magnon signals, a colour map can be produced, which shows how the magnon resonance changes with respect to the increasing field. The amplitude of excitation is shown by the colour.

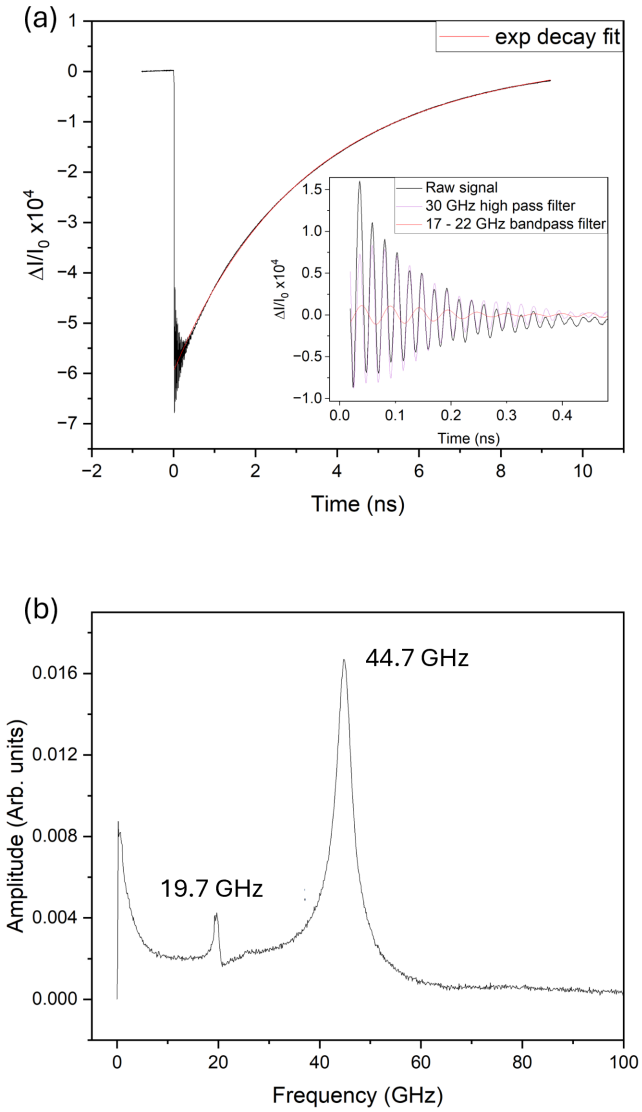


Figure 21: (a) shows an example of a time-resolved fractional change of probe intensity when the ASOPS system is configured to measure the change in intensity. This figure also shows the exponential fitting applied to the time trace to remove the thermal background. The inset shows the results of the residuals after the fit values are removed, along with two frequency filters to separate the Rayleigh mode (red) and the Brillouin oscillation (purple) (b) shows the FFT of the residuals, which separate the frequency components. This shows the Brillouin oscillations are at 44.7 GHz and the Rayleigh mode phonons are at 19.7 GHz. Both these figures correspond to a pump fluence of 10 mJ/cm^2.

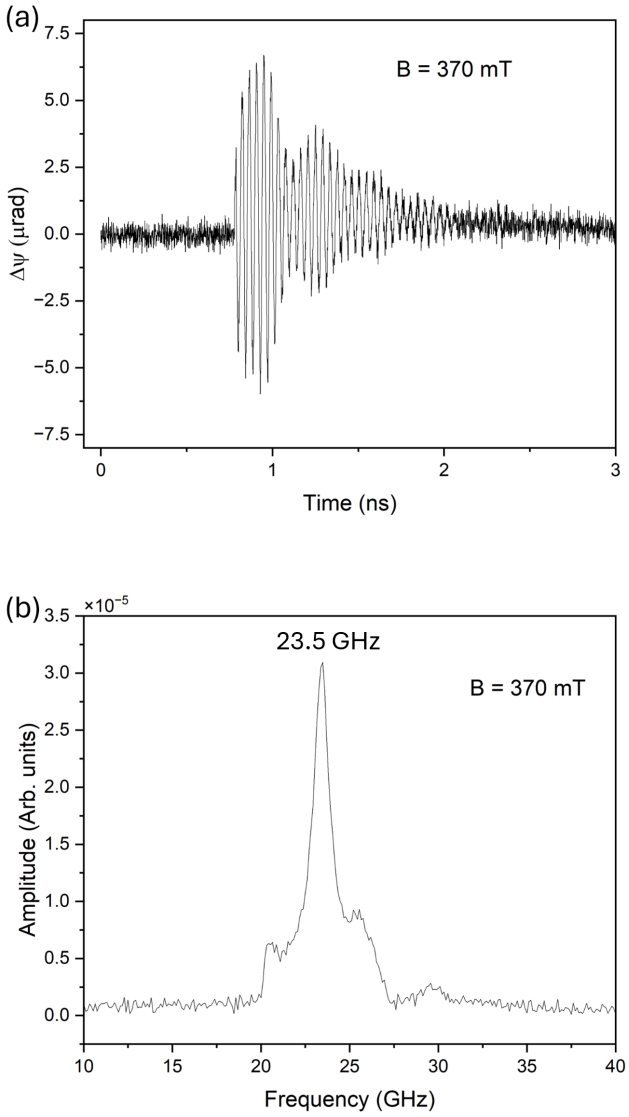


Figure 22: (a) shows an example of a time-resolved difference between the s and p polarisations of the probe beam when the ASOPS systems are configured to measure the change of the Kerr angle. This time trace was specifically measured when the magnetic field was set to 370 mT. (b) shows the FFT of the time trace. The frequency of the magnon at 370 mT is approximately 23 GHz. Both these figures correspond to a pump fluence of 10 mJ/cm^2. The sidebands which appear here are due to the laser excited magnons whereas the peak is due to phonon driven magnons.

For a laser fluence of 1.2 mJ/cm^2, the magnetic field was swept from 230 - 325 mT, in 5 mT steps. This allows for waterfall plots (Figure 23(a)) and a colour map (Figure 23(b)) to be produced, which show the dependence of the measured amplitude of the magnetisation precession (i.e. magnons) on magnetic field. The resonant magnon excitation is shown as light blue or green, and the excitation follows a close to linear relation. The colour map further shows the interaction between the magnons and phonons, which appears as a bright spot. Strong coupling would be observed as an anticrossing in the colour map, as shown in [1]. This suggests that we have a weakly coupled driving interaction where the phonons drive the magnons.

This data can also be used to plot the amplitude change of the magnons as the magnetic field is increased from 250 - 310 mT, this follows the line f_0, which includes the phonon interaction at 260 mT (Figure 23(c)), which shows the increase in amplitude due to the phonon interaction but also shows the decrease in amplitude after the resonant interaction. The FFT of the magnon amplitude at 250 mT, where the detuning between the phonon and magnon frequencies is 0.4 GHz, is presented in Figure 23(d). Increasing the laser fluence to 10 mJ/cm^2, the same experiment was undertaken with the magnetic field range used being 200 - 400 mT, with the magnetic field increasing in 10 mT steps. This allows the same figures as previously to be produced (Figures 24(a)-(d)). Figure 24(b) again shows a colour map, which suggests again that the magnon-phonon interaction is only in the weak coupling regime. However, there is also a region where the magnon-phonon detuning is 0.4 GHz, where the amplitude of the magnon excitation is decreased. Figure 24(c) further shows that there is a decrease in the amplitude of the magnon excitation before the phonon interaction at 270 mT. This also shows that the amplitude of the magnon excitation decreases after crossing the phonon excitation, but the amplitude doesn't return to the value before crossing the phonon resonance.

If Figure 23(d) is compared to Figure 24(d), the shape of the excitation is different, with the low fluence example being the typical case, taking a more symmetric excitation, and the high fluence example taking a Fano-like interaction shape, which is asymmetric in nature. The cause of this Fano-like interaction will be explained in the following theory section.

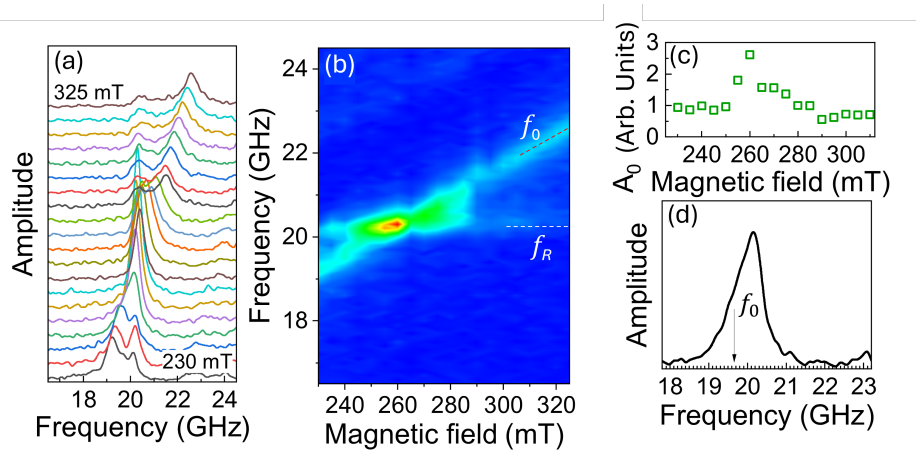


Figure 23: (a) Waterfall plot showing the magnon FFT figures offset from each other from 230 - 325 mT, when the laser fluence is 1.2 mJcm^{-2} (b) shows a colour map, where the magnon resonance is plotted labelled by f_0 and the phonon resonance is labelled by f_R. This plot shows that the magnon-phonon interaction shows weak coupling between the two quasi-particles. (c) shows the amplitude of the magnon resonance when the applied magnetic field is increased from 230 - 310 mT, this follows the line f_0, which includes the phonon resonance interaction, which occurs at 260 mT. (d) shows the FFT of the magnon time trace at an applied field of 250 mT, where the detuning of the magnon frequency from the phonon frequency is 0.4 GHz.

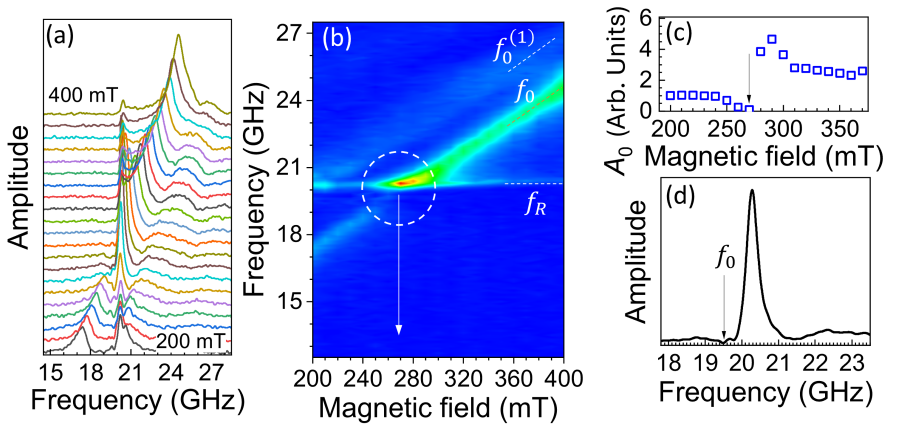


Figure 24: (a) Waterfall plot showing all the magnon FFT figures offset from each other from 200 - 400 mT, when the pump laser fluence is 10 mJcm^{-2}. (b) shows a colourmap, where the resonance of the first magnon mode is plotted, labelled by f_0. The resonance of the second magnon mode is plotted and labelled by $f_0^{(1)}$. The phonon resonance is labelled by f_R. This plot shows that the magnon-phonon interaction shows weak coupling between the two quasi-particles. (c) shows the amplitude of the magnon resonance when the applied magnetic field is increased from 200 - 370 mT, this follows the line f_0. The reduction of the amplitude before the phonon resonance is labelled by the arrow. (d) shows the FFT of the magnon time trace at an applied field of 250 mT, where the detuning of the magnon frequency from the phonon frequency is 0.4 GHz, there is nulling of the magnon amplitude observed as well as the resonance taking a more asymmetric shape than Figure 23

2.4 Simulation and Modelling of Rayleigh Waves and Magnon Modes in Galfenol Nanogratings

The modelling of the grating structure using COMSOL [138] was accomplished by Dr Serhii M Kukhtaruk, with the LLG analysis being conducted by Dr Tatiana L Linnik and Dr Andrew D Armour. These results are reproduced with their permission.

From the COMSOL modelling, a spatial profile of the strain components of the ground-state phonon mode can be produced, with the expected wavevector of the Rayleigh wave being $q = 2\pi/d$, where d is the period of the nanograting. Input parameters for the simulation include the elastic coefficients, c_{ij}, and the density, ρ, of the galfenol and the GaAs. For these we took the values from the literature: $c_{11}^{Galf} = 193$ GPa, $c_{12}^{Galf} = 156$ GPa, $c_{44}^{Galf} = 123$ GPa and $\rho^{Galf} = 7800$ kg/m^3 [43]. Due to the ion milling process, which used Ga^+ ions, it is theorised that the grooves have a higher concentration of Ga from implantation, which affects the elastic coefficients; however, because the amount of material affected is small, the effect on the results is negligible. $c_{11}^{GaAs} = 119$ GPa, $c_{12}^{GaAs} = 53.8$ GPa, $c_{44}^{GaAs} = 59.5$ GPa and $\rho^{GaAs} = 5316$ kg/m^3 [137]. This produces a phonon mode at 20.2 GHz, consistent with the experimental results.

The spatial distributions of the components of the strain tensor from this simulation are presented in Figure 25. This figure shows the dominant strain components, being ε_{xx}, ε_{zz} and ε_{xz}. Of these components, it can be seen that ε_{xz} is predominantly confined to the GaAs substrate, and since the applied magnetic field is in the plane of the sample, the out-of-plane strain component, ε_{zz}, will have little effect on the effective magnetic field. Therefore, the main strain component of interest is ε_{xx}.

The COMSOL software is also used to model the magnon modes within the nanograting. To model the LLG equations, a micromagnetic package was produced by Serhii M Kukhtaruk [139]. By first assuming that the gallium concentration in the milled and unmilled areas is constant at 19%, The material parameters needed for $Fe_{0.81}Ga_{0.19}$ are: the saturation magnetisation $\mu_0 M_0 = 1.65$ T; the exchange constant A = 18 pJ/m; the cubic and uniaxial anisotropies $K_c = K_u = 35$ kJ/m^3 [140]. These parameters do not fit the experimental data for the two lowest frequency magnon modes, f_0 and $f_0^{(1)}$, but were chosen because they agree with previously reported values for the same composition of galfenol [140].

Since the nanograting was milled with Ga^+ ions, the implantation of gallium into the milled areas suggests that the model should

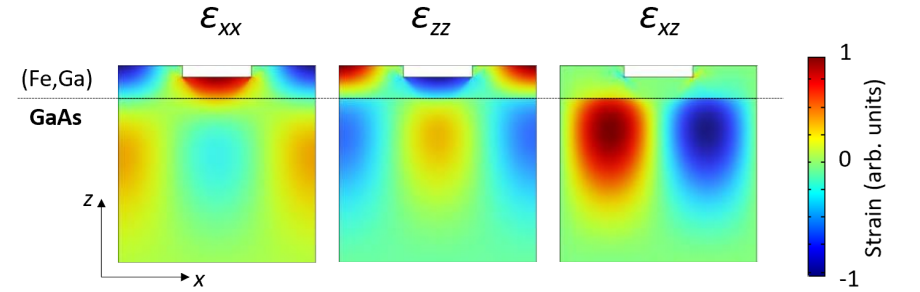


Figure 25: The simulated spatial distributions of the strain within the galfenol layers and the GaAs substrate calculated via COMSOL. Here, the colour scale shows the amplitude of the strain, with green being defined as zero strain, and then red being positive strain and blue being negative strain. The ε_{xx}, ε_{zz} and ε_{xz} are are the dominant components of the strain tensor. This also shows that the xz component is confined to the substrate, and that the xx and zz components have a seemingly inverse relationship. The elastic coefficients and densities used were: $c_{11}^{galf} = 193$ GPa, $c_{12}^{galf} = 156$ GPa, $c_{44}^{galf} = 123$ GPa, $\rho^{galf} = 7800$ Kg/m^3, $c_{11}^{GaAs} = 119$ GPa, $c_{12}^{GaAs} = 53.8$ GPa, $C_{44}^{GaAs} = 59.5$ GPa, and $\rho^{GaAs} = 5316$ Kg/m^3. The effect of the gallium implantation is negligible due to the thickness of the galfenol being much smaller than the phonon wavelength.

have the milled areas with a higher gallium concentration. The model provided the best fit when the gallium concentration in the milled areas is 39%; however, further work is required to measure this. For this composition of galfenol, the saturation magnetisation $\mu_0 M_0^* = 0.75$ T and the exchange constant is $A^* = 1.2$ pJ/m [141]. The results of the model with a higher gallium concentration is shown in Figure 26, this figure also shows the initial results with the concentration of gallium remaining constant, which shows that the effect of having the milled regions with a lower concentration of gallium reduces the eigenfrequencies of the modes and the difference in frequency between the different magnon modes.

The model also produced the spatial distribution shown in the upper inset of Figure 26, which shows that the magnon modes are both confined to the milled regions, which is similar to the ε_{xx} distribution shown in Figure 25. Due to the spatial overlap of the magnons and ε_{xx} strain component, it is determined that this component of the strain is responsible for the quasi-harmonic phonon excitation of the magnons.

The lower inset in Figure 26 shows a simulated spatial distribution of the electron temperatures 100 fs after the laser excitation with the fluence of 10 mJ/cm^2 in the galfenol layer. This shows that the temperature of the milled region is above 1000 K, which is above the Curie temperature of $Fe_{0.81}Ga_{0.19}$, $T_c = 973$ K [142]. It is also known that for galfenol, increasing the gallium concentration decreases the Curie temperature [143], which suggests that the entirety of the milled region is non-magnetic 100 fs after the optical excitation. This non-uniform heating of the nanograting paired with the non-uniform nature of the steady-state orientation of the magnetisation in the nanograting due to the complex dependence of the demagnetising field's spatial profile on the external field direction [139] leads to spin diffusion between the two nanograting regions, which dominates the broadband optical excitation of the magnons for the high pump fluence [144, 145, 146, 123, 147, 148, 149]. The complexities of this method of excitation are an ongoing area of research [150].

The dynamics of the magnons were modelled using the LLG equation 28. To solve the LLG equation, the magnetic free energy must first be defined to calculate the effective field given by equation 31. For this model, the only terms that are used are the uniaxial anisotropy, the Zeeman, the demagnetisation and the magnetoelastic terms. The exchange term is ignored due to its small influence on ferromagnetic regions away from the layer interfaces [151, 152] and since the exchange energy affects neighbouring spins, the frequency

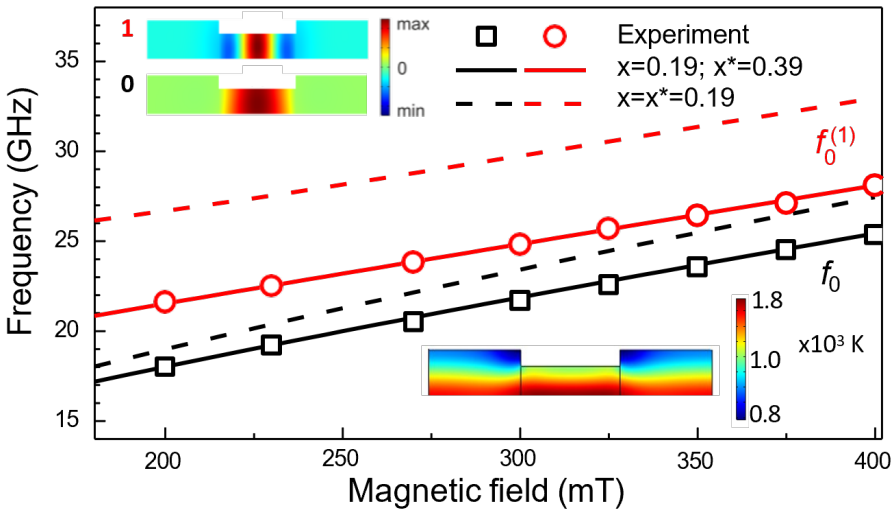


Figure 26: This figure shows the theoretical field dependence of the first two magnon modes, where x is the gallium concentration in the unmilled regions and x* is the gallium concentration in the milled regions. The first mode is black and the second is red. The field dependence of galfenol with a gallium composition of 19% in both the milled and unmilled regions is represented by the dashed lines. The field dependence when the gallium composition of the unmilled regions remains at 19% but the milled regions have a gallium composition of 39% is given by the solid lines. The experimental results are plotted as black squares for the first mode and red circles for the second mode. The upper inset shows the spatial distribution of both the magnon modes. The lower inset shows the temperature distribution of the electrons in the galfenol layer 100 fs after the optical excitation.

range of the exchange magnons is proportional to the inverse of the lattice constant, which results in magnon frequencies of the order 1 THz [153]. The cubic term is ignored due to the confinement of the magnetisation caused by the grating, which results in the magnetisation lying in a local energy minimum, meaning the uniaxial term is dominant.

Since the galfenol is a thin film the only component of the uniaxial anisotropy of interest is the x-component and the form of the demagnetising field is taken to be $H_{int} = \mu_0 M_s/2$, which assumes the film is infinite but is an appropriate simplification considering the width of the peaks of the gratings (48 nm) is much smaller than the length of the gratings (20 μm). Therefore, the resultant energy density takes the form:

$$E = -\mu_0 M_s \boldsymbol{m} \cdot \boldsymbol{H_{ext}} + K_u m_x^2 + \frac{1}{2}\mu_0 M_s m_z + B_1 \varepsilon_{xx} m_x^2. \qquad (70)$$

The parameter values of the saturation field and the uniaxial anisotropy field for high (low) pump fluence were found to be 1.70 T (1.79 T) and 42 mT (49 mT), respectively. These were obtained by fitting the magnetic field dependence of the ground magnon mode. From previous work, the magnetoelastic constant is known to be B_1 = -9 T [140]. Finally, the Gilbert damping coefficient is measured from the full-width half maximum (FWHM) of the magnon mode, which corresponds to $\alpha = 0.0085$.

By assuming that the perturbations of the effective field due to both the quasi-harmonic phonon excitation and the broadband optical excitations are small, the time evolution of H_{eff} can be modelled by

$$\boldsymbol{H_{eff}}(t) = \boldsymbol{H_0} + \boldsymbol{\delta H_{phonon}}(t) + \boldsymbol{\delta H_{photon}}(t) \qquad (71)$$

here, $\boldsymbol{H_0}$ is the static component of the effective field from the demagnetising term, the Zeeman term and the initial uniaxial and magnetoelastic anisotropy terms, $\boldsymbol{\delta H_{phonon}}(t)$ is the perturbation due to the phonon excitation resulting from the changing strain in the magnetoelastic term, and $\boldsymbol{\delta H_{photon}}(t)$ is the perturbation due to the photon excitation which results in a change of the uniaxial anisotropy parameter. $\boldsymbol{H_0}$ is calculated by using equation 31 and equation 70 with K_u(t=0) and ε_{xx}(t=0). $\boldsymbol{\delta H_{phonon}}(t)$ is determined by the time evolution of ε_{xx} for the Rayleigh phonon, which takes the form $\varepsilon_{xx} = -A\sin(\omega_R t)\exp(-\Gamma_R t/2)$, where A is the amplitude of the phonon excitation, ω_R is the frequency of the Rayleigh phonon and Γ_R is the decay rate of the Rayleigh phonon. Γ_R was experimentally measured from the FWHM of the spectral line of the Rayleigh mode with a value of 1.25 GHz. The amplitude was

estimated numerically via fitting to the Rayleigh mode for the two pump fluences of 1.2 mJ/cm^2 and 10 mJ/cm^2, which produced values for A of 5×10^{-6} and 3.5×10^{-5}, respectively. This results in the phonon-induced perturbation of the x component of the effective field being

$$\delta H_{phonon,x}(t) = -2B_1 A sin(\omega_R t) exp(-\frac{\Gamma_R t}{2}) m_{0x} \tag{72}$$

where m_{0x} is the x projection of the static magnetisation.

The optical perturbation is modelled considering two mechanisms of excitations. The first excitation mechanism is ultrafast demagnetisation, which is modelled as an instantaneous decrease of the uniaxial anisotropy. This suggests that the corresponding change in the x component of the optical excitation can be written as

$$\delta H_{photon,x}(t) = 2\delta K_u m_{0x} \Theta(t), \tag{73}$$

here δK_u is the change of the uniaxial anisotropy coefficient and $\Theta(t)$ is the Heaviside function which is 0 at t = 0 and 1 at t > 0. Previous works on galfenol nanolayers [154] suggest that the change in the uniaxial anisotropy coefficient is δK_u = 1 mT.

The second excitation mechanism is via spin transfer torques (STT) induced by optically excited diffusive spin currents. The method of including this spin torque into the LLG equation follows [155], which models the excitation as a time-dependent modulation of the effective field, which is in line with how the other perturbations have been modelled. For the case of ultrashort spin diffusion, the contribution to $\boldsymbol{\delta H_{photon}}(t)$ can be taken to be a rectangular pulse with a fixed direction (which is taken to be the x-axis to match the phonon and demagnetising modulations), which takes the form

$$\delta H_{photon,x}(t) = A_{stt} \tau_{stt} \omega_0. \tag{74}$$

The amplitude of the pulse is A_{stt} = 100 mT, and the duration is τ_{stt} = 0.2 ps [156], and ω_0 is the frequency of the pulse, which corresponds to the magnon eigenfrequency. The condition $\omega_0 \tau_{stt} \ll 1$ suggests that the time scale of the spin current-induced spin transfer torque is much shorter than the time scale of the magnon oscillations is satisfied. The two-photon-induced changes in the uniaxial anisotropy coefficient occur in mixed proportions for all cases other than the extremum values. The mixing of these mechanisms is explored analytically.

To solve the LLG equation analytically, the spherical coordinate system is used with the assumption that there are static angles and

a time-dependent small perturbation to these angles, such that

$$\begin{aligned}\theta(t) &= \theta_0 + \delta\theta(t) \\ \phi(t) &= \phi_0 + \delta\phi(t)[157]\end{aligned} \tag{75}$$

where $\theta(t)$ is the polar angle of the magnetisation vector, which can take values from 0 to 2π, θ_0 is the stationary polar angle with respect to a given external magnetic field and $\delta\theta(t)$ is the time-dependent perturbation to the stationary polar angle. $\phi(t)$ is the azimuthal angle, which can take values from 0 to π, ϕ_0 is the stationary azimuthal angle with respect to a given external magnetic field, and $\delta\phi(t)$ is the perturbation of the azimuthal angle. The radial component is 1 due to the normalising of the magnetisation components. The change to spherical coordinates results in

$$\begin{aligned}\frac{1}{\gamma}\frac{dm_\theta}{dt} &= M_s h_\phi \\ \frac{1}{\gamma}\frac{dm_\phi}{dt} &= M_s h_\theta\end{aligned} \tag{76}$$

where the h_i terms take the form

$$\begin{aligned}h_\theta &= -\frac{1}{M_s}(E_{\phi\theta}\phi + E_{\theta\theta}\theta) \\ h_\phi &= -\frac{1}{M_s}(E_{\phi\phi}\phi + E_{\phi\theta}\theta).\end{aligned} \tag{77}$$

The E_{ij} are the second derivatives of the magnetic free energy density, where the subscripts denote what the derivative is with respect to. Finally, the magnetisation components are given by $m_\phi = M_s \sin\theta_0 \delta\phi$ and $m_\theta = M_s\delta\theta$, which, by substituting equations 76 and 77 into each other and the spherical magnetisation components, result in a one-dimensional harmonic oscillator type equation for the deviation of the in-plane azimuthal angle

$$\frac{d^2\delta\phi(t)}{dt^2} + \Gamma_0\frac{d\delta\phi(t)}{dt} + \omega_0^2\delta\phi(t) = gB_1 sin(\omega_R t)exp(-\frac{\Gamma_R t}{2}). \tag{78}$$

here, Γ_0 is a damping constant which is given by $\Gamma_0 = \gamma\alpha(F_{\theta\theta}+F_{\phi\phi})$. g is the coefficient which couples the driving term to the oscillator, where the driving term in this case is due to the phonons and the oscillator is the magnons. g takes the form $g = \omega_0^2 \sin\,\phi_0/F_{\phi\phi}$. The solutions to equation 78 take the form

$$\delta\phi(t) = \delta\phi_{phonon}(t) + (\delta\phi(0)cos(\omega_0 t) + \delta\dot{\phi}(0)\omega_0^{-1}sin(\omega_0 t))exp(-\frac{\Gamma_0 t}{2}). \tag{79}$$

$\delta\phi_{phonon}(t)$ is the partial solution due to the phonon driving interaction given by

$$\delta\phi_{phonon}(t) = -asin(\omega_R t)exp(-\frac{\Gamma_R t}{2}) - bcos(\omega_r t)exp(-\frac{\Gamma_r t}{2})$$
$$+bcos(\omega_0 t)exp(-\frac{\Gamma_0 t}{2}) + (a\omega_R + b(\Gamma_0 - \Gamma_R)/2)\omega_0^{-1}sin(\omega_0 t)exp(-\frac{\Gamma_0 t}{2}) \tag{80}$$

and

$$a = \frac{g \cdot B_R \cdot \Delta}{\Delta^2 + \omega_R^2(\Gamma_0 - \Gamma_R)^2}, \quad b = \frac{g \cdot B_r \cdot \omega_R(\Gamma_0 - \Gamma_R)}{\Delta^2 + \omega_R^2(\Gamma_0 - \Gamma_R)^2},$$
$$\Delta = \omega_R^2 - \omega_0^2 - \frac{\Gamma_R^2}{4} + \frac{\Gamma_0\Gamma_R}{2}.$$

The initial conditions required to solve the general solution are the initial displacement and the initial velocity, which are the azimuthal perturbation at time zero, $\delta\phi(0)$, and the first time derivative of the azimuthal perturbation at time zero, $\delta\dot{\phi}(0)$. These initial conditions describe the different mechanisms of the broadband optical excitation. The initial displacement is determined by the demagnetisation effect, given by

$$\delta\phi(0) = 2\frac{sin\phi_0}{E_{\phi\phi}}\delta K_u m_{0\phi}\Theta(t) = 2\frac{sin\phi_0}{E_{\phi\phi}}\delta K_u cos\phi_0\Theta(t) = \frac{sin\phi_0}{E_{\phi\phi}}B_{dis}. \tag{81}$$

Due to the step function, this mechanism describes a displacive excitation because the instantaneous change in the uniaxial anisotropy causes an instantaneous change in the magnetisation direction. The spin transfer torque excitation sets the initial velocity

$$\delta\dot{\phi}(0) = -\omega_0^2\frac{sin\phi_0}{E_{\phi\phi}}A_{stt}\tau_{stt} = -\omega_0\frac{sin\phi_0}{E_{\phi\phi}}B_{imp}. \tag{82}$$

Since the spin transfer torque excitation has the form of a rectangular pulse, this describes an impulsive excitation. The interference effects are determined by the ratio between the displacive and impulsive excitation, which determines the initial phase, and the last term in equation 80 determines the phase at the magnon frequency. An important point of note is that since 78 takes the form of a damped and driven harmonic oscillator when the oscillator frequency is passed through the driving frequency, a π phase is imparted on the oscillator system. Proof of this is given in the appendix Chapter A1.

The dependence of the magnon spectra on the pump fluence is measured for five laser fluences (1.2, 2.5, 4.0, 8.0 and 10.0 mJ/cm^2).

The lower laser fluences, 1.2 and 2.5 mJ/cm^2, show no nulling of the magnon amplitude. A dip in the magnon spectra first occurs at 4.0 mJ/cm^2, and the nulling continues to deepen up to 10 mJ/cm^2. The change in fluence is modelled by varying the amplitudes of the different magnon excitation mechanisms. This is achieved by changing B_R, B_{imp} and B_{dis}. The relationship between each of the excitation mechanisms defines the phase, whereas the absolute values determine the total amplitude of the measured change in Kerr angle, which decreases with increasing fluence due to the rising background temperatures causing a decrease in the magnetoelastic constant and the saturation magnetisation [156]. This means that the absolute value of B_{dis} and B_R decrease, which appears as the nulling detuned from the phonon driving excitation. The value of B_{dis} is arbitrarily fixed at 1 mT; this value is chosen such that the ratios between the other excitations can be based upon it, since the absolute values are not important. The values taken for the other excitation mechanism amplitudes are shown in Figure 27, which shows that by increasing B_R and B_{imp}, the interference-based effects can be modelled to match the experimental results.

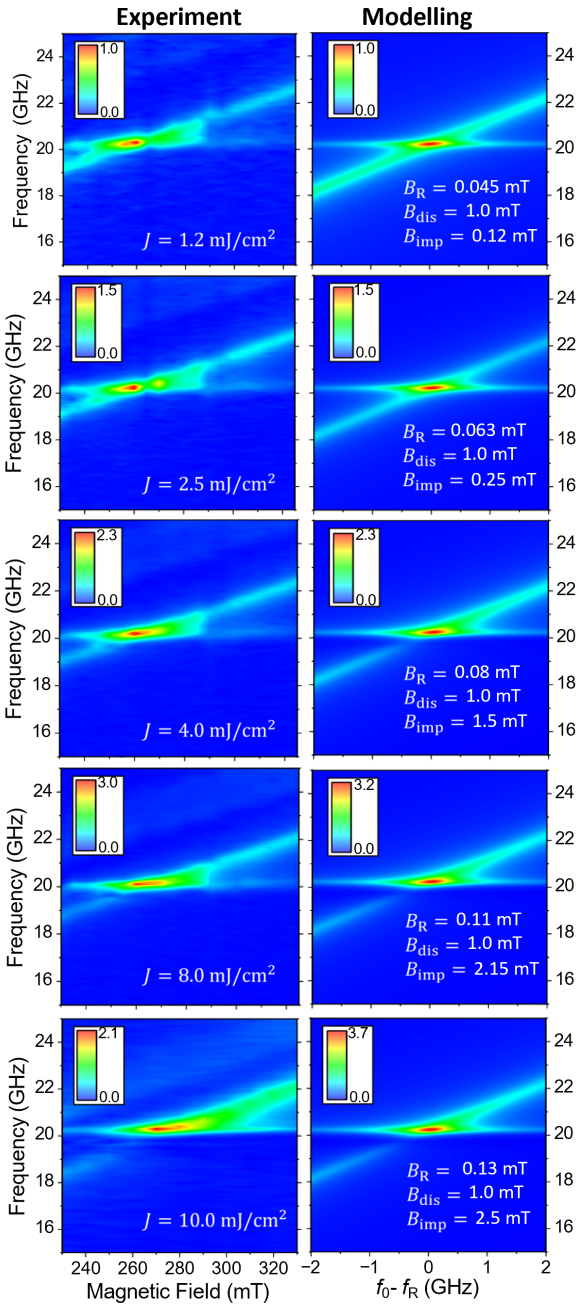


Figure 27: Left panels show experimental magnon spectra produced through the collection of FFT measurements for a variety of pump fluences. Right panels show the results of the LLG equation for different values of B_{dis}, B_{imp} and B_R, where the values of B_{dis} and B_{imp} determine the dominant optical excitation mechanism. The value of B_{imp} given is at $\omega_0 = \omega_R$.

2.5 Conclusion

This chapter explored laser excitation of a nanograting milled into the surface of the ferromagnetic material galfenol. This results in the excitation of both magnons and Rayleigh mode phonons, which are confined within the nanograting.

Experimentally, it was observed that at high pump laser fluences (10mJ/cm^2), the magnon spectral amplitude is nulled at a detuning below the phonon frequency of 0.4 GHz, along with an increase in the spectral amplitude above the phonon resonance interaction. This is the form of a Fano-like resonance, which is an interference-based resonance that originates from the interaction between a quasi-harmonic excitation and a broadband excitation. In this experiment, the quasi-harmonic excitation is due to the Rayleigh mode phonon driving of the magnons. The broadband excitation is due to optical excitation of the magnons. This optical excitation of the magnons occurs via two separate mechanisms: ultrafast demagnetisation and STT induced by a spin current. The initial phase of the magnon precession is determined by the ratio of these two broadband excitation methods, which is controlled by the laser fluence. This therefore allows the Fano-like resonance interaction to be controlled.

The origin of the STT mechanism is hypothesised to be due to gallium implantation in the milled regions caused by the ion milling being accomplished using Ga^+ ions. The increase of the gallium concentration in the milled regions lowers the Curie Temperature of these regions; this results in the laser pumping at high fluences raising the temperature of these regions beyond the Curie temperature, which produces stripes of adjacent magnetically active and magnetically dead regions that allow spins to be pumped through, inducing an STT.

This hypothesis is further confirmed through modelling of the nanograting, where the milled regions are taken to have a gallium percentage of 39% (increased from 19%). With the two mechanisms of the magnon excitation being determined, the LLG equation is solved, providing further theoretical evidence of the origins of the Fano-like resonance interaction.

This work could be further explored by experimentally confirming the concentration of gallium in the milled regions via external uniform heating of the sample. Furthermore, the gallium concentration can then be adjusted, changing the dependence of the Fano-like resonance interaction on the pump fluence. The period of the nanograting can also be adjusted, which would move the phonon

resonance and, by extension, would allow the magnon nulling frequency to be controlled.

3 Enhanced Phonon-Photon Interaction in Acoustic Nanocavities

3.1 Introduction

The work presented in this chapter is published in ACS Photonics [158] as Enhanced photon-phonon interaction in WSe_2 acoustic nanocavities. Within this work, the sample preparation was undertaken by G. Magnabosco, N. Vogel and C. Ruppert. The experimental results were gathered by A. D. Carr with help from A. K. Samusev. The data analysis was completed by A. D. Carr, A. V. Akimov, A. V. Scherbakov and A. K. Samusev. Finally, the theoretical understanding was provided by T. L. Linnik and A. V. Akimov.

The work described in this chapter examines the use of van der Waals (vdW) nanolayers of WSe_2 as acoustic nanocavities (ANCs). VdW materials are composed of many atomic layers where the interlayer force is the van der Waals interaction. The vdW material, WSe_2, was used due to the internal strain depending on the number of layers of the material [159, 160] as well as the direct exciton resonance being close to the probe laser energy [161]. WSe_2 is a transition metal dichalcogenide (TMD) with a crystal structure illustrated in Figure 28, which is a family of materials that take the form ME_2 where M is a transition metal and E is either sulfur, selenium or tellurium. This family of materials possesses a variety of properties, but all are semiconductors. The layers are deposited onto an opal substrate layer, which provides mechanical support without altering the acoustic properties of the nanolayers. The nanolayers are excited and probed by lasers using a pump-probe measurement technique. This allows for longitudinal phonons to be excited within the nanolayers. This process is repeated for many layers of varying thickness, which produce different fundamental frequencies depending on the thickness. This allows the amplitude as a function of the fundamental frequency to be explored for higher-order harmonics and fundamental modes.

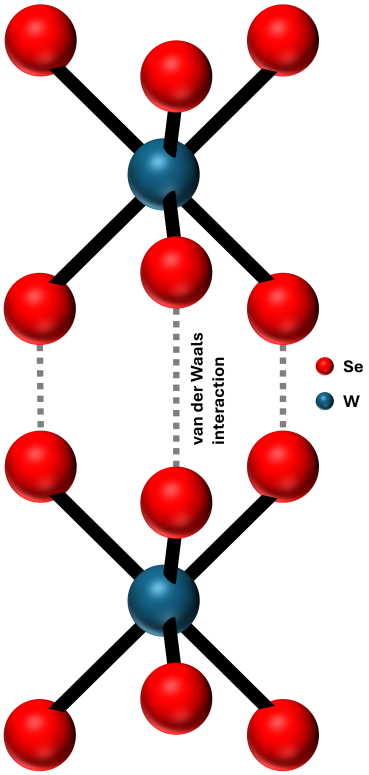


Figure 28: A cartoon that illustrates the hexagonal crystal structure of WSe_2 and the van der Waals interaction that occurs between adjacent layers. The red atoms are selenium, and the blue atoms are tungsten.

3.2 Current Works in Phonon Nanocavities

The study of acoustic cavities began half a century ago, with the examination of bulk phonon modes confined in crystals, such as ruby [162]. These produced low-frequency phonons (of the order MHz). More recently, due to advancements in material science and fabrication techniques, devices can be made with nanostructures (gratings [163], as described in the the previous chapter, waveguides [164] and pillars [165]), superlattices [166, 167] and membranes of semiconductor material (examples include Si [168, 169] and GaAs [170]). This allows for GHz to sub-THz frequency phonons to be achieved, which have found use in various applications, including filters [171], modulators [172], sensors [173], optical cooling [174], and the performance of quantum operations [175, 176, 177]. Current research looks to extend this range further into the THz range and the single-phonon limit [178] to expand applications to more quantum technologies and communications, which require high speeds and sensitivities.

The THz range is being reached by optimising the devices mentioned previously through the choice of material and device design. This work utilises vdW nanolayers, which are a classification of materials characterised by the interaction between crystal layers, with the primary interaction being van der Waals forces. vdW nanolayers are chosen due to its ease of fabrication and the promising results showing sub-THz and THz acoustic properties in samples of graphene [179] and various TMDs [180, 163].

Due to vdW materials being arranged in atomic layers, there are higher-order phonon modes that can be excited as each layer is only weakly bound to the adjacent layers, allowing these layers to move more independently than a tightly bound crystal lattice. These modes are separated into transverse and longitudinal waves; the transverse waves are referred to as shear modes, with each layer moving in the plane of the sample. The modes studied in this experiment were the longitudinal modes, also known as breathing modes, where the spacing between each layer varies. The relatively weak vdW interaction enables the production of thin films through the exfoliation process. Another key reason for using vdW materials is that the Q-factor of devices fabricated using these materials is greater than 10^3, resulting in f$\times$Q reaching record-breaking values of 10^{14} Hz [181, 182]. Previously, studies of these materials have focused on maximising the resonant frequency of the phonons or minimising the decay rate [183, 184, 185]. Instead, this study looks to maximise the amplitude of the detected signal, as this quality is essential for the use of these materials in practical devices. TMDs

are another family of materials composed of a transition metal atom and two chalcogen atoms. Some TMDs are semiconductors which can transition to superconductors by twisting adjacent layers [186]. They also possess favourable electrical and mechanical properties, along with a direct bandgap and the ability to be scaled down to atomic layers, making this family of materials an area of current study [187]. WSe_2 is used in this experiment because this material has well-documented optical and elastic properties, including the refractive index and its wavelength dependence [161, 188], the deformation potential [189], and the speed of sound [190].

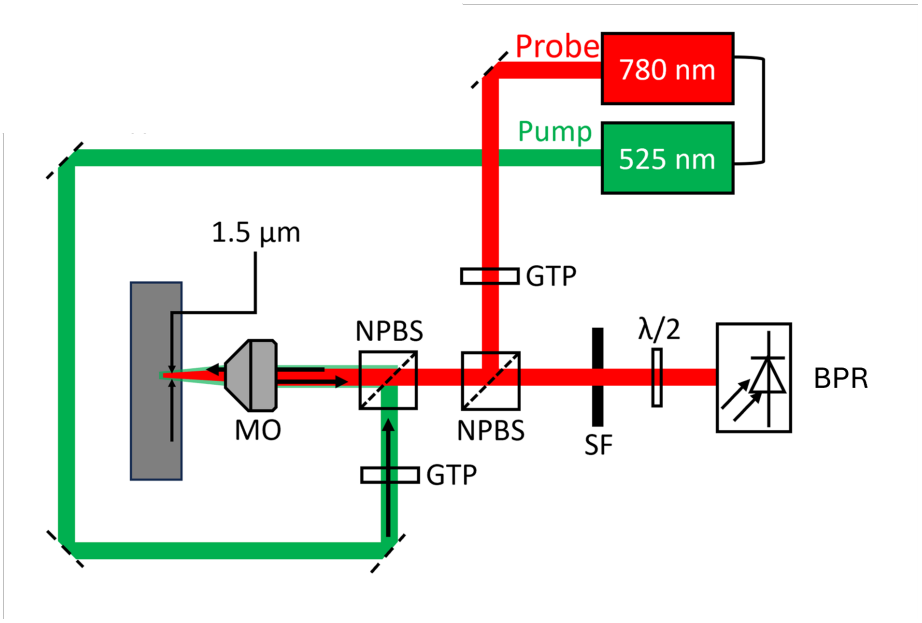


Figure 29: A schematic showing the ASOPS setup used for this experiment. The probe wavelength is 780 nm, and the pump is 525 nm. The spot size of both the pump and the probe was 1.5 μm. A balanced photoresistor is used to detect the phonon intensity. MO is a microscope objective, NPBS is a non-polarising beam splitter, SF is a spatial filter, $\lambda/2$ is a waveplate, and GTP is a Glan-Taylor prism.

3.3 Methods

3.3.1 Setup

This experiment employed a pump-probe laser setup, which utilises the asynchronous optical sampling (ASOPS) scheme. The experimental setup is illustrated in Figure 29. This setup employs frontside excitation, in which both the pump and probe lasers are incident on the front face of the sample. In this experiment, two TOPTICA Yb-doped fibre ring harmonic oscillator lasers are used as the pump and probe. The pump and probe have central wavelengths of 1050 nm and 780 nm, respectively. To utilise the ASOPS scheme, the lasers need to have a frequency offset between their repetition rates; this is achieved by a synchronisation unit from Laser Quantum. The offset frequency is set to 800 Hz. Within these works, the second harmonic of the pump was utilised; therefore, the pump wavelength is 525 nm. The second harmonic of the laser is achieved by using a beta-barium borate (BBO) crystal. This crystal enables the process of second-harmonic generation (SHG). This is a nonlinear process

which converts two photons of equal frequency to one photon of half the wavelength.

In front of the sample is a microscope objective, which focuses the laser light into a spot on the sample. The microscope objective used is the Mitutoyo NIR 20x lens. Before the microscope objective, the laser power is measured to be 0.3 mW. The fluence of the laser measured on the sample is then calculated to be 0.15 mJ/cm^2. The microscope objective is attached to a piezotranslator (piezosystem Jena, NV40 3CLE, Tritor 101), which is used for fine movement of the laser spot. This translator features three-dimensional travel, with 100 µm of movement in each axis. The light reflected off the sample undergoes a change in intensity due to absorption, re-emission, and reflection of the laser light.

This light is detected by a balanced photoreceiver (Newport balanced photoreceiver, model 2107) (BPR). The BPR is set such that the low-pass filter is 100 Hz, the high-pass filter is 10 MHz, and the gain is set to 100. Furthermore, to measure the intensity change, one of the pair of sensors on the BPR is covered. Thus, only the change of intensity of a single polarisation is measured. The low-pass filter is also set to the DC setting to measure the DC reflectivity while the pump laser is blocked. An oscilloscope (Techtronix DPO 5104) is connected to the BPR in order to read the electrical signal from the BPR. Also connected to the oscilloscope is an electrical triggering system, which allows the resolution to be increased from 12 ns, corresponding to the repetition rate of the lasers, to ≈ 1 ps.

Additional optical elements are used, including half-waveplates, polarised beam splitter cubes, non-polarised beam splitter cubes, and Glan-Taylor prisms. There is also a microscope and lamp used to observe the placement of the laser beams, ensuring a good laser shape, overlap, and placement.

3.3.2 Materials

The substrate of this sample is composed of silica particles that self-assemble to form a colloidal crystal thin film, which is referred to as an opal. These are chosen because they provide both mechanical and thermal stability to the WSe_2 flakes while acting as a suspended layer, therefore allowing the WSe_2 to flex in the longitudinal direction, which does not occur with typical substrates. A scanning electron microscope (SEM) image is shown in Figure 30a. The opals are synthesised by a modified Stöber process. The Stöber process is a complex process that primarily uses three chemicals: TEOS, water, and ammonia [191]. The concentrations of each of these chemicals

affect the size of the resultant opals. There are, however, other factors that affect growth, including temperature, additional solvents, salts, and the dielectric properties of the solvent. If extra solvents are used, the longer the alkyl chain, the larger the opals become, but the more spherically symmetric they are. If the extra solvent is a dielectric material, the larger the dielectric constant of the solvent, the higher the stability of the colloid formed. Salts are used to reduce the formation of secondary particles, resulting in monodisperse opals. Finally, temperature is used to produce smaller particles with a narrow size distribution [191]. These opals were prepared using vertical deposition, whereby a glass substrate is immersed in a 0.1 wt% particle suspension. The solvents are then dissolved over three days at 65°C. This process produced opals with a diameter of 265 nm, which form a hexagonal close-packed structure.

On top of the opal substrate are thin films of WSe_2, which range in thickness from 8 - 130 nm. These films were produced by the external company, HQ Graphene, where the films were exfoliated from bulk samples of WSe_2. These thin films are known as vdW nanolayers. The process of transferring these vdW nanolayers to the opal substrate uses a transfer stamp. This process usually uses polydimethylsiloxane (PDMS) on top of a glass slide, which is affixed using crystal scotch tape. Polycaprolacetone (PCL) is then spin-coated and annealed onto the stamp. The PCL is heated to 57°C when placed on top of the WSe_2, then the PCL is cooled to allow the WSe_2 to be fixed to the stamp [192]. The PCL stamp is then placed onto the opal substrate, and the temperature is raised to >65°C to melt the PCL. This leaves the WSe_2 flakes on the opals along with some PCL residue. A solvent bath of tetrahydrofuran is used to remove the residue. An atomic force microscope (AFM) image of a flake exfoliated on top of the opal substrate is shown in Figure 30(b). The flakes were distributed across the surface of the opal. Figure 31 shows a darkfield microscope image to illustrate the spread of the flakes.

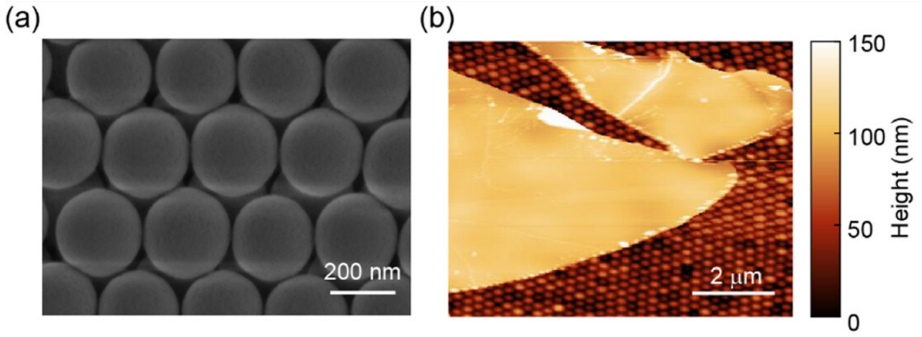


Figure 30: (a) a scanning electron microscope (SEM) image of the opal substrate. (b) An atomic force microscope image of 2 flakes of WSe2 on top of the opal substrate [158].

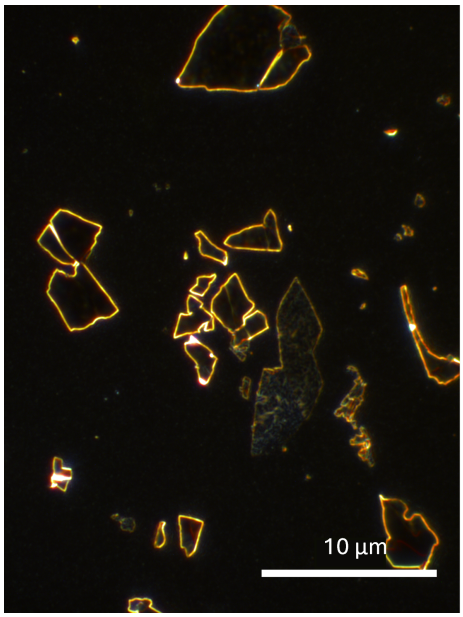


Figure 31: Dark-field microscope image of the WSe2 flakes, taken at a magnification of 100x. This illustrates a rough representation of the distribution of flakes across the substrate's surface.

3.3.3 Techniques

To collect the data, several averages were taken to improve the signal-to-noise ratio. Typically, for these measurements, the number of time traces taken was 50000. In this case, as the change in intensity is being measured, the averaged result appears as shown in Figure 32. This data shows a sharp peak, which is due to the

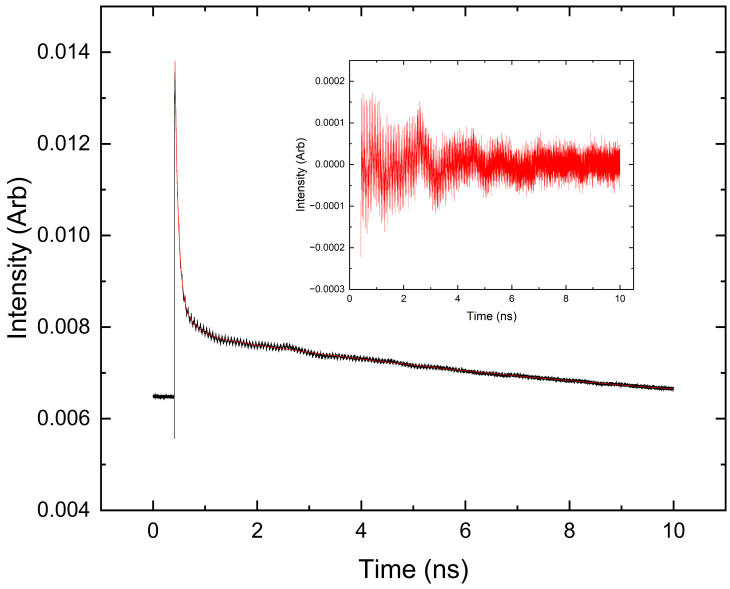


Figure 32: A change in intensity signal recorded by the BPR. This is an averaged signal with 50000 averages taken. The inset shows the phonon oscillations, which are determined by fitting an exponential decay function to the data from the trough to the end and plotting the residual data.

electronic background excitation. This excitation is not of interest and is filtered out by fitting an exponential decay curve to the start of the decay and the end of the data. This produces data in the form of Figure 32 inset. This figure illustrates the oscillations caused by phonons. To extract the frequency components, a fast Fourier transform (FFT) algorithm is performed; this takes the data from the time domain to the frequency domain. A typical frequency trace is shown in Figure 33. There is always a fundamental frequency, which is the fundamental breathing mode phonon. The thickness of the flakes, d, was estimated using atomic force microscopy (AFM) by Claudia Ruppert to calculate an estimated

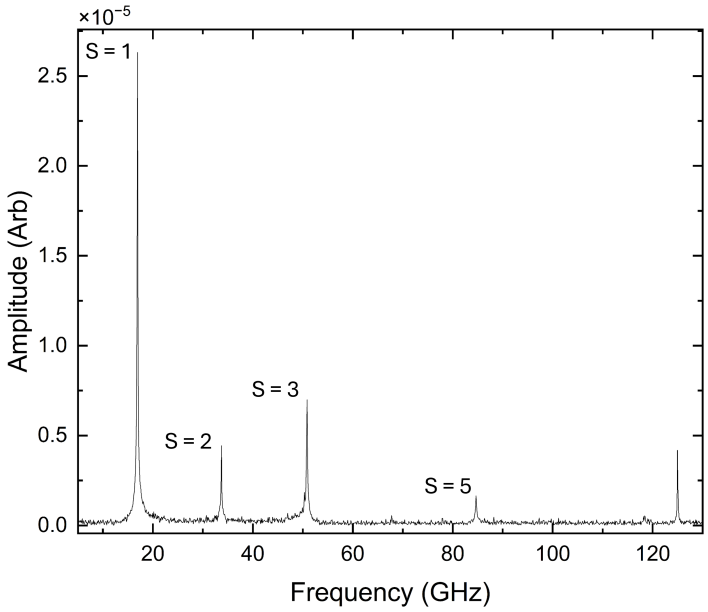


Figure 33: An example of a typical FFT. This figure displays a fundamental frequency of $f_1 = 16.9$ GHz. The s = 1, 2, 3, 5 are present in this data, where s is the order of the observed mode. A frequency component is observed at f = 125 GHz, which is a parasitic frequency resulting from the ASOPS process.

speed of sound within WSe_2. Five flakes where the fundamental frequency was measured were taken and had the thickness measured independently via AFM to determine the speed of sound in the flakes by using $f_s = sv/2d$, where v is the speed of sound in WSe_2, it is calculated to be 2840±20 ms^{-1} (this is 12% greater than previous works [190]), and s is the order of the harmonic, with $s = 1$ being the fundamental frequency. This then also allows the thickness of flakes not measured with AFM to be calculated. There are also higher harmonics of this fundamental frequency; each harmonic is an integer multiple of this fundamental frequency. Finally, there is an extra frequency component at 125 GHz. This extra frequency is an artefact caused by the lasers interfering; this effect is a type of parasitic oscillation.

3.4 Results

For each WSe_2 flake, the reflectivity was measured without the pump being applied to the sample. This was achieved by setting the BPR to DC mode and recording the voltage. This parameter is R_0. The change in reflectivity, ΔR, was then found from the Fourier transform of the time trace. The amplitude of each harmonic was then produced, which can be used to find the normalised change in reflectivity, $\Delta R/R_0$. The reflectivity, R_0, can be fitted for multilayer dielectrics as given by [193]:

$$R_0 = \frac{r_{12}^2 + r_{23}^2 + r_{12}\ r_{23}\ \cos(\frac{4\pi c}{f}\ n_2\ d\cos(\theta_2))}{1 + r_{12}^2 r_{23}^2 + 2r_{12}\ r_{23}\ \cos(\frac{4\pi c}{f}\ n_2\ d\ \cos(\theta_2))} \tag{83}$$

where r_{ij} are the reflection coefficients, which depend on the refractive indices of adjacent layers. $\lambda = c/f$ is the wavelength of the probe light. n_2 is the refractive index of the WSe_2, θ_2 is the incident angle of light into the WSe_2 layer, and d is the thickness of the WSe_2 layer. By taking the layers to be air (n = 1), WSe_2 and opal spheres (n = 1.5) and assuming that the incident angle between all the layers is 0°, this produces Figure 34. The refractive index taken for WSe_2 in the fitting is 5.26. This value is taken from databases and papers [188, 161], which cite the complex refractive index for the probe wavelength of 780 nm as 5.26+0.54i.

As stated in Chapter 3.3.3, the FFT of each of the time traces of the WSe_2 flakes is taken. This allows each of the frequency components to be separated, enabling the identification of the fundamental phonon frequency, along with its higher harmonics. Once the frequency components have been found, frequency filters can be applied to the time trace, and individual waveforms can be extracted;

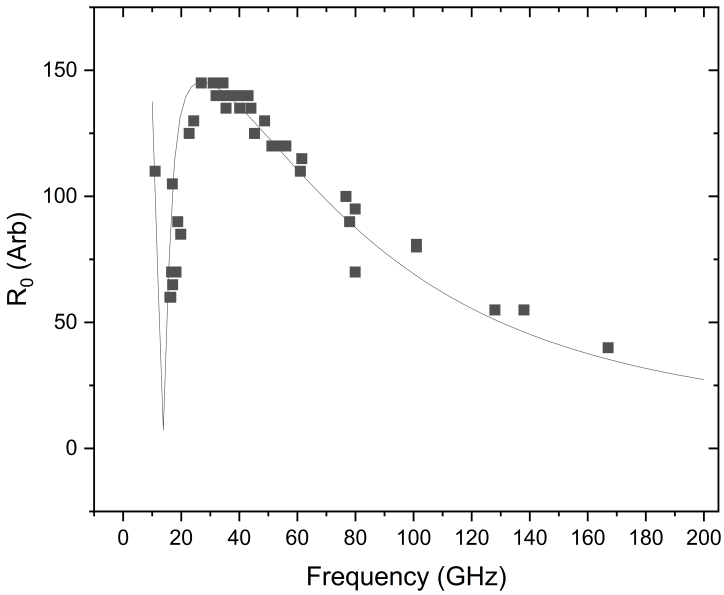


Figure 34: Reflectivity measurements of all the WSe_2 flakes against the fundamental phonon frequency of each flake. Equation 83 is used to produce the fit, which confirms that the values of n_2 are appropriate. The uncertainty in these measurements is low due to low error in the responsivity of the photodiode and the high accuracy of the power meter used; therefore, the experimental uncertainty of the reflectivity is smaller than the point size (of the order 0.1 (Arb).

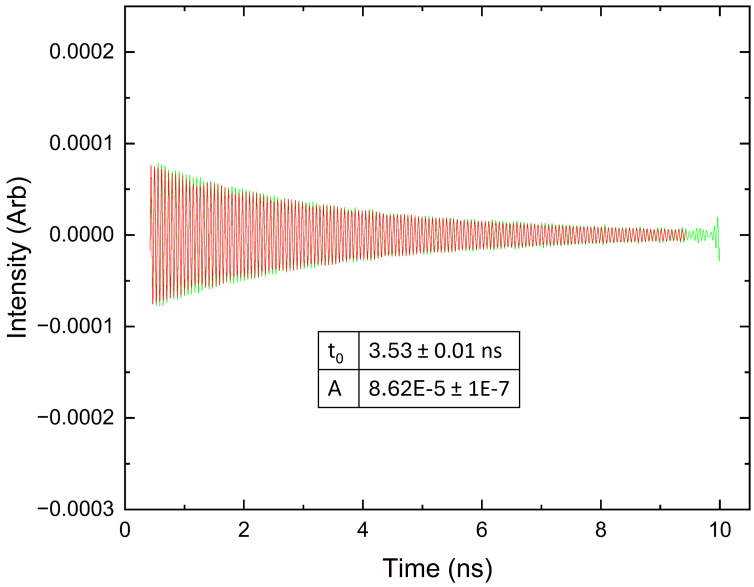


Figure 35: The phonon signal from the inset in Figure 32 was taken, and an FFT band filter was applied between 10 - 20 GHz to extract only the fundamental frequency; this is the green curve. Using a damped sine function, the oscillations are fitted to the filtered signal to extract the decay rate and amplitude as shown by t0 and A, respectively.

this process is done to determine the amplitude and decay rate without any influence from the windowing function used for the FFT. These waveforms take the form $A_s\exp(-t/\tau_s)\sin(\omega_s t)$, where A_s is the amplitude of the waveform for the s^{th} harmonic, τ_s is the decay constant for the s^{th} harmonic and $\omega_s = 2\pi f_s$ is the angular frequency of the s^{th} harmonic. With the frequency of the waveforms being known and estimates for the amplitudes (being found from the amplitude of the FFT) and the decay constants (being found from the half width half maximum of the peaks in the FFT), a fitting can be produced to acquire more accurate values for the amplitude and decay constants which are independent of the windowing function used in the FFT, an example of which is shown in Figure 35, Figure 36a shows that there is a roughly inverse relationship between the fundamental frequency of the phonons and the decay rate, meaning high-frequency phonons decay more rapidly, which is expected due to the higher energy requirement of higher frequency phonons.
The amplitudes of higher order harmonics can be plotted as a func-

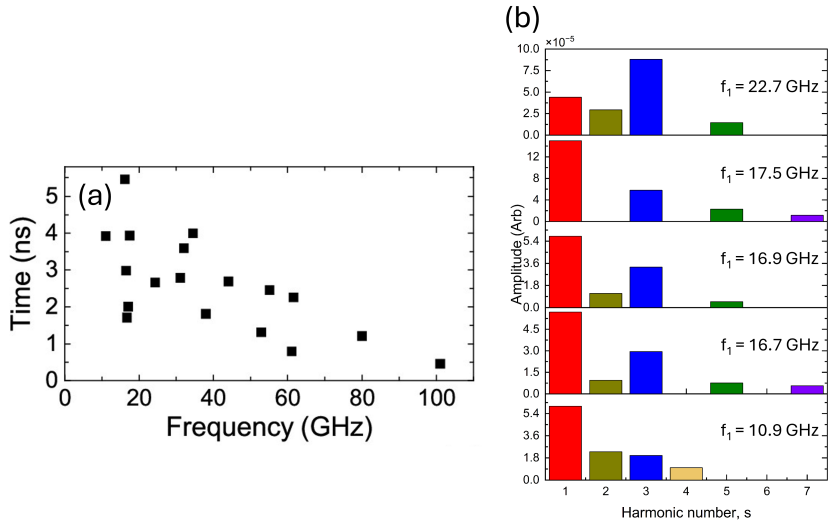


Figure 36: (a) The decay rates of the fundamental phonon modes (s=1) show a negative proportional relationship between the decay rate and the fundamental phonon frequency. As shown by Figure 35, the errors are on the order of 0.01 ns. (b) The amplitude of different harmonics for a selection of 5 different WSe_2 flakes is shown with the fundamental frequency labelled. For 17.5 GHz, the even harmonics are completely suppressed, and for 10.9 GHz, the 4th harmonic is still present, differentiating it from other flakes. The error in the amplitudes is also shown in Figure 35 to be on the order 1×10^{-7}

tion of the fundamental frequency (Figure 36(b)). In some cases, certain harmonics are suppressed. For all cases involving harmonics with s$\geq$5, the amplitudes are negligible due to the greater energy loss of higher frequency waves through damping, in agreement with Figure 36(a). For this reason, Figure 37 only shows the amplitudes of the first three harmonics (s = 1, 2, 3) corresponding to Figures (a), (b) and (c) against the fundamental frequencies. Figure 37 also shows a fitting process, which will be further explained in Chapter 3.5. The maximum amplitude of the fundamental frequency occurs at $f_1 \approx 18$ GHz, corresponding to a flake thickness of 79 nm, which is close to the Bragg thickness where $d_B = \lambda/2\Re\{n\} = 74$ nm, where $\Re\{n\}$ is the real part of the refractive index of WSe_2 when the probe is considered. This peak in the phonon amplitude and its proximity to the Bragg thickness suggest that there is a photoelastic resonance-based effect within the TMD flakes. Also, for the fundamental frequency corresponding to the maximum amplitude for s = 1, there is a minimum in the amplitude for s = 2, and for s = 3, the maximum is shifted to $f_1 \approx 20$ GHz.

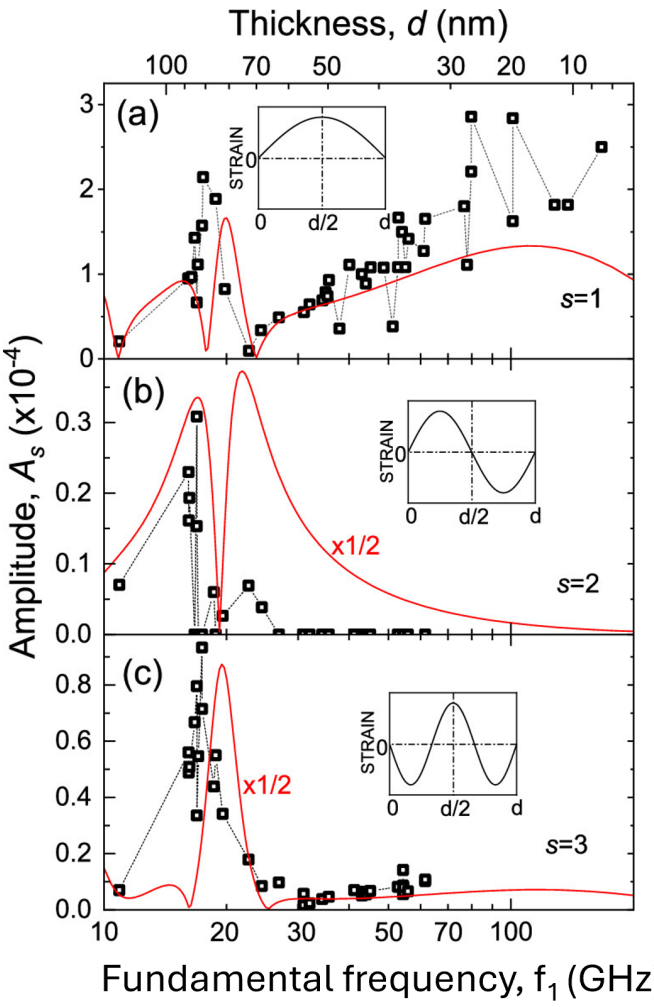


Figure 37: The amplitudes of harmonics compared to the fundamental frequency of the harmonics. (a) shows the fundamental frequency amplitudes. (b) shows the amplitudes of the second-order harmonics as a function of their fundamental frequency. (c) shows the amplitudes of the third-order harmonics as a function of their fundamental frequency. Each figure shows a fitting line (red) whose equation is derived in Chapter 3.5. The insets show the spatial distribution of the phonon modes. The uncertainties in the amplitudes are of the order 1×10^{-7} so are not shown.

3.5 Simulation and Modelling of the Amplitude of Longitudinal Phonon Modes in WSe_2

The theoretical results in this section were produced by T. L. Linnik and A. V. Akimov. To generate the fits used in Figure 37, the strain amplitudes need to be calculated. Since the phonons are coherent, having been created via laser pulses, and were exclusively longitudinal phonons, which is justified by comparing the measured frequencies to theory via the frequency-wavelength relation, which shows the transverse wave would have a frequency in the MHz range due to the vastly different length scales in the transverse and longitudinal directions. The one-dimensional elastic equation can be used.

$$\begin{aligned} \rho\frac{\partial^2 u}{\partial t^2} &= \frac{\partial \sigma_{zz}(t,z)}{\partial z} \\ \sigma_{zz}(t,z) &= \rho v^2 \varepsilon_{zz}(t,z) + G(t,z). \end{aligned} \tag{84}$$

Where ρ is the mass density of the WSe_2 and takes the value 9.32 gcm^{-3}, u is the displacement vector of the atoms within the flake, $\sigma_{zz}(t,z)$ is the zz component of the stress tensor (which implies that it is the z-component of the stress acting in the z-plane). v is the speed of sound in WSe_2, $\varepsilon_{zz}(t,z)$ is the zz component of the strain; the zz component has the same meaning as the stress. Finally, G(t,z) is the stress generated via the ultrashort optical pulse delivered via the pump laser, which is applied at t = 0. To solve equation 84, we can impose Dirichlet boundary conditions such that $\sigma_{zz}(t,z) = 0$ at $z = 0$ and $z = d$. The optically generated stress takes the form

$$G(t,z) = DN_0 e^{-\alpha z}\Theta(t). \tag{85}$$

Where D is a fitting parameter with units of energy, which depends on the mechanism of stress generation. In this experiment, the mechanisms involved are thermoelastic effects and effects through the deformation potential. N_0 is the density of excited electron-hole pairs at the surface of the WSe_2, with $N_0 = 7.3\times10^{25}$ m^{-3}[194] for a pump fluence of 0.15 $mJcm^{-2}$. α is the inverse of the penetration depth, which for the pump laser wavelength $\lambda_{pump} = 525$ nm, the refractive index of WSe_2 was found to be $n_{pump} = 4.6+1.4i$, using the same databases used previously. Additionally, assuming there is no ultrafast carrier diffusion and recombination, $\alpha = 3.3\times10^7$ m^{-1} [195]. Θ is a step function such that $t < 0$ $\Theta = 0$ at $t \geq 0$, $\Theta = 1$. For this one-dimensional case, the strain is given by $\varepsilon_{zz}(t,z) = \frac{\partial u}{\partial z}$. By solving the elastic equation (equation 84) for the atomic displacement vector and substituting this back into the strain equation, it

can be shown that

$$\varepsilon_{zz}(t,s,z) = \frac{DN_0}{\rho v^2}\frac{1}{s\pi}[1-(-1)^s e^{-\alpha d}]\frac{q_s}{\alpha^2+q_s^2} sin(q_s z)e^{i\omega_s t}. \quad (86)$$

Where s refers to the order of the harmonic, and q_s is the wavevector of the s^{th} harmonic. This equation defines the spatial distribution of the phonon modes.

To calculate the normalised change in reflectivity, an earlier theoretical approach was used [196], which results in

$$\frac{\Delta R(t)}{R_0} = 2\Re\{C[(n+p)\Delta d(t) + p\Psi_s(t)]\}. \quad (87)$$

Where $p = dn_{probe}/d\varepsilon_{zz}$ is the reduced photoelastic constant, $\Delta d(t)$ = $u_d(t)$ - $u_0(t)$ is the change in layer thickness due to the generated stress (u_d is the displacement of the top of the flake and u_0 is the bottom), C is a complex variable and defined by equation 88, $\Psi_s(t)$ is a function which dependents on the change in strain over time and the harmonic number of the generated strain. This determines the strength of the photoelastic effect, $\Psi_s(t)$, which is defined further in equation 89.

$$C = 2i\frac{r_{23}(1-r_{12}^2)k_1 e^{2ik_2 d}}{(r_{12}+r_{23}e^{2ik_2 d})(1+r_{12}r_{23}e^{2ik_2 d})} \quad (88)$$

where k_j (j = 1, 2, 3) are the wavevectors of the probe in the air, WSe_2 flakes and opal, respectively, r_{ij} are calculated by (k_i-k_j)/(k_i+k_j).

$$\Psi_s(t) = \frac{1}{2}\int_0^d \varepsilon_{zz}(t,s,z)[r_{23}e^{2ik_2(d-z)} + r_{23}^{-1}e^{-2ik_2(d-z)}]dz \quad (89)$$

where this describes interactions between phonons and photons in the WS_2 layers.

Since the probe wavelength is close to the direct exciton resonance of WSe_2, which is 1.62 eV [188], there is a strong dispersion of the photon regime. With this regime of strong dispersion, the reduced photoelastic constant changes to $p = \Xi\, dn_{probe}/d(\hbar\omega)$. Where $\Xi = dE_{exciton}/d\varepsilon_{zz}$ is the out-of-plane deformation potential, $E_{exciton}$ is the direct exciton energy, and finally, $\hbar\omega$ is a quantum of energy of the probe laser.

Ξ is not known directly; however, other works have been done [189] which show that under hydrostatic pressure, P, $dE_{exciton}/dP$ = 3.4 meVkbar^{-1}. Then, assuming the effects of the out-of-plane stress dominate, Ξ = -$v^2\rho$ $dE_{exciton}/dP \approx$ -3 eV. This assumption

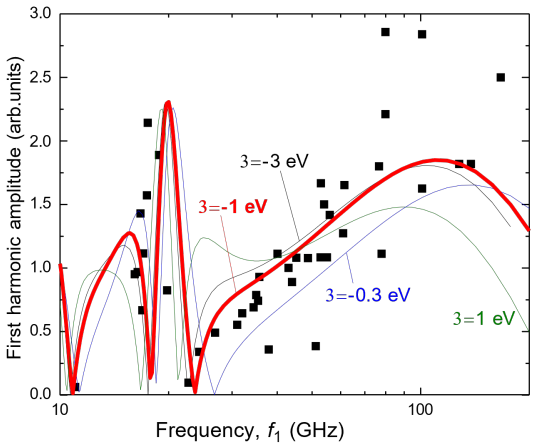


Figure 38: Comparison of different deformation potential values around a known value of -3 eV (black). Other values chosen are -1, -0.3 and 1 eV, where -1 eV shows the closest fit to the data.

allows for an initial estimate of the deformation potential. Therefore, a selection of deformation potentials were chosen around -3 eV and compared in Figure 38.
dn/d($\hbar\omega$) can be determined from the dispersion of multilayer WSe_2, which is computed in other works [188]. Figure 39a,b shows the dependence of n and p on the photon energy within the vicinity of the direct exciton resonance. When the real part of the reduced photoelastic constant is greater than the real part of the refractive index, the photoelastic effect is the dominant effect contributing to the normalised change in reflectivity. The value of the reduced photoelastic constant is greatly increased when the photon frequency is in the vicinity of the exciton resonance, as shown in Figure 39b. This is due to the rate of change of the refractive index being larger since the probe photon energy is also generating excitons. For the case of the probe laser, which is labelled in Figure 39c, the photon energy is within this peak in the reduced photoelastic constant caused by the exciton resonance; therefore, for the probe laser wavelength, the real part of p is increased, which in turn causes the photon-phonon enhancement, since the photons are coupled to the excitons and the excitons are coupled to the strain in the sample this allows for the phonons to be driven via the pump laser but also via this exciton pathway.

Figure 39(c) shows a contour plot of the amplitude of the first harmonic's dependence on the probe photon energy. There are two regions separated by the frequency $f_B = 25$ GHz. This frequency is chosen because it is greater than the resonant effects that occur

in Figure 37(a), which are due to the Bragg condition. In the region $f_1 < f_B$, interference between the probe's light reflected from the ANC surfaces gives rise to photoelastic resonances (as previously discussed). In the region where $f_1 > f_B$, which is well above the Bragg condition, the peaks in amplitude are due to the generation of excitons. Since f_1 is a proxy for layer thickness, it can be seen that a critical layer thickness is reached at $f_1 \approx 0.5$ GHz, which corresponds to a layer thickness of 3 nm. This suggests there are two layers of WSe_2 [160]. The interaction between the strain in the material [197] and the layer thickness [160] lowers the band gap energy such that, without changing the pump fluence, the number of excitons excited is increased. This region has a large linewidth of 0.13 eV; this broadening has been shown to be due to phonon-exciton scattering events [198]. There is a region of amplitude nulling at a photon energy of 1.59 eV, due to the sum of the refractive index and the photoelastic constant producing a minimum in reflectivity. This is due to the asymmetry of the refractive index and the photoelastic constant, which leads to interference between the photons emitted by the excitons and the reflected probe photons. The maximum in the reflectivity is found in this region, which results in the sensitivity of the detection of phonons being optimised in this region. Therefore, the amplification of the higher-order mode of the fundamental frequency 22.7 GHz, shown in Figure 36, is due to the higher-order magnon being in this region of greatly increased sensitivity.

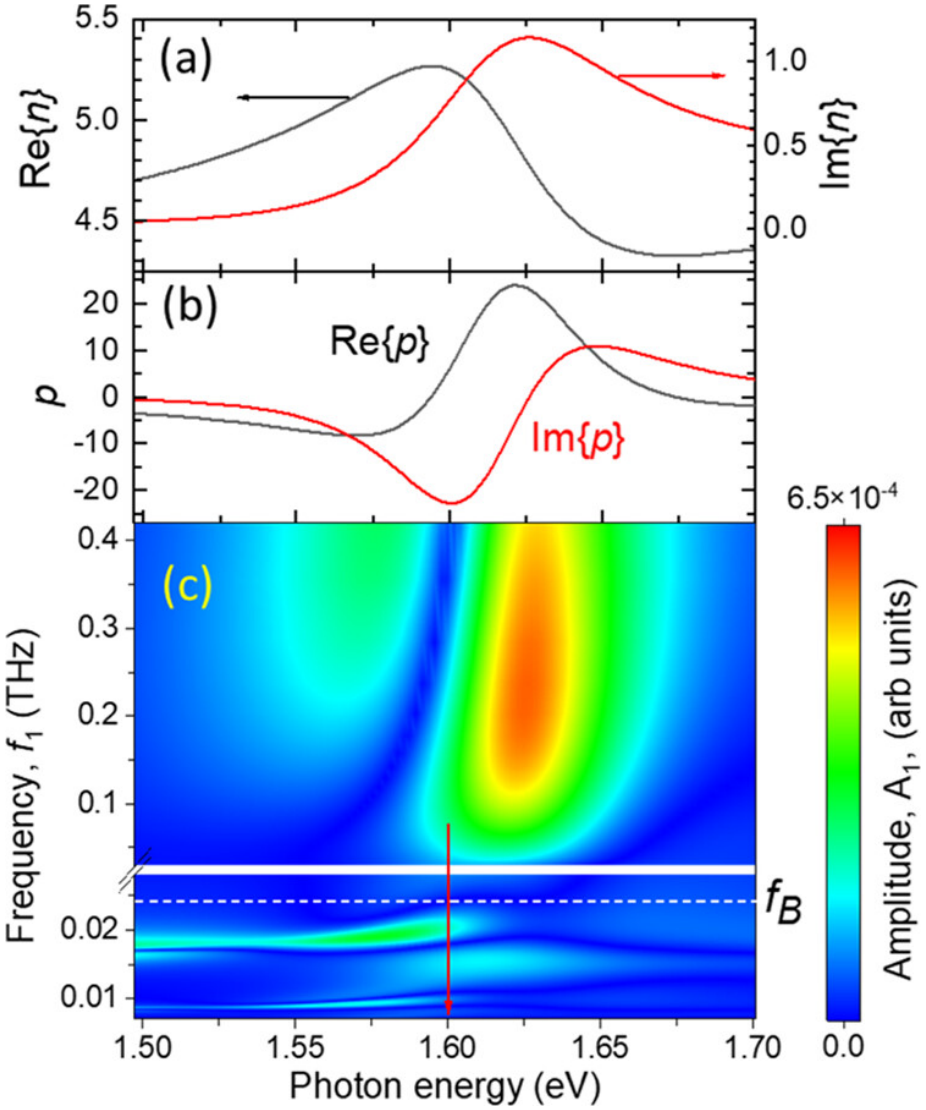


Figure 39: (a) The dependence of the real (black) and imaginary (red) parts of the refractive index, n, of WSe_2 on photon energy. Data collected from [161]. (b) The dependence of the real (black) and imaginary (red) parts of the reduced photoelastic constant, p, of WSe_2 on photon energy. At the used photon energy of 1.6 eV (indicated by the red arrow in panel (c)), the real part of p is greater than the real part of n. (c) Colourmap showing the amplitude of the fundamental frequency as a function of frequency and photon energy. There is a break in the frequency axis to display data collected near the Bragg condition, f_B, and far above it.

3.6 Conclusion

This chapter explored the interactions between phonons, photons, and excitons, specifically examining how photons in the proximity of the exciton resonance have increased detection sensitivity to phonons, which occurs in two distinct regions with different origins; however, both regions of increased sensitivity are due to the refractive index and the changing photoelastic constant mediated by excitons.

This work presents van der Waals films on an opal substrate, with film thicknesses ranging from 8 - 130 nm. This allows for longitudinal phonon modes of various fundamental frequencies to be excited, depending on the thickness of the film. The phonons are excited by lasers using the pump-probe regime, utilising ASOPS.

The experimental results indicate that when the fundamental frequency of the excited phonons is close to the Bragg condition for the probe laser, the sensitivity of the detection of the phonons is increased due to the photons reflected from the top and bottom layers of the flakes constructively interfering. There is also an observed example where the s = 3 higher-order mode has a larger amplitude than the fundamental harmonic; this is due to a second region of high sensitivity at frequencies much greater than those that satisfy the Bragg condition.

The theoretical explanation of these results shows that the phonon signals are primarily dependent on two factors: the refractive index of the material, which itself is wavelength-dependent, and the reduced photoelastic constant, which, away from the exciton resonance, has the form $p = dn_{probe}/d\varepsilon_{zz}$. However, the probe frequency lies close to the exciton resonance, changing the form of the reduced photoelastic constant to $p = \Xi dn_{probe}/d(\hbar\omega)$. This increases the reduced photoelastic constant. Therefore, in the region where the Bragg condition is satisfied ($f_1 < 25$ GHz), the reflectivity changes from having the refractive index being the leading parameter to the reduced photoelastic constant, which causes an amplification of the phonon signal. In the region where $f_1 > 25$ GHz, there is another region of reflectivity amplification. This amplification is due to the layer thickness and strain lowering the exciton energy, such that, for the same pump fluence, more excitons are excited and, upon decay, emit more photons that interact with phonons, thereby increasing the sensitivity of the measurement. Experimentally, an s = 3 harmonic, with frequency = 66 GHz and amplitude = 9×10^{-5}, was observed to have an amplitude greater than the fundamental frequency (amplitude = 4.5×10^{-5}). This suggests that this higher-order har-

monic lies within this region of increased sensitivity. Furthermore, this experiment opens discussion for the use of vdW ANCs for the development of single phonon devices, since the amplitude is approximately $S\varepsilon_{zz}$, where S is the sensitivity of detection, which in this case $S \approx 10$. And ε_{zz} is proportional to the square root of the phonon density $\sqrt{N_p}$. For a phonon generated with $f_1 = 100$ GHz, using a pump fluence of 0.15 mJ/cm^2, the amplitude is $A_1 \approx 10^{-4}$, and therefore the phonon density is $\approx 10^4$ phonons/μm^2. This means that to reach the single phonon limit, the pump fluence must be decreased by two orders of magnitude, which decreases the amplitude down to 10^{-6} and then results in a phonon density of 1 phonon/μm^2, which is detectable with current ASOPS equipment. This experiment enables further investigation into magnetic van der Waals materials [199, 200], which can be utilised to explore the phenomenon of strong coupling between phonons and magnons. Using this work, materials could be designed to select phonon frequencies and amplitudes that drive spin wave precession more efficiently.

4 Electrical Excitation and Detection of Magnons

4.1 Introduction

This chapter investigates the electrical excitation and detection of magnons in micro- and nanoscale structures fabricated from Galfenol films sputtered on GaAs substrates and attempts to explore magnon-phonon coupling in those structures. The magnetic part of each device consists of a 3 μm wide, 20 μm long Galfenol bar fabricated using photolithography and ion milling. To excite magnons, an on-chip microwave antenna was fabricated in close proximity to the Galfenol bar. The excited magnons pump spin-polarised electrons into a layer of platinum sputtered on top of the Galfenol. The pumped spin-polarised electrons produce a spin current in the platinum layer, which, due to platinum being a spin Hall material, causes a charge current to be produced through the inverse spin Hall effect (ISHE), enabling detection of the magnons.

To investigate the coupling between magnons and phonons, the magnetic part of the device was incorporated within a phonon cavity. The phonon cavities were made by fabricating two different nanostructures. The first is a nanograting [201, 1] that is ion-milled into the magnetic part of the device, where the magnons are excited. The second nanostructure used was a GaAs/AlAs superlattice [202, 203], where the microwave antenna and magnetic bar are fabricated on top of the superlattice. A cartoon of both of the devices used is shown in Figure 40. To understand the magnon spectra experimentally measured, micromagnetic simulations are undertaken to model the magnetic part of the device. The results show a variety of magnon modes, including backwards volume modes (BV) and Damon-Eshbach modes (DE). The spatial profiles of these modes are also calculated to determine whether they are centre or edge modes.

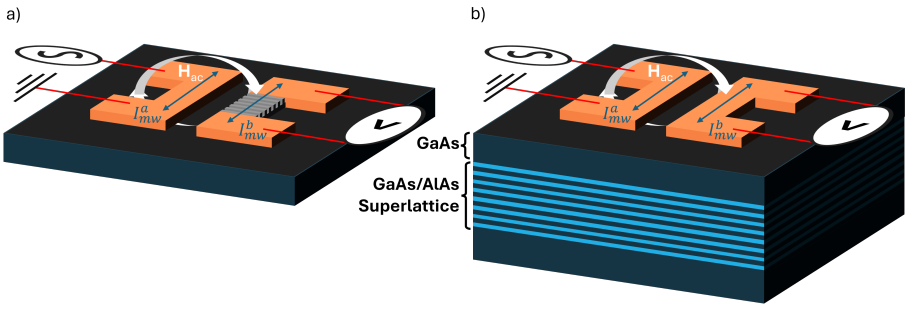


Figure 40: a) A schematic diagram of a nanograting device. The device structure on the left is the antenna, with a microwave signal applied at the input, which induces an alternating current I^a_{mw}. This current then produces an alternating magnetic field H_{ac}, which allows for a current, I^b_{mw}, to be induced in the neighbouring magnetic Galfenol bar. The bar has a nanograting milled into the surface. A measurable voltage is present across the magnetic bar. b) A schematic diagram of a superlattice device. This device does not have the nanograting, but instead is fabricated above a GaAs/AlAs superlattice.

4.2 Methods

4.2.1 Setup

The experiments described in this chapter utilise a microwave signal generator to excite magnons. The signal generator used is an Anritsu MG3692C, with a frequency range of 10-20 GHz and an output power ranging from 0 to 20 dBm. To detect the voltage generated by the ISHE, a Stanford Research Systems model SR830 DSP lock-in amplifier was configured, with the internal reference signal also modulating the microwave signal. The samples were mounted on a sample stick and connected to instruments via semi-rigid SMA cables, due to their low attenuation at high frequencies (> 10 GHz) [204]. The sample stick is designed to fit into a cryostat, which features an electromagnet positioned at its base. However, the cryostat's cooling properties are not utilised in this experiment; all experiments are conducted at room temperature. The electromagnet consists of two water-cooled copper coils and can produce a magnetic field of up to 400 mT. A Kikusui PWR800M power supply provides the current supplied to the coils. The samples used were layers of Galfenol with a gallium concentration of 19%, which were characterised previously by S. Bowe and D. Parkes [36, 132]. The Galfenol layer was fabricated into a microwave antenna and a rectangular bar with dimensions 3 x 20 μm^2 (the fabrication is discussed

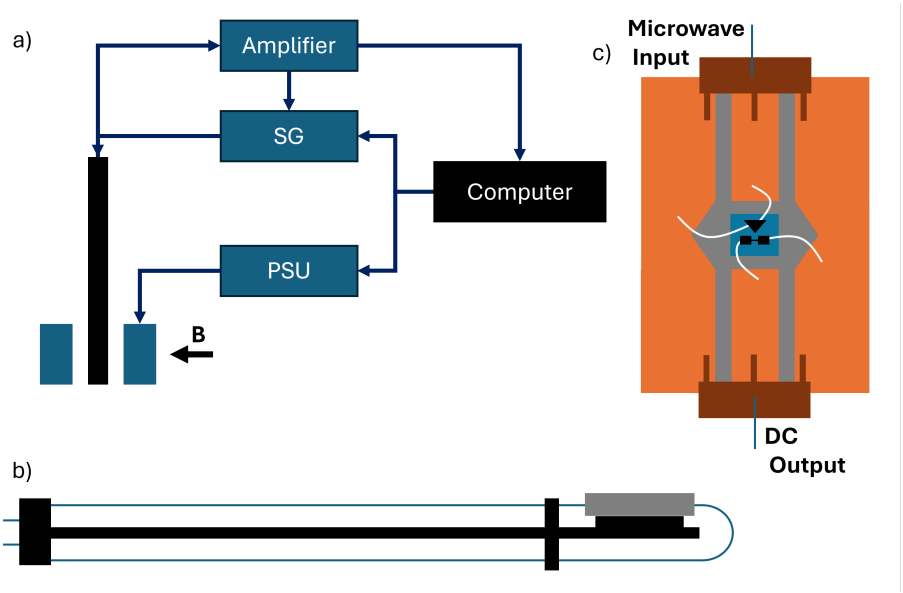


Figure 41: a) An illustration of the electrical setup that uses the lock-in amplifier and signal generator (SG) and power supply unit (PSU). b) An illustration of the sample stick where the rigid SMA cables connect to the top and bottom of the sample holder. c) An illustration of the sample holder where the sample is placed in the centre directly on top of the substrate with the aluminium wires bonded from one terminal to the device and then from the device to the ground.

further in Chapter 4.2.2). The antenna was designed to maintain a 50 Ω impedance across the device, while minimising capacitance and overall fabrication time [205]. Contacts to the rectangular bar were used to detect a DC voltage through the inverse spin Hall effect (ISHE). The phase of the lock-in amplifier was adjusted such that at the maximum applied external field, the signal in the x-channel is maximised. The experimental setup, the sample stick and the sample holder are illustrated in Figure 41. Finally, in order to measure the phonon modes in the structures, a pump-probe experiment was undertaken, utilising the ASOPS technique described in Chapter 2. The lasers used in this case are Tsunami Ti-sapphire oscillators from Spectra Physics. This setup was used to detect phonons in three different samples: two were nanogratings with different thicknesses of Galfenol (20 nm and 30 nm), and the third was a superlattice with a Galfenol layer sputtered on top.

4.2.2 Materials and Devices

Within these works, four different layers of Galfenol were used. Each of these layers was deposited as described in Chapter 2.3.2. These layers are named S1, S2, S3 and S4. Each of the sample thicknesses and the platinum capping layer thicknesses are listed in Table 2. All of these samples were produced via magnetron sputtering on a GaAs [100] layer. For sample S3, there was a superlattice structure grown via molecular beam epitaxy (MBE), topped with a 4 nm GaAs layer, which then had the 100 nm Galfenol and 5 nm platinum layers sputtered on top. The superlattice structure consists of repeated units of AlAs and GaAs with thicknesses of 108.6 nm and 90.5 nm, respectively. These repeated units are layered 10 times to impose boundary conditions on phonons in the z-direction. The combination of the superlattice structure, the GaAs top layer, Galfenol, and the Pt capping layer constitutes the phonon cavity as a whole [206]. A rough estimate for the allowed frequencies of the phonons, only taking into account the superlattice, is given by [207]:

$$f_n = n \frac{1}{\frac{c_{GaAs}}{d_{GaAs}} + \frac{c_{AlAs}}{d_{AlAs}}} \tag{90}$$

where f_n is the frequency of the nth harmonic, n is an integer, C_i is the speed of sound in each material of the superlattice and d_i is the thickness of each material in the repeated unit. In this case, d_{GaAs} = 90.5 nm, c_{GaAs} = 4.73 ms^{-1} [208], d_{AlAs} = 108.6 nm, c_{AlAs} = 5.65 ms^{-1} [208], resulting in the superlattice having a fundamental phonon mode of 13.0 GHz. The repeating units are capped with a 4 nm GaAs layer, onto which the Galfenol layer is sputtered. The thickness of the capping GaAs layer is smaller than previously used, as only the surface is required for the seeding of single-crystal galfenol and for the imparting of the uniaxial anisotropy component, but the layer should be thin enough to allow for the excitation of phonons within the superlattice from the surface galfenol. In previous laser experiments, the GaAs substrate was thicker (0.5 mm) because optical absorption was required only in the galfenol layer. The deposition of the superlattice structure was performed by Dr Richard Campion at the University of Nottingham.

The nanofabrication steps for each of the sample wafers begin with scribing each into 5 mm x 5 mm chips. Following this, the chips were then cleaned in 3 solvents in the order acetone, methanol and finally IPA at room temperature, using a vibration stage to provide gentle agitation for 10 minutes each. Once the chips were cleaned, they were then prepared for photolithography. The first step in the

	Thickness (nm)	Pt cap Thickness (nm)
S1	20	10
S2	30	5
S3	100	5
S4	100	5

Table 2: The different sample thicknesses along with the thickness of the platinum cap

photolithography process involves spin-coating photoresist on top of the chips. Based on the photomask design, a positive photoresist was required; given the high resolution of 0.5 μm and the lift-off structure produced, AR-P 5350 was used. The chip was placed in the Laurell spin coater, a drop of AR-P 5350 was applied on top, and the sample was spun at 4000 rpm for 60 s. After spin coating, the chip is baked for 4 minutes at 105°C. Following this step, the chip is placed in the MJB3 mask aligner so that the device structure on the photomask is either 45° or 90° to the sample edge. The chip is then exposed for 5 s to UV light from a mercury lamp, which weakens the resist in the regions exposed. Next, the chip is agitated in a development solution composed of a 1:3 ratio of AR300-35 and deionised water for 45 s. The development step removes the resist from the regions where the resist was weakened. The chips were then ion-milled using argon ions with an acceleration voltage of 200 V for a time to etch fully through the Galfenol layer. To remove the excess resist, the chips were placed in acetone at room temperature in an ultrasonic bath at the lowest power setting for 20 minutes, followed by rinsing in IPA.

Nanogratings, with troughs of width 100 nm and pitch 200 nm and depth of 10 nm, were fabricated along the Galfenol bar samples S1 and S2. The fabrication steps involved electron-beam lithography (EBL), the deposition of a hard mask (Cr), and ion milling. The sequence of steps is depicted in Figure 42. The EBL steps were carried out by Sarah Heywood and Richard Cousins using electron-beam resist CSAR 6200.09 and developer AR600-71.

Figure 43 shows an example of a completed device. Each of the chips is named based on whether it has a phononic resonator or is a control sample, as well as the orientation of the device with respect to the sample edge; the names of each chip is shown in Table 3.

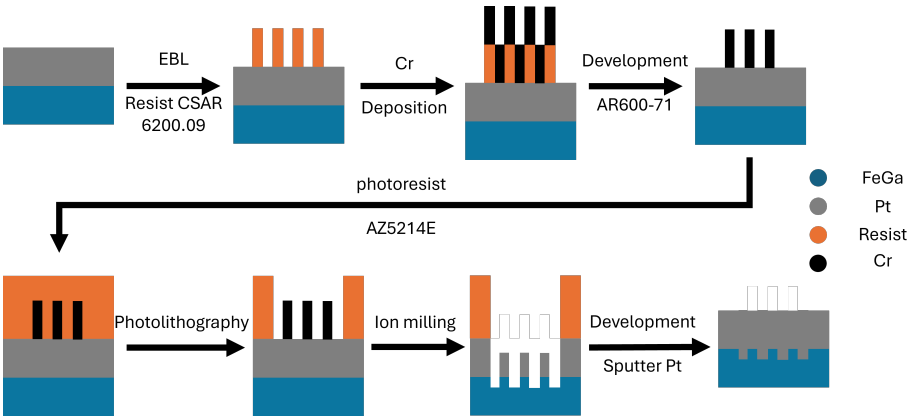


Figure 42: An illustration showing the fabrication steps to produce the nanogratings on the surface of the Galfenol.

	Grating(angle)	Control(angle)	Superlattice(angle)
S1	G3(45)	C3(45)	n/a
S2	G1(45), G2(90)	C1(90), C2(45)	n/a
S3	n/a	n/a	SL1(45), SL2(90)
S4	n/a	C5(45), C6(90)	n/a

Table 3: The names of each wafer and the samples fabricated from them. The labels G, C, and SL indicate whether the sample has a nanograting, is a control, or is a superlattice. The number in brackets is the angle of the magnetic bar with respect to the crystal edge.

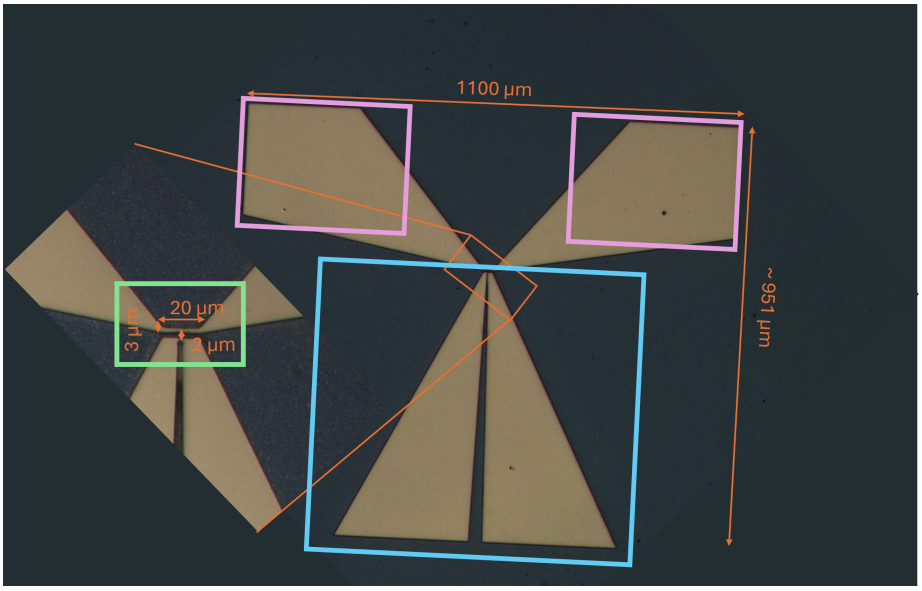


Figure 43: A 50x magnified light microscope image of a completed device showing the relevant lengths of the complete device. The inset is at 100x magnification. The magnetic bar and the space between the microwave antenna and the DC line are highlighted by a green box. The pink boxes highlight the contact pads. The blue box highlights the microwave antenna.

4.3 Results

4.3.1 Data Analysis

An example of the raw data collected from the microwave experiment is shown in Figure 44. The plot shows the DC voltage measured across the magnetic bar as a function of the applied magnetic field. The main features in the data are the magnon resonances, represented by asymmetric features at approximately ± 250 mT. There is also an asymmetric background that saturates at high magnetic fields and is therefore associated with the static magnetisation. This data needs to be processed in order to extract the information about the magnons. The first step in the process removes the small offset in each of the data traces, the origin of which is likely to be an instrument offset. The next step normalises the data such that the

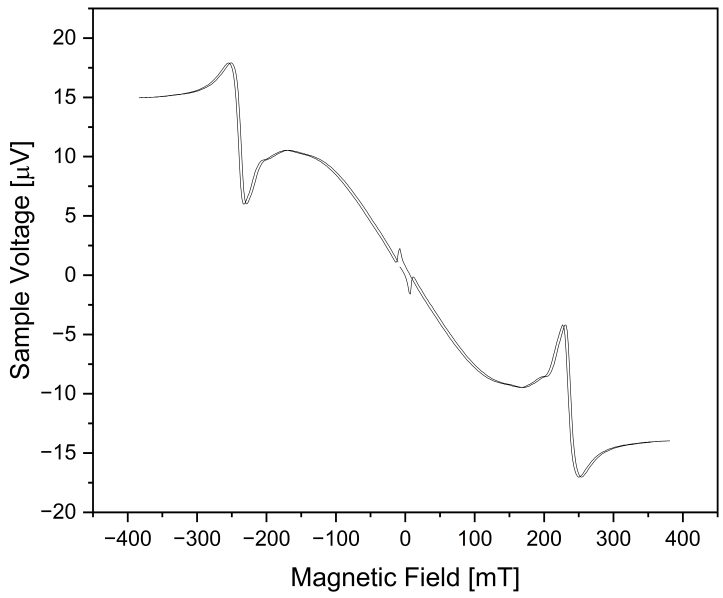


Figure 44: The data collected from the microwave experiments before any processing is done. The magnon excitation is at approximately ± 250 mT as well as a small hysteresis around 0 mT. For this data, the microwave input has a frequency of 18.9 GHz and a power of 63 mW, and the device used is C2. The external field is applied at 45° with respect to the magnetic bar.

asymmetric background voltage varies between -0.5 and 0.5 μV at the highest magnetic field. This is done because the power transmitted to the device from the antenna is frequency dependent, and

we do not have a direct measurement of the power at the device. As shown in Figure 45a), the asymmetric background varies as a function of the frequency. For one sample, we conducted an experiment where we varied the microwave power at a fixed frequency. Figure 46 shows that the magnitude of the asymmetric background is approximately proportional to the power. Therefore, we used the magnitude of the background signal as a proxy for the microwave power reaching the sample, which is accounted for by normalising the data with respect to the magnitude of the background, producing Figure 45b).

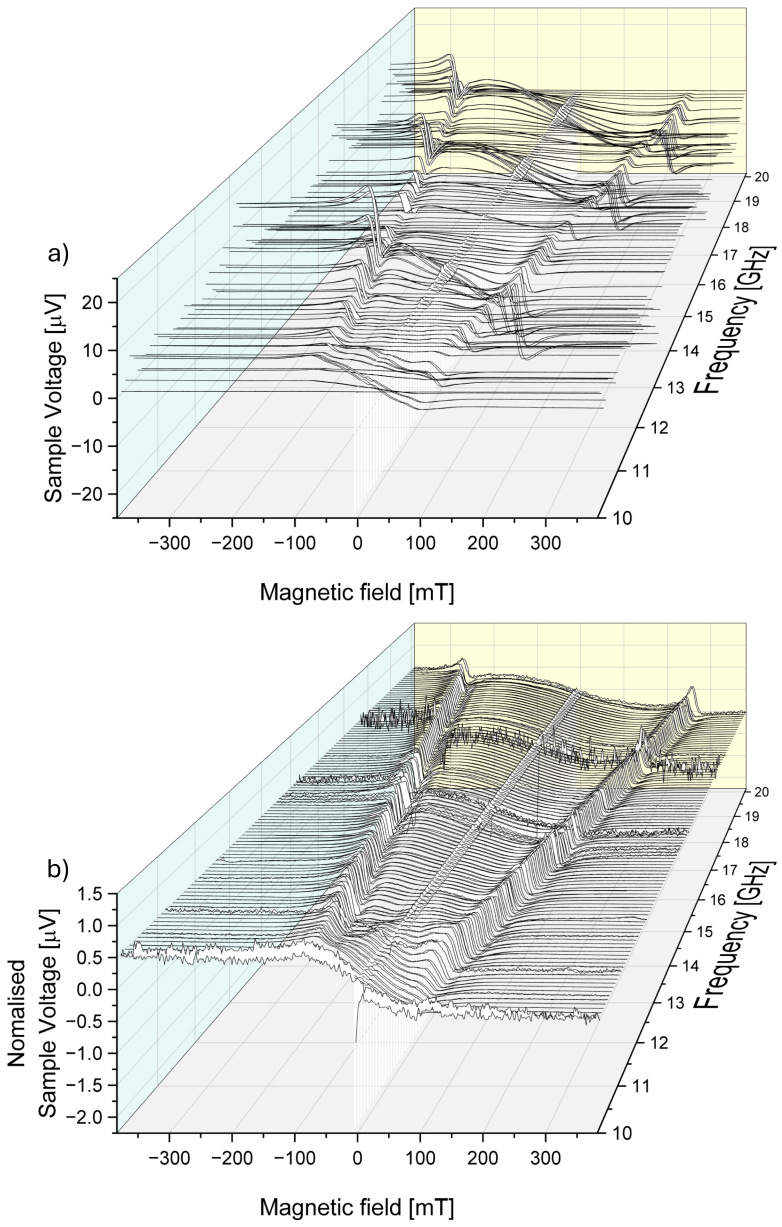


Figure 45: a) A waterfall plot of the voltage measured from sample C2, where the microwave signal is increased from 10 - 20 GHz in 0.1 GHz steps. This shows that the amplitude of each signal differs with frequency. b) The same waterfall plot, but the voltage measured from the sample is normalised such that the 'tails' are at ± 0.5 μV.

Three different methods were used to analyse the data. The first method of analysing the data fits an exponential decay function to the data, with the fitting function prioritising the low field (0 - $\pm$20 mT) and high field regions ($\pm$300 - $\pm$400 mT). The val-

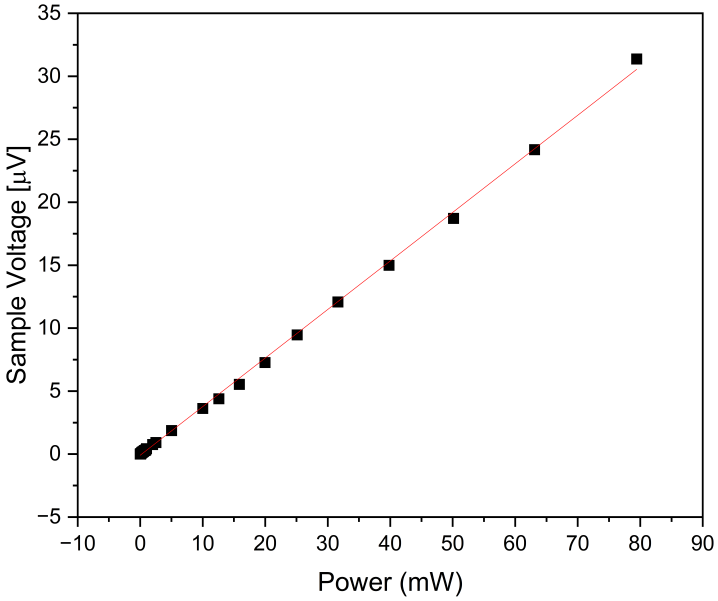


Figure 46: The magnitude of the asymmetric voltage background plotted against the power of the microwave signal from the signal generator. The signal generator frequency is 18.9 GHz, the sample used is C2, and the power is varied between 0.08 - 79 mW. The red line is a linear fit to the data. This shows that the relationship between the input power and the amplitude of the background voltage is linear.

ues of the function are then subtracted from the data to remove the background; the resultant data is the residuals of the fitting process. An example of the fitting used to produce the residuals and the normalised data is shown in Figure 47. The residuals are then collected across multiple input frequencies, enabling a colour map to be produced that shows how the magnon mode varies with applied frequency and external field. The second and third methods of analysing the data are similar in operation. The forward sweeps (0 - ±400 mT) and the backwards sweeps (± 400 - 0 mT) are paired together, and then the negative field data is flipped about x = 0. Following this, flipping the data can either be added or subtracted, resulting in the methods referred to as the addition and subtraction methods. These methods are used due to the data containing odd and even components; therefore, by adding the data together, the odd components of the total function are removed, whereas by subtracting the data sets, the even components of the

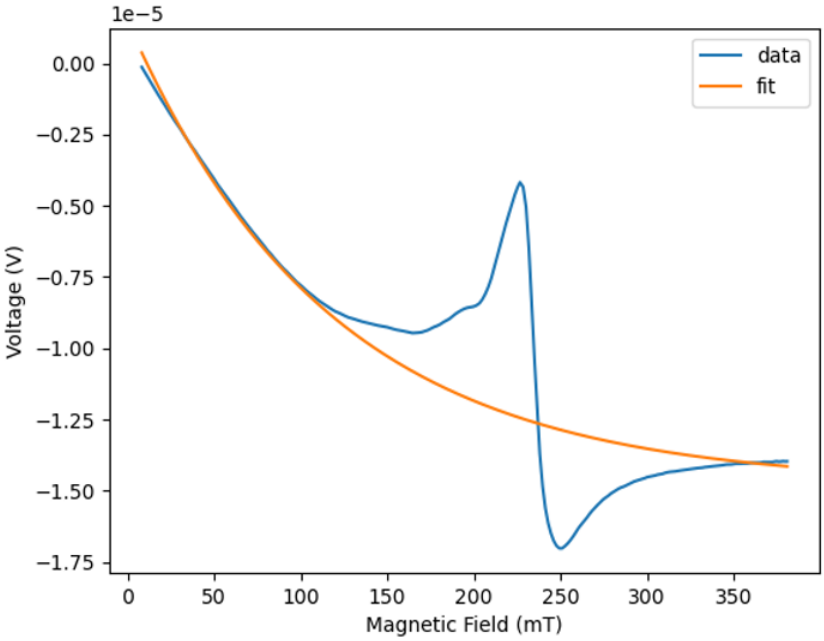


Figure 47: The fitting used to remove the background signal compared to the normalised data. This data is the same as that used in Figure 44, where the field is swept from 400 - 0 mT. The function used to fit the background is an exponential decay function given by $V = Ae^{-(H-x_0)/t} + b$, with the fitting parameters found to be $A = 4.48 \times 10^{-9}$, $x_0 = 955$, $t = 117$, $b = -1.45 \times 10^{-5}$.

underlying function are removed. Skinner et al. [209] used a very similar experimental method to investigate magnons in cobalt microbars. They noted that the DC voltage features generated by magnons in their Co/Pt structures can arise from two main phenomena: the ISHE due to spin pumping from the Co layer into the Pt layer, and a voltage contribution from the AMR, which arises due to the induced microwave current in the Co layer interacting with the magnetisation-dependent resistivity of the layer. The features associated with the magnons can be fitted to a Lorentzian with antisymmetric and symmetric parts, such as in Figure 48. From the

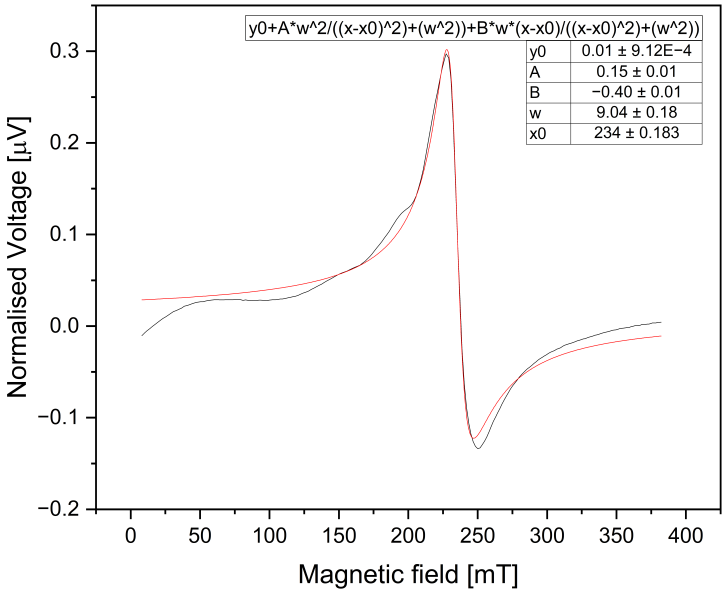


Figure 48: The magnon excitation with both anti-symmetric and symmetric Lorentzian fits applied. The microwave frequency applied was 18.9 GHz, and the external applied field was at 45° to the magnetic bar. Here, x_0 is the resonant magnetic field, w is the magnetic linewidth of the excitation, y_0 is the offset voltage, A and B are the magnitudes of the symmetric and the antisymmetric parts as shown in equation 91, where $A = V_{AMR}\cos\phi + V_{ISHE}$ and $B = V_{AMR}\sin\phi$.

works of Skinner [209], it is shown that the even components of the function are due to the ISHE and AMR and that the odd compo-

nents are due to only AMR. With the equation taking the form:

$$\begin{aligned} V_{dc} =& (V_{AMR}\cos(\phi) + V_{ISHE})\frac{\Delta H^2}{(H-H_0)^2+\Delta H^2} \\ &+ V_{AMR}\sin(\phi)\frac{\Delta H^2(H-H_0)}{(H-H_0)^2+\Delta H^2}. \end{aligned} \tag{91}$$

Where V_{dc} is the dc voltage measured by the lock-in amplifier. V_{AMR} is the voltage component due to AMR, V_{ISHE} is the voltage component due to the ISHE. ϕ is the phase difference between the magnetisation precession and the current coupled to the magnetic strip from the microwave antenna. ΔH is the linewidth of the magnon signal, H is the external magnetic field, and H_0 is the magnon resonant field. The voltage due to AMR is given by

$$V_{AMR} = \frac{1}{2} I^b_{mw} \Delta R A_{xx} sin(2\theta) h_z \tag{92}$$

where I^b_{mw} is the current coupled to the magnetic strip from the microwave antenna. ΔR is the AMR coefficent, A_{xx} is related to the xx-component of the susceptibility by $A_{xx} = \chi_{xx}/M_S$. θ is the angle between the magnetisation and the length of the bar, and h_z is the amplitude of the microwave magnetic field. The voltage from the ISHE is expanded by

$$V_{ISHE} = \theta_{SH} w (\frac{2e}{\hbar}) \lambda_{sd} tanh(\frac{d_{pt}}{\lambda_{sd}}) j^0_s R sin\theta. \tag{93}$$

Here, θ_{SH} is the spin Hall angle, w is the width of the bar, λ_{sd} is the spin diffusion length of platinum, d_{pt} is the thickness of the platinum, j^0_s is the initial spin current, and R is the sample resistance. The AMR voltage is dependent on $\sin(2\theta)$, whereas the ISHE voltage depends on $\sin(\theta)$. This difference in the angular dependence between the two sources of the voltages means that by sweeping the field from positive to negative the angle changes by 180°, which due to the dependences on θ suggests that the voltage due to ISHE changes in sign whereas the voltage component due to AMR keeps the same sign, this suggest that the subtraction method as well as extracting the even components which contains the ISHE and AMR terms leaves intact the ISHE terms while reducing the AMR term. The fitting parameters shown in Figure 48 suggests that AMR is the dominant effect due to the magnitude of the fitting parameter responsible for solely AMR being, $|B| = 0.4\ \mu$V, which is double the magnitude of the fitting parameter which includes both the AMR and ISHE effect terms, $|A| = 0.2\ \mu$V. Figure 48 also shows that

the magnetic linewidth measured at 18.9 GHz is 9.0 mT, which, compared to the results from Skinner [209] of 30 mT measured at 23 Hz in Co and Parkes [131] of 8.7 mT measured at 10 GHz in Galfenol, suggests the measured signals are of the order expected for this material. The magnetic linewidth can also be used to find the frequency linewidth using the gradient from Figure 50 to produce $\Delta f = 0.5$ GHz; the lifetime of the magnon is then estimated to be ≈ 2 ns. Comparing this to an example where strong coupling was observed [1], where the lifetime was found to be 5.9 ns, our magnons decay three times faster.

From the electrical measurements, each of the samples in Table 3 was measured in two field orientations, except for sample C1, due to its being damaged. These field orientations are 45° and 90° with respect to the bar of magnetic material. The 0° orientation was not of interest since equations 92 and 93 show that at 0° both of these voltages are zero. Whereas at 45° the AMR voltage is maximised and the ISHE voltage is non-zero, and at 90° the AMR voltage is zero but the ISHE voltage is maximised. A single device was measured with the magnetic field oriented at 0° to confirm that the measured voltage shows no features; this is shown in Figure 49.

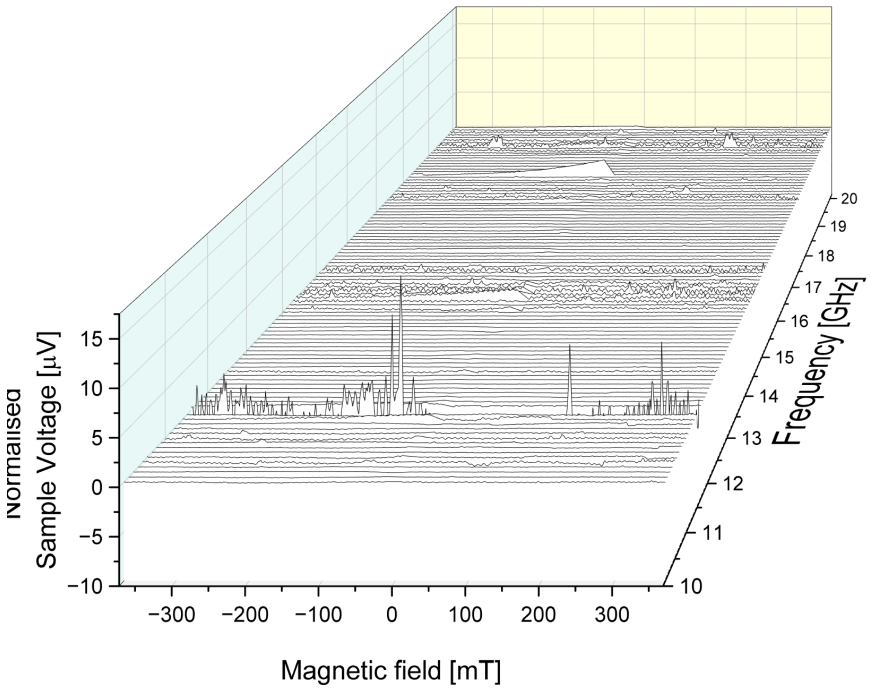


Figure 49: A waterfall plot of the measured voltage of sample SL1, where the applied magnetic field is oriented at 0° to the magnetic bar. Clearly, there are no discernible features as is expected for this orientation.

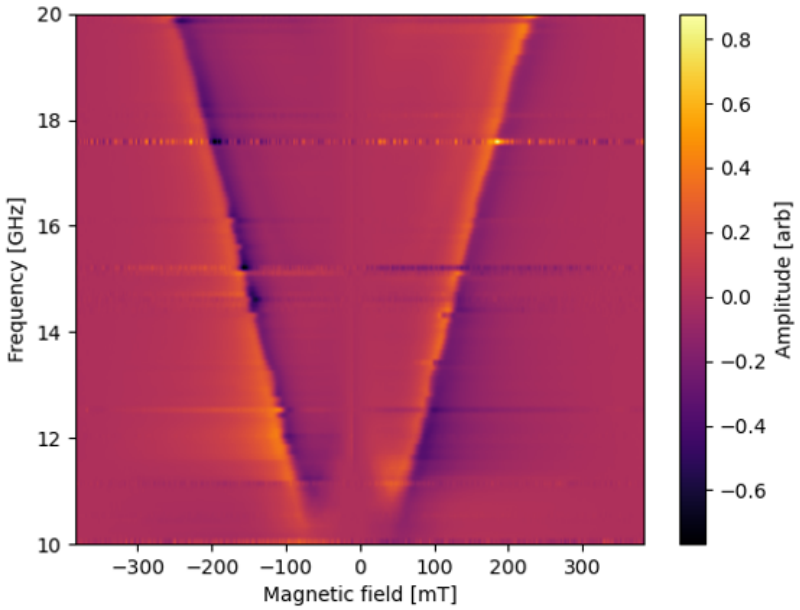


Figure 50: Sample C2 with the magnetic field applied at 45°. The figure is processed by taking the data from Figure 45 and finding the residuals as shown in Figure 47. A colourmap is then produced with the residuals data. This figure shows a magnon mode with an approximately linear dependence of frequency on applied field.

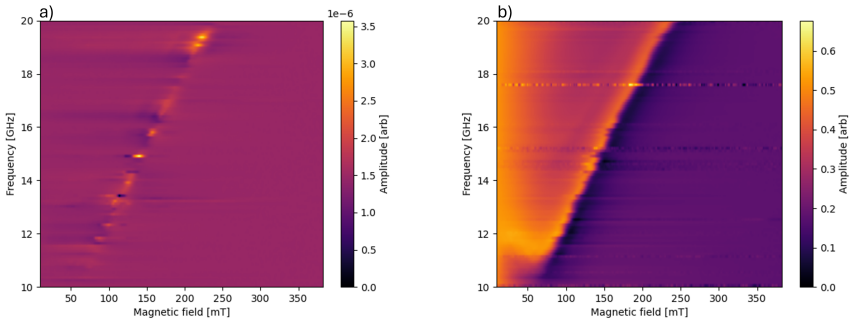


Figure 51: Sample C2 with the magnetic field applied at 45° processed via a) the addition method, which shows both the ISHE and a component of the AMR effect. b) shows the subtraction method, which only contains a component of the AMR effect.

An example of the data collected with the magnetic field applied at 45° is shown in Figure 50, which depicts the control sample C2. These results show a positive, approximately linear relationship between the magnetic field and the frequency. Figure 51 shows the same data as Figure 50, but subtraction and addition methods have been applied to separate the ISHE and AMR components. Figure 51b) shows a clear resonance line which suggests strong AMR effects, whereas Figure 51a) shows a less distinct line, with gaps. Since ϕ is not known, it cannot be determined whether this is also due to AMR or the ISHE; however, it is clear that the AMR effect is dominant overall, which is in agreement with the fitting parameters shown in Figure 48.

When the magnetic field is oriented perpendicular to the magnetic bar in sample C2, a different magnon mode is observed. This magnon mode's frequency dependence on the magnetic field differs from the typical results seen, where the frequency increases with increasing magnetic field. Instead, this magnon frequency decreases with increasing magnetic field up to a critical field value. An example of this type of magnon mode is shown in Figure 52. The origins and classification of this magnon are explored in Chapter 4.4.2.

The observable difference between the magnon mode in Figure 50 and the magnon mode in Figure 52 is that the mode in Figure 52 shows a decrease in frequency with increasing magnetic field. This decreasing frequency continues until the internal demagnetising field is overcome by the externally applied field; the magnon frequency then begins to increase with applied magnetic field. This will be further shown in Chapter 4.4.2. Because Figure 52 shows complex coupling interactions, the samples exhibiting these interactions were further explored with higher-resolution scans around the frequencies at which these modes occur. These high-resolution scans were not undertaken for each sample due to time constraints. High resolution scans of sample C2 with the magnetic field at 90°, with a frequency range of 10.5-12 GHz, are shown in Figures 53a and 53b. These figures show a magnon mode which decreases in frequency as the magnetic field increases. Figure 53b) shows bright spots at frequencies of 11.59, 11.65, and 11.71 GHz; these suggest a resonant interaction. Figure 53a) shows an anticrossing at 10.82 GHz, which suggests there is strong coupling. Since these measurements are in the control sample C2, these interactions are attributed to other magnon modes excited in the bar. Figure 54 shows the addition (54a)) and subtraction (54b)) data analysis methods for the data shown in Figure 53a). This again shows that AMR is the dominant effect in voltage generation when the magnetic field is applied per-

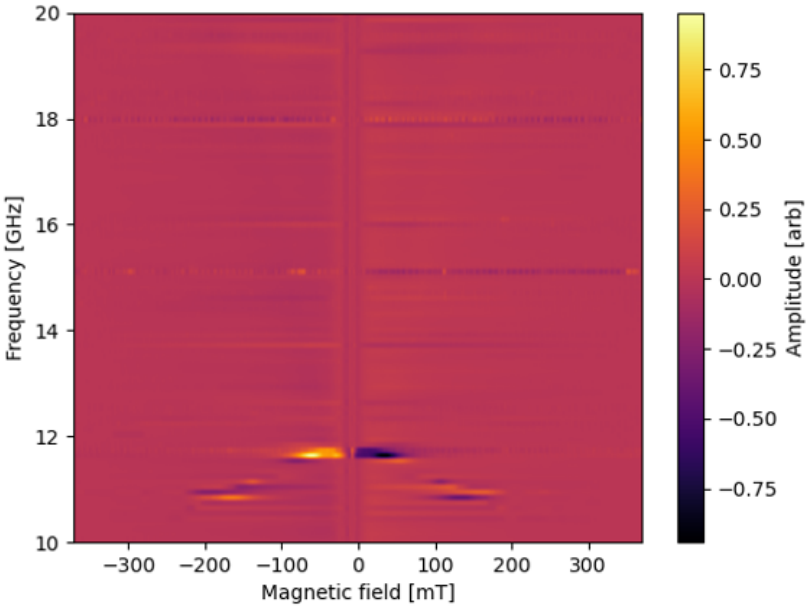


Figure 52: Sample C2 with the magnetic field applied at 90° processed by the exponential fitting method. This sample and field geometry shows magnons that decrease in frequency with respect to the magnetic field.

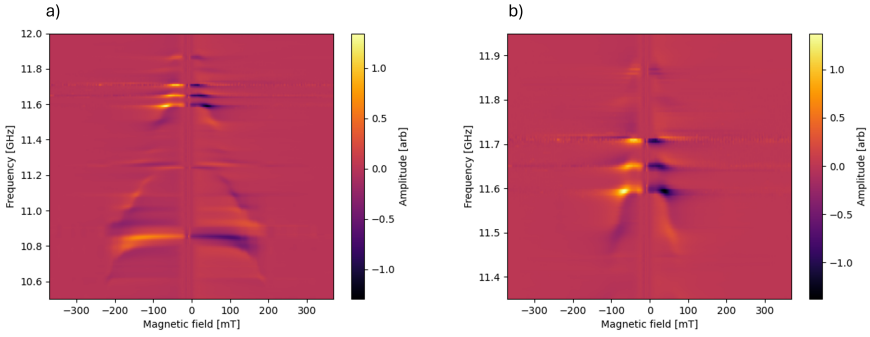


Figure 53: Higher resolution scan of sample C2 with the magnetic field at 90° a) shows the full range of the magnon modes with a frequency resolution of 0.01 GHz, and b) shows a higher frequency resolution image (0.005 GHz) of where the modes cross at 0 mT.

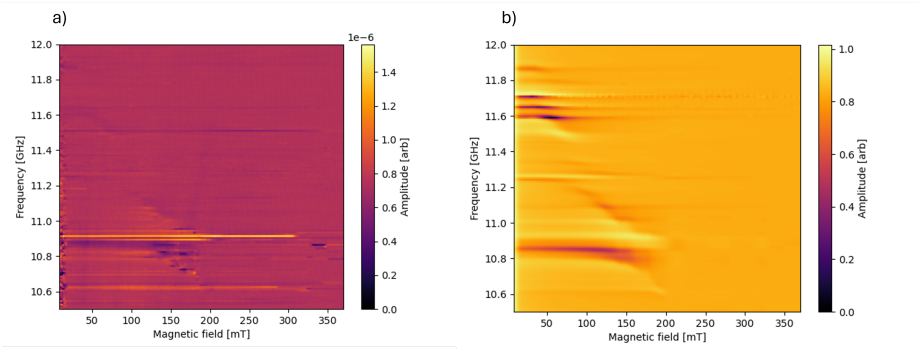


Figure 54: Sample C2 with the magnetic field applied at 90° processed via a) the addition method, which shows both the ISHE and a component of the AMR effect. b) shows the subtraction method, which only contains a component of the AMR effect.

pendicular to the magnetic bar in sample C2. These magnon modes that decrease in frequency as the magnetic field is increased are also observed in samples G3 (Figure A10), G2 (Figure A4), SL1 (Figure A14) and SL2 (Figure A18). This shows that the effect is observed across different sample thicknesses (20, 30, and 100 nm), different Pt cap thicknesses (10 and 5 nm), and across control samples and different nanostructures and crystallographic directions. The only observed similarity is that the external field is applied at 90° to the magnetic bar. This effect, however, is not observed in all samples when the magnetic field is applied at 90° to the magnetic bar, with devices C3 (Figure A8), G1 (Figure A6), C5 (Figure A12) and C6 (Figure A16) not producing this magnon spectra. This indicates that the effect is observed only in five of the nine devices measured in this orientation. We speculate that the quality of the bars was affected during fabrication, thereby altering the magnetisation profile across the edges of the bar.

Each of these samples exhibits the linear magnon structure shown in Figure 50. By examining the subtraction and addition plots for all samples, it is evident that the AMR contribution to the voltage is greater than the ISHE contribution. These extra experimental results are included in the appendix.

Overall, these results suggest that the AMR is predominantly responsible for the effects observed; therefore, the magnetic moments must not be entirely aligned with the external field, and the geometry of the sample and the field are also critical. This suggests that shape anisotropy and the internal field play a key role in this effect. To further explore the origins of the modes in these samples and the interactions, micromagnetic simulations were done.

ASOPS experiments were undertaken to explore the phonon modes within the nanogratings or superlattices in the devices. In these experiments, only the change in reflectivity was recorded, without any polarisation information, so only phonons, not magnons, were detected. The FFT signals for each of the grating samples are shown in Figures 55 and 56. Figure 55 shows the phonons in sample S1, where the resonant frequency is 10.5 GHz, with a secondary peak at 11.3 GHz, possibly due to imperfections from the fabrication process. The linewidth of the peak at 10.5 GHz is 0.4 GHz; therefore, the lifetime is 2.5 ns. The higher-frequency modes are not important because they lie above the measured frequency range and are attributable to the system's sampling rate and Brillouin oscillations.

Figure 56 shows the phonons in sample S2, where the phonon frequency is 10.9 GHz. The mode at 19.4 GHz is speculated to be a higher-order phonon mode that is shifted in frequency due to defects in the nanograting. The linewidth of the peak at 10.9 GHz is also 0.4 GHz, and the lifetime is again 2.5 ns. The higher-frequency modes are from the same origins as in Figure 55.

The superlattice results are shown in Figure 57. This shows the phonons in the superlattice are at 12.6 GHz. The linewidth of this peak is 0.8 GHz, which results in a lifetime of 1.25 ns.

Comparing the lifetimes of the phonons in our nanostructures to those in works where strong magnon-phonon coupling is observed [1], where the lifetimes are 33 ns, it is clear that the phonon lifetimes in our structures are much shorter. For the gratings, this is because our gratings were confined to an area of 3×20 μm^2, whereas in Godejohann's work the grating structure was larger, with an area of 25×25 μm^2. For the case of the superlattice, the lifetimes of the phonons are reduced due to the finite-size effect and the relatively low frequency of the phonons confined in the structure.
Figure 18 shows the magnon spectra measured for samples S1 and S2 with nanogratings, and for sample S3 with a superlattice structure, and corresponding spectra measured in control samples (without nanogratings or superlattices), all with the field oriented at 45 degrees to the bar.

There are no discernible differences between the data from the samples containing phonon cavities (nanogratings or superlattices) and the control samples, and no features that would suggest coupling between magnons and phonons across the measured frequency range, which includes the range where the phonon resonances have been identified in Figures 15 - 17. The samples where the magnetic field is applied perpendicular to the magnetic bar are not shown

in this comparison because we did not measure any corresponding control-nanostructure pairs which exhibit these magnon modes. Using the measured linewidths of the phonons and magnons, we can determine an upper bound on the coupling strength (g) that would be resolvable in principle from our measurements. Typically, the strong coupling limit is resolvable when the cooperativity, $C = g^2/\Delta f_m \Delta f_P < 1$. Therefore, a coupling strength of 0.6 GHz or more would be necessary in order to be resolvable from our data. This would exceed the coupling strength of 0.2 GHz observed in optical studies of similar nanogratings investigated in Galfenol layers [1].

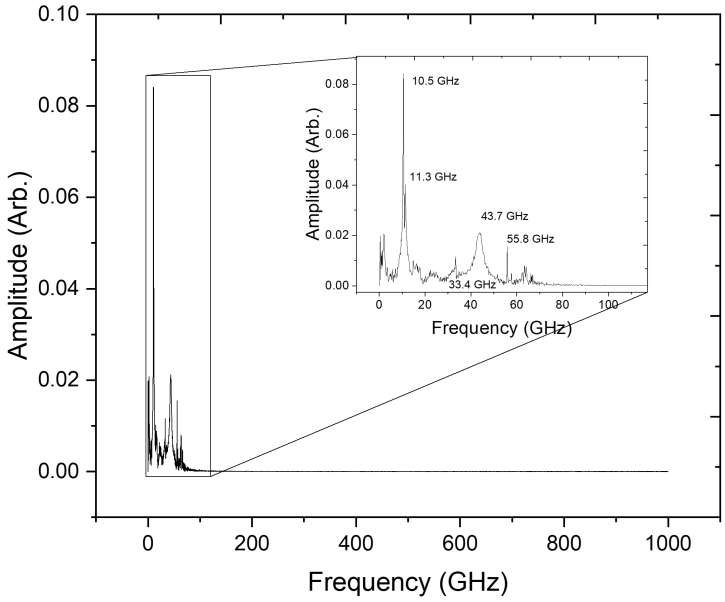


Figure 55: The FFT of the intensity signal measured by the BPR for a sample of S1 with a nanograting milled into the surface. This shows several peaks, with the modes of interest at 10.5 GHz and 11.3 GHz. The mode at 10.5 GHz is from the nanograting. The mode at 33.4 GHz is an artefact of the sampling rate of the apparatus. The mode at 43.7 GHz is due to Brillouin oscillations. The modes above 20 GHz are not of interest because these phonons cannot be resonantly excited by the generated magnons, which have a maximum frequency of 20 GHz due to the signal generator used.

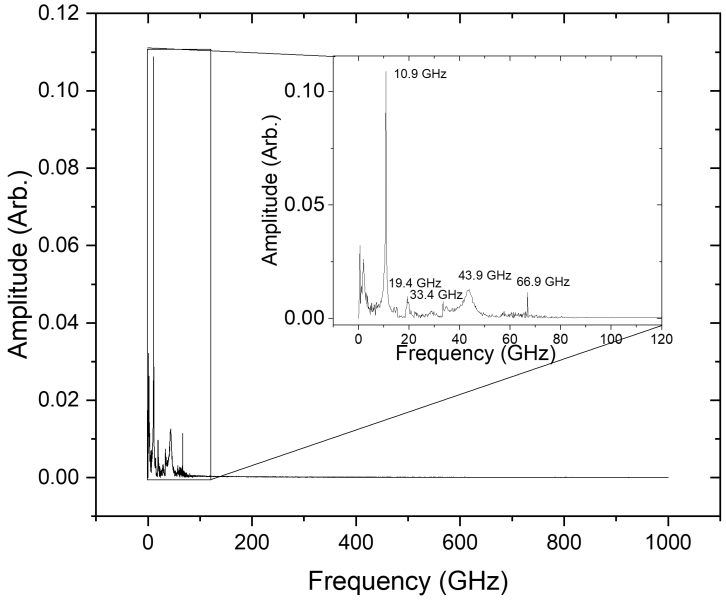


Figure 56: The FFT of the intensity signal measured by the BPR for a sample of S2 with a nanograting milled into the surface. This shows several peaks with the mode of interest being at 10.9 GHz. The mode observed at 19.4 GHz is speculated to be a higher-order phonon mode that is shifted in frequency due to defects in the nanograting. The mode at 33.4 GHz is an artefact of the sampling rate of the apparatus. The mode at 43.9 GHz is due to Brillouin oscillations. The modes above 20 GHz are not of interest because these phonons cannot be resonantly excited by the generated magnons, which have a maximum frequency of 20 GHz due to the signal generator used.

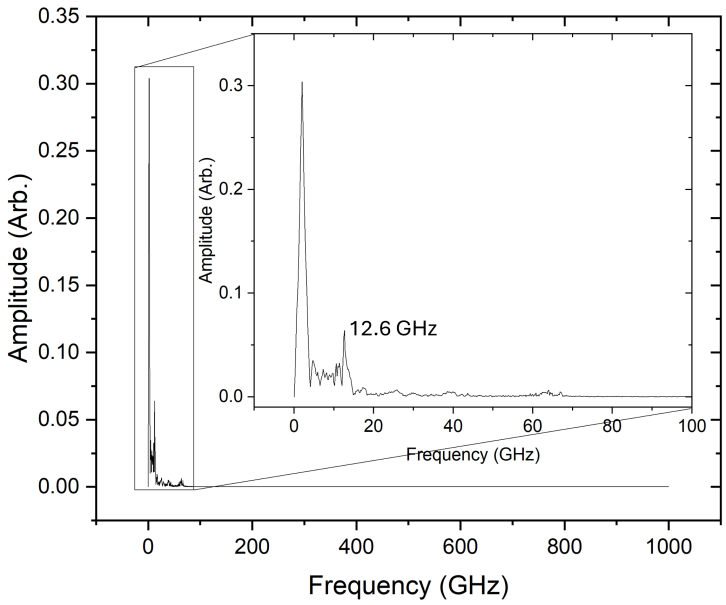


Figure 57: This shows the FFT of the intensity signal measured by the BPR for a sample of S3, which is grown on top of a superlattice. This shows several small peaks with the main mode of interest being at 12.6 GHz.

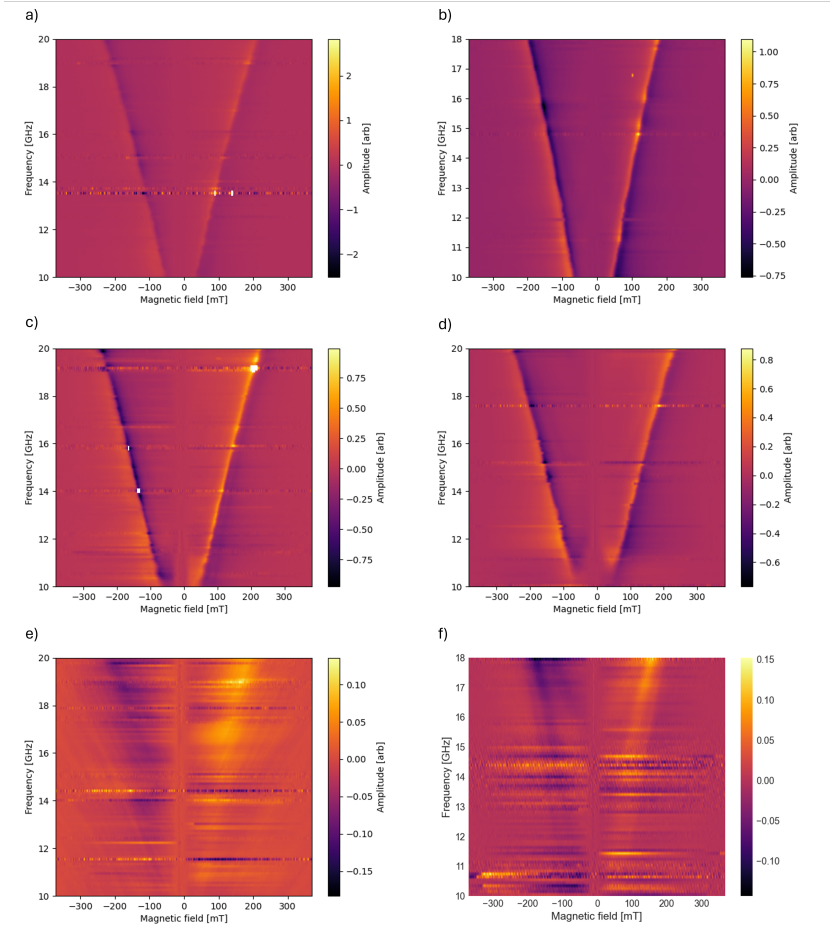


Figure 58: Each of these figures shows the frequency against magnetic field plots for the magnetic bar fabricated at 45° to the crystal edge, and the magnetic field is applied at 45° to the magnetic bar. a) An example of device G3 produced from sample S1 with a nanograting. There is no observed crossing or anticrossing at 10.5 GHz. b) An example of the control sample C3, which is produced from sample S1. The difference between a) and b) is that a) some noisy traces around 13.5 GHz, which is well away from the phonon frequency. c) An example of device G1 produced from sample S2 with a nanograting; there is no observed crossing or anticrossing at 10.9 GHz. d) An example of the control sample C2, which is produced from sample S2. There is no discernible difference between the control and the grating. e) An example of device SL1 produced from sample S3, grown on a superlattice. There is no observed crossing or anticrossing at 12.6 GHz. f) An example of the control sample C5, which is produced from sample S4. There is no discernible difference between the control and the grating.

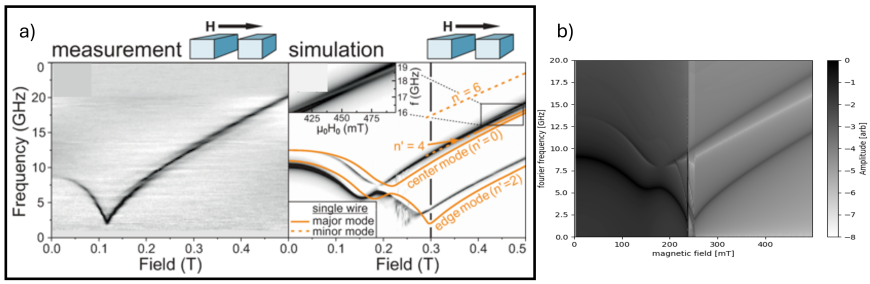


Figure 59: a) Experimental and simulated results that Langer et al. produced [210]. b) The reproduced results using Ubermag. The same two magnon modes are present at the same frequencies with inflexion points at the same fields. In the Ubermag simulation, there is a sharp change in amplitude at approximately 250 mT. This is due to a switch in the magnetisation orientation before saturation. Overall, the key features observed by Langer et al. are replicated.

4.3.2 Simulations

In order to understand the magnon spectra observed in our microbars when the field is oriented at 90 degrees to the bar, we performed micromagnetic simulations. The micromagnetic simulation package used was Ubermag [65]. To check the validity of our model, the first simulation sought to replicate the work of Langer [210]. The parameters used here were: depth = 36.8 nm, width = 140 nm, and the length is set to be infinite by using periodic boundary conditions. The saturation magnetisation is $\mu_0 M_0 = 0.9236$ T and the exchange stiffness, D, is 23.6 Tnm^2 [211, 212]. Therefore, only the Zeeman, exchange and demagnetisation interactions are taken into account.

Reproducing the Langer et al. results confirmed that Ubermag can produce reliable results for this geometry. These results are shown in Figure 59. The Langer et al. simulation results show two magnon modes, which at 0 mT are at approximately 10 GHz and 12.5 GHz. Both modes decrease in frequency as the field increases up to 150 mT; the lower mode then rises until 200 mT, at which point the two modes approach each other. After this point, the upper mode continues to increase in frequency, whereas the lower mode decreases until 300 mT, at which point the lower mode begins to increase. Each of these features is reproduced in the Ubermag simulations conducted. Furthermore, Langer et al. assign the upper mode as a centre mode and the lower mode as an edge mode by examining the spatial profiles of each mode and observing where the modes are localised in the samples.

Following this, the material parameters were changed to those

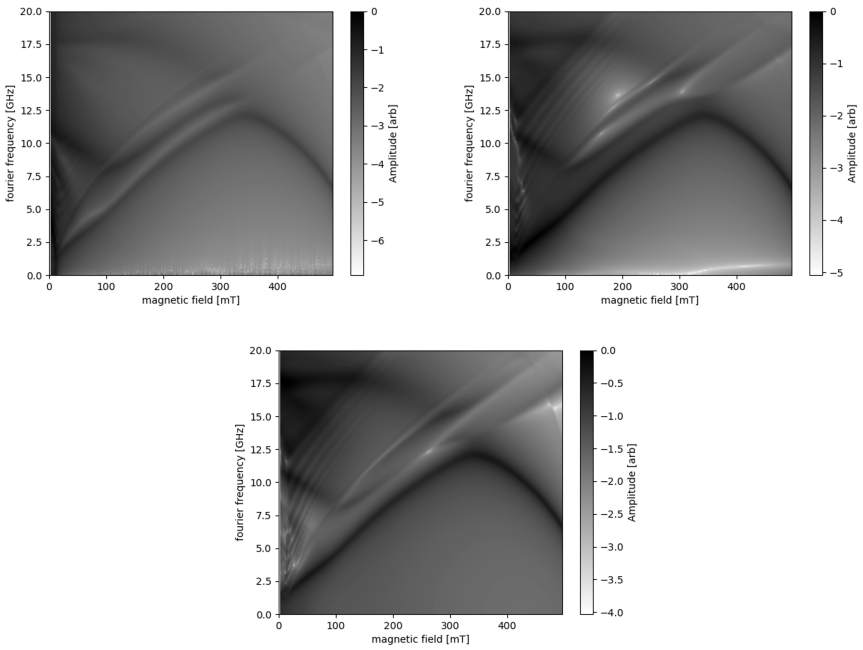


Figure 60: Simulation showing frequency dependence of the magnetisation precession as a function of the applied magnetic field for a bar with periodic boundary conditions in the y-axis, 3000 nm wide in the x-axis and 20 nm thickness. For these results, cubic, uniaxial, and shape anisotropies are included, as are the Zeeman and exchange interactions and the demagnetising field. a) The x component of the magnetisation. b) The y component of the magnetisation. c) The z component of the magnetisation.

of the galfenol, as well as including anisotropy terms; the cubic and uniaxial anisotropy energy densities are K_c = 33000 J/m^3 and K_u = 9000 J/m^3 [140]. The width of the bar was also increased from 140 nm to 3000 nm. The saturation magnetisation is 1.39×10^6 A/m, the unitless Gilbert damping parameter is 0.017 and finally the exchange constant is $A = 1.9\times10^{-11}$ J/m [213]. Comparing the narrower permalloy bar in Figure 59b) to the 3000 nm wide Galfenol bar (Figure 60), it can be observed that the magnons in the two materials largely show similar magnon structures with rising and falling modes. The difference between the two materials arises from the number of observed magnon modes in galfenol, which is due to the increased width of the simulated bar. Another key difference lies in the magnon initial frequency, which arises from differences in the magnetic parameters.

Figure 60, shows a large rising mode which increases in frequency

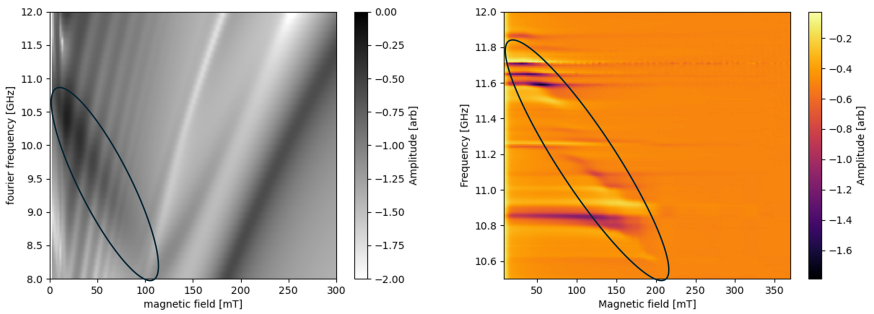


Figure 61: Here, the experimental results shown in Figure 54b) are compared to the simulated results. The main magnon mode is highlighted by the circle in either image. Furthermore, the simulation shows many rising modes, which may explain the many interactions with the prominent mode observed in the experimental results.

as the magnetic field increases up to ≈ 350 mT, where a falling mode intersects it and continues to decrease in frequency. Figure 60 also appears to show many modes which interact with a falling mode at approximately 20 mT; this interaction appears to change these modes into rising modes. A deeper analysis of why this switch from decreasing to increasing field is presented in the theory Chapter.

The results of the 3 μm wide bar with anisotropy can be compared to the experimental results; this comparison is shown in Figure 61. Clearly, within the simulation, many modes are excited that are not observed in the experiment. To characterise each of these modes, the spatial distribution of these modes for various applied field values was explored. To process the data to extract the spatial distribution of the magnon modes, the magnetic field is fixed, and a sample of the cells defined in the simulation is taken. In this case, the cells are taken from the central yz plane, and every cell in the x-direction of this plane is taken. The time dependence of each of the magnetisation components in each cell is recorded. By taking the FFT of the magnetisation in each cell, the time domain is changed to the frequency domain. Finally, each of the transformed magnetisation components is arranged by the cell coordinates, which produces the position-dependent frequency figures seen in Figure 62. This figure shows that for low field values 0-200 mT, many modes exist, with the highest amplitude modes being confined to the edges of the sample; however, some lower amplitude modes exist solely in the centre of the bar. Above 200 mT, there are fewer of these centre modes, and the spatial distribution shows that the remaining modes are confined only to the edges of the sample. However, there

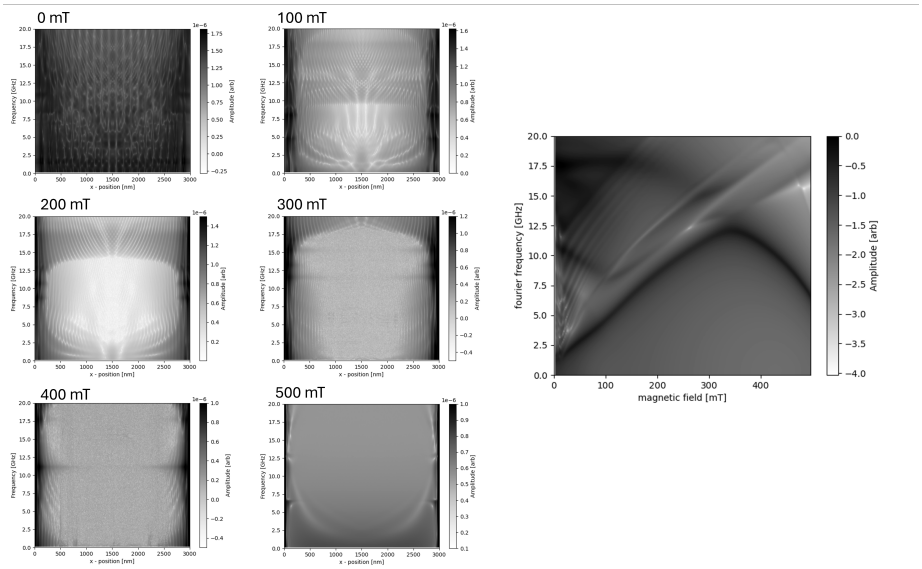


Figure 62: The spatial distribution of the magnon modes across the width of the device. The Amplitude of the edge modes is much greater than the centre modes; however, there are examples of modes that extend into the centre region, such as at 400 mT at 11 GHz. The structure of the modes in the centre of the bar is clearly complex in nature.

is still a complex structure to the central region of the material. The origins of these centre and edge modes are further discussed in the theory Chapter.

Figure 62 shows the spatial distributions for external field values between 0 - 500 mT in 100 mT steps; however, the spatial distributions for the external field values were calculated in 50 mT steps. These extra figures are found in the appendix.

4.4 Classifying the Origin and Type of Magnon Modes Observed Within 3 μm Galfenol Bars

Different magnon modes are possible in magnetic devices, depending on the magnitude and direction of the magnon wavevector with respect to the magnetisation. The main magnon modes to be aware of in the context of this work are the Kittel modes, which have the wavevector, k, equal to 0 [34], Damon-Eshbach (DE) modes, where k is perpendicular to the magnetisation [210] and Backwards Volume (BV) modes for which k is parallel to the magnetisation.

DE modes have their phase and group velocities collinear. The dispersion relation of these modes is given in Chapter 1.4.1, equation 45, as:

$$(\frac{\omega_m}{\omega_M})^2 = (\frac{\omega_H}{\omega_M} + \alpha k_m^2 + 1 + \frac{\lambda_m}{4\pi})(\frac{\omega_H}{\omega_M} + \alpha k_m^2 - \frac{\lambda_m}{4\pi}). \quad m = 1, 2, 3, ... \tag{94}$$

BV modes have a group velocity directed antiparallel to k and the phase velocity. The group velocity opposing the wavevector is why these modes are referred to as backwards. The dispersion relation for these modes is also given in Chapter 1.4.1, equation 49, as:

$$(\frac{\omega}{\omega_M})^2 = (\frac{\omega_H}{\omega_M} + \alpha k^2)(\frac{\omega_H}{\omega_M} + \alpha k^2 + 1 - P(kL)). \tag{95}$$

To further characterise the modes observed in these works, the spatial origins of these modes are explored. To explore this, the shape anisotropy of the sample needs to be factored in due to the cuboidal shape of the bar. The combination of this shape anisotropy and the direction of the applied external field results in an inhomogeneous internal demagnetising field, with the net effective magnetic field approaching 0 closer to the edges of the sample and at the centre being equal in magnitude to the applied external field. Along with this inhomogeneous internal field, there is also pinning of the spins, which occurs at the edges of the sample. The pinning results in the magnetisation at the edges of the sample being perpendicular to the applied field. These two effects, combined, produce two distinct regions where magnons can be excited: the edges and the centre. As the applied field increases, the boundary between these regions is moved closer to the edge as the internal field begins to homogenise. The boundary between these regions arises because the spin waves that could be excited at the boundary are purely imaginary. This results in spin wave wells at the edges and the centre of the sample, where the allowed spin waves must obey

$$\int k(H_{int}(z), \nu)dz = n\pi \quad n \in \mathbb{Z}[66]. \tag{96}$$

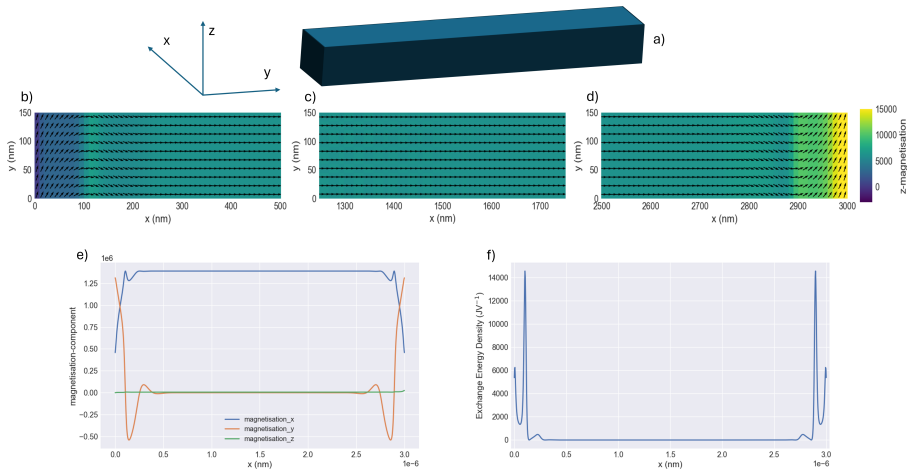


Figure 63: a) A cartoon of the full-size magnetic bar is simulated, with the axes labelled. For b) - d), the magnetisation of the xy plane of the simulated bar is shown; the z height is fixed in the centre of the bar at 18.4 nm. The y-direction has periodic boundary conditions. The colour shows the z component of the magnetisation, whereas the arrows show the x and y components. The external field is 50 mT in the x-direction, such that the edge region has not been too compressed. b) The x-direction is limited to 0 - 500 nm to show the bottom edge of the bar, such that the effects of the edge pinning can be observed. c) The x-direction is limited to 1250 - 1750 nm to show the alignment of the magnetisation in the centre of the bar. d) The x-direction is limited to 2500 - 3000 nm to show the top edge of the bar again, so that the edge pinning can be observed. e) A plot of how the magnetisation component changes throughout the bar. In the centre, the magnetisation is saturated in the direction of the external field, whereas at the edges, there is some rotation in the plane. f) A plot showing how the exchange energy is distributed throughout the bar. This figure clearly shows that the exchange energy is minimised at the centre of the bar, and that the exchange interaction is large at the edges.

Where k(H_{int}(z),ν) is the wavevector as a function of the internal magnetic field and the frequency; this is essentially the dispersion relation. This integral being equal to an integer value of π suggests that each of the excited modes must have nodes at the boundaries.

From works done by Slavin, Bayer and Demokritov [214, 215, 216, 217, 218], it was observed that modes localised at the edges and the centre have different origins, with the modes localised at the edges being due to the exchange interaction more than the dipolar interaction (shown in Figure 63f) and the modes localised in the centre being due more to the dipolar interaction than the exchange interaction. In the simulated results shown in Figure 62, it can be seen that modes with the largest amplitude are localised at the edges of the sample. These results are consistent with those reported by Slavin, Bayer, and Demokritov.

Results from Bayer [68] suggest that the modes confined to the edge regions are DE-type magnons and the modes localised in the central region are BV-type magnons. The type of these modes, however, cannot be directly determined from these results without further measurements using wavevector-dependent techniques.

From the addition and subtraction figures shown in Figures 51 and 54, the dominant effect towards generating the voltage is AMR. This is consistent with the mode being localised at the sample edge, due to the inhomogeneous internal field and edge pinning within this region, which prevents the magnetisation from aligning with the external field. Additionally, in the experimental data shown in Figure 61b), there are instances of crossings occurring from 11.6 - 11.8 GHz and an anticrossing occurring at 10.8 GHz. The modes that produce these crossings and anticrossings are the rising modes, which are observed to cross the falling mode shown in Figure 61a). These modes are more dipolar than exchange, localised in the central region of the bar, and are BV modes. There are differences between the simulated and experimental data, primarily a shift in the frequencies and magnetic fields at which the modes occur, which is likely due to the idealised nature of the simulations. Another difference between the experimental and the simulated data is illustrated by Figure 60, where it's clear that a large number of the magnon modes are not observed in the experimental setup, including the mode at 17.5 GHz and many of the rising modes.

4.5 Conclusion

This experiment explores the electrical excitation and detection of magnons. The experimental results show that the magnon spectrum

is dependent on the orientation of the external magnetic field with respect to the magnetic bar. When the field is oriented at 45° to the bar, a linear mode is observed, whereas when the field is oriented at 90°, a falling magnon mode is observed. This falling magnon mode is also observed to couple to other non-observed magnon modes, with an example of an anticrossing between the falling and unobserved modes. The characterisation of these coupled modes was further explored via simulation, revealing a complex structure of multiple magnon modes localised in different regions of the sample. The boundaries between these regions are produced by the interplay between edge pinning and the effects of shape anisotropy on the demagnetising field.

Through simulations, it was observed that some modes decrease in frequency, then reach an inflexion point at which they increase in frequency as the field increases. Further simulations show that this inflexion point is associated with magnetisation saturation, which occurs more readily in the central region of the bar due to the absence of edge pinning and a more homogeneous demagnetising field. This suggests that modes originating at the centre of the bar have an inflexion point closer to 0 mT. In contrast, the magnetisation, which is confined to the edges and is affected by edge pinning and a more inhomogeneous demagnetising field, produces modes that decrease in frequency up to much higher fields, as the magnetisation is much harder to saturate.

Works from Slavin, Bayer and Demokritov [214, 219, 68] suggest that the edge modes are due to exchange more than dipolar interactions and the central modes are more dipolar than exchange in nature. The work done agrees with this, since the magnetisation in the edge region is perpendicular to the applied field. This is due to edge pinning and the exchange interaction dominating over dipolar interaction, whereas in the central area, the demagnetising field plays a weaker role and allows for the alignment of the magnetisation with the external field. The authors mentioned previously also determined that the edge modes are DE modes and the central modes are BV modes; however, further work is needed to confirm this in the samples used in these works. To experimentally continue the characterisation of these magnon modes, the dynamics and the dispersion relation of these excited magnons should be measured. This is typically done through Brillouin light scattering (BLS) type experiments.

Originally, this experiment was devised to observe strong coupling between magnons and phonons in a microscale device. However, these measurements showed that coupling between the magnon

and phonon systems could not be resolved with this specific device structure and experimental setup. The phonons were shown to be producible (measured via ASOPS) and have frequencies in the range of the magnon measurements, but no coupling was observed. The linewidth of the magnons was found to be approximately 0.5 GHz, and the phonon linewidths were 0.4 GHz for the gratings. This suggests that the magnons were decaying too rapidly to observe any coupling effects between the magnons and phonons. To reduce the linewidths of the excited magnons, different device structures could be explored using waveguide devices commonly employed in the field. This increases the decay rate of the magnons and increases the coupling strength. The generation of the microwave could then be changed to a vector network analyser (VNA), which would allow for the transmission and reflection of the input signal to be measured, which is not possible with the current structure, and would allow for more optimisation of the sample and the device.

5 Conclusion

The three results chapters in this thesis describe three distinct investigations.

The first of these chapters is the observation of a Fano-like interference effect between magnons and phonons. This is explored in a Galfenol nanograting, which is used because Galfenol is a highly magnetostrictive material. The nanograting is designed such that the phonon frequency is tuned by the grating period; the grating also spatially confines phonon modes, thereby increasing the interaction between magnons and phonons, as they are spatially located in the same region. The Galfenol nanograting is excited and probed via a pump-probe laser technique known as ASOPS, which allows the sample to be excited and probed at regular intervals determined by the offset in the repetition rate of the laser pulses. The results of this experiment show that the Fano-like interference is strongly fluence dependent, as when the pump fluence is 1 mJ/cm^2, the Fano-like interference does not appear. The interaction between the magnons and phonons is purely that of two weakly coupled oscillators. When the pump fluence is increased to 10 mJ/cm^2, the Fano-like interference occurs. This is shown via simulations and theoretical analysis to be due to the phase relation between two methods of magnon excitation. The first of these is the ultrafast demagnetisation of the sample via the laser pulse. The second excitation method is spin-transfer torque induced by spin currents. Evidence indicates that this method is caused by an increased concentration of Ga ions in the milled regions of Galfenol, which reduces the material's Curie temperature in these regions; therefore, increasing the pump fluence causes the milled region temperature to exceed the Curie temperature. It is the second excitation method that tunes the overall phase of the magnon excitation and enables the Fano-like interference.

The second Chapter discusses the amplification of the phonon-photon interaction mediated via excitons. This work explores thin flakes of the Van der Waals TMD material WSe_2. These flakes act as acoustic nanocavities for longitudinal phonon modes, where the thickness of the flakes determines the fundamental phonon frequency. In this work, the flakes were again excited and probed via the ASOPS technique. This work shows that the relationship between the refractive index and the photoelastic constant of the material affects the reflectivity of the probe photons, where the refractive index depends on the probe frequency and the photoelastic constant initially only depends on the strain in the flakes, however, close to the direct exciton resonance the photoelastic constant

changes to rely on the photon frequency and the strain. This results in there being two regions of amplified phonon-photon interaction, the first of which is when the fundamental phonon frequency is below 25 GHz, in this region, the Bragg condition can be satisfied and therefore due to the constructive interference of photons reflecting of the top and bottom surfaces of the flakes the sensitivity to the phonon amplitude is increased with further amplification occurring when the probe photon frequency is at the exciton resonance due to the emission of photons from the decay of the excitons at the probe frequency. In the second region, the Bragg condition is not satisfied, and the reflectivity peak arises from the decrease in flake thickness. This reduces the exciton energy level, thereby increasing the number of excited excitons without increasing the pump fluence. The outcome of the peak in reflectivity in this region is that phonons with a fundamental frequency of 100 GHz would have an amplitude of on the order 10^{-4}, and the number density of phonons is 10^4 phonons/μm^2. By reducing the pump fluence, single-phonon detection would be possible by tuning the flake thickness and ensuring the probe frequency is close to the exciton resonance.

The final chapter looks at the electrical excitation of magnons and phonons in a micro-scale bar via a microwave antenna, with detection of the magnon modes via the voltage generated by the inverse spin Hall effect and the anisotropic magnetoresistance. The phonons in this work are spatially confined in two different nanostructures: nanogratings, where the periodicity determines the allowed frequencies, and superlattices, where the period of repeated layers of AlAs/GaAs defines the phonon frequency. In this work, the interaction between phonons and magnons is not resolved. The magnons measured in the samples depend on the orientation of the external magnetic field relative to the fabricated magnetic bar. When the field is applied at 45° to the bar, the observed magnon frequency follows an approximately linear relationship with increasing magnetic field; however, when the magnetic field is applied perpendicular to the bar, the magnon frequency decreases with increasing magnetic field, as well as exhibiting magnon-magnon crossings and anticrossings. The origins of this phenomenon is explored further via simulations, which reveal that, due to the anisotropy and shape of the material, the internal field is inhomogeneous and there is also edge pinning present in the material. The combination of these effects results in two distinct regions in which magnons can be excited. These are the central region and the edge regions. Magnons localised in the edge regions are dominated by the exchange interaction, and magnons localised in the central region are dipolar

dominated. Comparing the simulation results with the experimental results shows that the observed mode is localised at the edge of the bar and therefore exchange-dominant. In contrast, the modes which couple to this edge mode and produce the crossings and anticrossings are localised in the central region of the bar and are dipolar dominant. It is also shown via the experimental results that the origin of the voltage signal induced by the magnons is predominantly via AMR. This further explains why only the edge mode is observed, as in this region, the magnetisation is rotated away from the longitudinal and transverse directions throughout.

This thesis has explored the coupling and detection of magnons, phonons, photons, and excitons confined in nanostructures. These works provide a step toward understanding optimal device structures for on-chip strongly coupled systems, as well as toward exploring other interference-based effects that can be exploited to enhance their detection and applications.

References

[1] Felix Godejohann, Alexey V Scherbakov, Serhii M Kukhtaruk, Alexander N Poddubny, Dmytro D Yaremkevich, Mu Wang, Achim Nadzeyka, Dmitri R Yakovlev, Andrew W Rushforth, Andrey V Akimov, et al. Magnon polaron formed by selectively coupled coherent magnon and phonon modes of a surface patterned ferromagnet. *Physical Review B*, 102(14):144438, 2020.

[2] Stephen Blundell. *Magnetism in Condensed Matter*. Oxford University Press, 10 2001.

[3] Harris VG. *Modern Ferrites: Basic Principles, Processing and Properties, Volume 1*. John Wiley and Sons Ltd, 2022.

[4] JMD Coey and Frédéric Mazaleyrat. History of magnetism. *Reference Module in Materials Science and Materials Engineering*, 2023.

[5] Michael Faraday. *On Induction*. Royal Society, 1838.

[6] William Thomson. Xix. on the electro-dynamic qualities of metals:—effects of magnetization on the electric conductivity of nickel and of iron. *Proceedings of the Royal Society of London*, (8):546–550, 1857.

[7] Edmund C Stoner. Ferromagnetism. *Reports on Progress in Physics*, 11(1):43, 1947.

[8] Pierre Curie. *Propriétés magnétiques des corps a diverses températures*. Number 4. Gauthier-Villars et fils, 1895.

[9] JA Ewing. Magnetic induction in iron and other metals: The electrician, 1892.

[10] Paul Langevin. Sur la théorie du magnétisme. *J. Phys. Theor. Appl.*, 4(1):678–693, 1905.

[11] Pierre Weiss. L'hypothèse du champ moléculaire et la propriété ferromagnétique. *J. Phys. Theor. Appl.*, 6(1):661–690, 1907.

[12] Werner Heisenberg and Wolfgang Pauli. Zur quantendynamik der wellenfelder. *Zeitschrift für Physik*, 56(1):1–61, 1929.

[13] Emil Beck. Zum experimentellen nachweis der ampèreschen molekularströme. *Annalen der Physik*, 365(18):109–148, 1919.

[14] WL Webster. The magnetic properties of iron crystals. *Proceedings of the Royal Society of London. Series A, Containing Papers of a Mathematical and Physical Character*, 107(743):496–509, 1925.

[15] WL Webster. Magneto-striction in iron crystals. *Proceedings of the Royal Society of London. Series A, Containing Papers of a Mathematical and Physical Character*, 109(752):570–584, 1925.

[16] Kotarô Honda, Seisi Kaya, and Yosio Masuyama. On the magnetic properties of single crystals of iron. *Nature*, 117(2952):753–754, 1926.

[17] Mohammed Asadullah Khan, Jian Sun, Bodong Li, Alexander Przybysz, and Jürgen Kosel. Magnetic sensors-a review and recent technologies. *Engineering Research Express*, 3(2):022005, 2021.

[18] R Hunt. A magnetoresistive readout transducer. *IEEE Transactions on Magnetics*, 7(1):150–154, 1971.

[19] Ching Tsang, Tsann Lin, Scott MacDonald, Mustafa Pinarbasi, Neil Robertson, Hugo Santini, Mary Doerner, Tim Reith, Lang Vo, Tom Diola, et al. 5 gb/in/sup 2/recording demonstration with conventional amr dual element heads and thin film disks. *IEEE Transactions on Magnetics*, 33(5):2866–2871, 1997.

[20] SSP Parkin, ZG Li, and David J Smith. Giant magnetoresistance in antiferromagnetic co/cu multilayers. *Applied Physics Letters*, 58(23):2710–2712, 1991.

[21] Stuart Parkin, Xin Jiang, Christian Kaiser, Alex Panchula, Kevin Roche, and Mahesh Samant. Magnetically engineered spintronic sensors and memory. *Proceedings of the IEEE*, 91(5):661–680, 2003.

[22] Michel Julliere. Tunneling between ferromagnetic films. *Physics letters A*, 54(3):225–226, 1975.

[23] Jagadeesh Subbaiah Moodera, Lisa R Kinder, Terrilyn M Wong, and R Meservey. Large magnetoresistance at room temperature in ferromagnetic thin film tunnel junctions. *Physical review letters*, 74(16):3273, 1995.

[24] PP Freitas, R Ferreira, S Cardoso, and F Cardoso. Magnetoresistive sensors. *Journal of Physics: condensed matter*, 19(16):165221, 2007.

[25] Sining Mao, Yonghua Chen, Feng Liu, Xingfu Chen, Bin Xu, Puling Lu, Mohammed Patwari, Haiwen Xi, Clif Chang, Brad Miller, et al. Commercial tmr heads for hard disk drives: characterization and extendibility at 300 gbit 2. *IEEE transactions on magnetics*, 42(2):97–102, 2006.

[26] R Lawrence Comstock. Review modern magnetic materials in data storage. *Journal of Materials Science: Materials in Electronics*, 13:509–523, 2002.

[27] JM Slaughter. Materials for magnetoresistive random access memory. *Annual Review of Materials Research*, 39(1):277–296, 2009.

[28] Werner Heisenberg. Mehrkörperproblem und resonanz in der quantenmechanik. *Zeitschrift für Physik*, 38(6):411–426, 1926.

[29] Ian Duck, Wolfgang Pauli, and ECG Sudarshan. *Pauli and the spin-statistics theorem*. World Scientific, 1997.

[30] John Hasbrouck Van Vleck. *The theory of electric and magnetic susceptibilities*. Oxford University Press, 1932.

[31] Gianfranco Spavieri and Masud Mansuripur. Origin of the spin-orbit interaction. *arXiv preprint arXiv:1506.07239*, 2015.

[32] Timothy Skinner. *Electrical control of spin dynamics in spin-orbit coupled ferromagnets*. PhD thesis, University of Cambridge, 2014.

[33] Llewellyn Hilleth Thomas. I. the kinematics of an electron with an axis. *The London, Edinburgh, and Dublin Philosophical Magazine and Journal of Science*, 3(13):1–22, 1927.

[34] Charles Kittel and Paul McEuen. *Introduction to solid state physics*. John Wiley & Sons, 2018.

[35] MQ Dong, Zhi-Xin Guo, and XR Wang. Anisotropic magnetoresistance due to magnetization-dependent spin-orbit interactions. *Physical Review B*, 108(2):L020401, 2023.

[36] Duncan Parkes. *Strain Control of Ferromagnetic Thin Films and Devices*. PhD thesis, University of Nottingham, 2015.

[37] M. W. Haverkort, I. S. Elfimov, L. H. Tjeng, G. A. Sawatzky, and A. Damascelli. Strong spin-orbit coupling effects on the fermi surface of sr_2ruo_4 and sr_2rho_4. *Phys. Rev. Lett.*, 101:026406, Jul 2008.

[38] Amikam Aharoni. *Introduction to the Theory of Ferromagnetism*, volume 109. Clarendon Press, 2000.

[39] IA Campbell, A Fert, and O Jaoul. The spontaneous resistivity anisotropy in ni-based alloys. *Journal of Physics C: Solid State Physics*, 3(1S):S95, 1970.

[40] AW Rushforth, K Vỳbornỳ, CS King, KW Edmonds, RP Campion, CT Foxon, J Wunderlich, AC Irvine, P Vašek, V Novák, et al. Anisotropic magnetoresistance components in (ga, mn) as. *Physical review letters*, 99(14):147207, 2007.

[41] Syamashree Roy. *The magnetic properties of epitaxial Fe100-xGax thin films: the role of Gallium composition and film thickness*. PhD thesis, University of Nottingham (United Kingdom), 2020.

[42] BD Cullity. *Introduction to Magnetic Materials,(1972)*. New Jersey: Addison-Wiley Publishing Company, 1972.

[43] A E Clark, K B Hathaway, M Wun-Fogle, JB Restorff, Thomas A Lograsso, VM Keppens, G Petculescu, and RA Taylor. Extraordinary magnetoelasticity and lattice softening in bcc fe-ga alloys. *Journal of Applied Physics*, 93(10):8621–8623, 2003.

[44] RC O'Hendley. *Modern magnetic materials*. Principles and Applications (Johns Wiley & Sons, Inc., 2000), 1999.

[45] Alexey V Scherbakov, Alex D Carr, Tetiana L Linnik, Serhii M Kukhtaruk, Andrew D Armour, Achim Nadzeyka, Andrew W Rushforth, Andrey V Akimov, and Manfred Bayer. Hybrid coherent control of magnons in a ferromagnetic phononic resonator excited by laser pulses supplemental material. *Physical Review Research*, 6(1):L012019, 2024.

[46] D Viehland, JieFang Li, Thomas A Lograsso, A Ross, and Manfred Wuttig. Structural studies of fe 0.81 ga 0.19 by reciprocal space mapping. *Applied physics letters*, 81(17):3185–3187, 2002.

[47] Hu Cao, Peter M Gehring, Christopher P Devreugd, JA Rodriguez-Rivera, J Li, and D Viehland. Role of nanoscale precipitates on the enhanced magnetostriction¡? format?¿ of heat-treated galfenol (fe 1-x ga x) alloys. *Physical review letters*, 102(12):127201, 2009.

[48] Mark Laver, C Mudivarthi, JR Cullen, AB Flatau, W-C Chen, SM Watson, and M Wuttig. Magnetostriction and magnetic heterogeneities in iron-gallium. *Physical review letters*, 105(2):027202, 2010.

[49] Yubin Ke, C Jiang, Juzhou Tao, and Huiping Duan. Local inhomogeneous structural origin of giant magnetostriction in fe-ga alloys. *Journal of Alloys and Compounds*, 725:14–22, 2017.

[50] Somnath Bhattacharyya, J. R. Jinschek, A. Khachaturyan, H. Cao, J. F. Li, and D. Viehland. Nanodispersed Do_3-phase nanostructures observed in magnetostrictive fe–19 *Phys. Rev. B*, 77:104107, Mar 2008.

[51] G Petculescu, KB Hathaway, Thomas A Lograsso, M Wun-Fogle, and AE Clark. Magnetic field dependence of galfenol elastic properties. *Journal of Applied Physics*, 97(10), 2005.

[52] Igor S Golovin, Valeria Palacheva, A Mohamed, Anatoliy Balagurov, Ivan Bobrikov, Natalia Samoylova, and Sergei Sumnikov. Phase transitions in metastable fe–ga alloys. In *SENSORDEVICES 2019, The Tenth International Conference on Sensor Device Technologies and Applications*, pages 13–16, 2019.

[53] Richard M Bozorth. *Concepts of ferromagnetism*. Wiley-IEEE Press, 1978.

[54] Sadamichi Maekawa, Takashi Kikkawa, Hiroyuki Chudo, Jun'ichi Ieda, and Eiji Saitoh. Spin and spin current—from fundamentals to recent progress. *Journal of Applied Physics*, 133(2), 2023.

[55] Mikhail I Dyakonov and VI Perel. Current-induced spin orientation of electrons in semiconductors. *Physics Letters A*, 35(6):459–460, 1971.

[56] RV Shchelushkin and Arne Brataas. Spin hall effects in diffusive normal metals. *Physical Review B—Condensed Matter and Materials Physics*, 71(4):045123, 2005.

[57] Hans-Andreas Engel, Bertrand I Halperin, and Emmanuel I Rashba. Theory of spin hall conductivity in n-doped gaas. *Physical review letters*, 95(16):166605, 2005.

[58] Guang-Yu Guo, Shuichi Murakami, T-W Chen, and Naoto Nagaosa. Intrinsic spin hall effect in platinum: First-principles calculations. *Physical review letters*, 100(9):096401, 2008.

[59] Shuichi Murakami, Naoto Nagaosa, and Shou-Cheng Zhang. Dissipationless quantum spin current at room temperature. *Science*, 301(5638):1348–1351, 2003.

[60] Jairo Sinova, Dimitrie Culcer, Qian Niu, NA Sinitsyn, T Jungwirth, and Allan H MacDonald. Universal intrinsic spin hall effect. *Physical review letters*, 92(12):126603, 2004.

[61] Anatoly Konstantinovich Zvezdin and Viacheslav Alekseevich Kotov. *Modern magnetooptics and magnetooptical materials*. CRC Press, 1997.

[62] Eugene Hecht. *Optik*. Walter de Gruyter GmbH & Co KG, 2023.

[63] John Kerr. Xliii. on rotation of the plane of polarization by reflection from the pole of a magnet. *The London, Edinburgh, and Dublin Philosophical Magazine and Journal of Science*, 3(19):321–343, 1877.

[64] Thomas L Gilbert. A lagrangian formulation of the gyromagnetic equation of the magnetization field. *Phys. Rev.*, 100:1243, 1955.

[65] Marijan Beg, Martin Lang, and Hans Fangohr. Ubermag: Towards more effective micromagnetic workflows. *IEEE Transactions on Magnetics*, 58(2):1–5, 2022.

[66] Burkard Hillebrands and Kamel Ounadjela. *Spin dynamics in confined magnetic structures III*, volume 83. Springer Science & Business Media, 2003.

[67] Burkard Hillebrands and Kamel Ounadjela. *Spin dynamics in confined magnetic structures I*, volume 83. Springer Science & Business Media, 2003.

[68] C Bayer, JP Park, H Wang, M Yan, CE Campbell, and PA Crowell. Spin waves in an inhomogeneously magnetized stripe. *Physical Review B*, 69(13):134401, 2004.

[69] J Jorzick, SO Demokritov, B Hillebrands, M Bailleul, C Fermon, K Yu Guslienko, AN Slavin, DV Berkov, and NL Gorn. Spin wave wells in nonellipsoidal micrometer size magnetic elements. *Physical Review Letters*, 88(4):047204, 2002.

[70] AV Chumak, AA Serga, and B Hillebrands. Magnonic crystals for data processing. *Journal of Physics D: Applied Physics*, 50(24):244001, 2017.

[71] Roman Verba, Gennadiy Melkov, Vasil Tiberkevich, and Andrei Slavin. Collective spin-wave excitations in a two-dimensional array of coupled magnetic nanodots. *Physical Review B—Condensed Matter and Materials Physics*, 85(1):014427, 2012.

[72] Silvia Tacchi, Gianluca Gubbiotti, Marco Madami, and Giovanni Carlotti. Brillouin light scattering studies of 2d magnonic crystals. *Journal of Physics: Condensed Matter*, 29(7):073001, 2016.

[73] SA Nikitov, Ph Tailhades, and CS Tsai. Spin waves in periodic magnetic structures—magnonic crystals. *Journal of Magnetism and Magnetic Materials*, 236(3):320–330, 2001.

[74] Thomas Schneider, Alexander A Serga, Britta Leven, Burkard Hillebrands, Robert L Stamps, and Mikhail P Kostylev. Realization of spin-wave logic gates. *Applied Physics Letters*, 92(2), 2008.

[75] Alexander Khitun. Multi-frequency magnonic logic circuits for parallel data processing. *Journal of Applied Physics*, 111(5), 2012.

[76] Andrey A Nikitin, Alexey B Ustinov, Alexander A Semenov, Andrii V Chumak, Alexander A Serga, Vitaliy I Vasyuchka, Erkki Lähderanta, Boris A Kalinikos, and Burkard Hillebrands. A spin-wave logic gate based on a width-modulated dynamic magnonic crystal. *Applied Physics Letters*, 106(10), 2015.

[77] Alexander Khitun and Kang L Wang. Non-volatile magnonic logic circuits engineering. *Journal of Applied Physics*, 110(3), 2011.

[78] Andrii V Chumak, Alexander A Serga, and Burkard Hillebrands. Magnon transistor for all-magnon data processing. *Nature communications*, 5(1):4700, 2014.

[79] Frederick Gertz, Alexander Kozhevnikov, Yuri Filimonov, and Alexander Khitun. Magnonic holographic memory. *IEEE Transactions on Magnetics*, 51(4):1–5, 2014.

[80] Pierre Deymier and Keith Runge. One-dimensional mass-spring chains supporting elastic waves with non-conventional topology. *Crystals*, 6(4):44, 2016.

[81] Arthur A Oliner. Acoustic surface waves. *Berlin and New York*, 24, 1978.

[82] Karlheinz Seeger. *Semiconductor physics*. Springer Science & Business Media, 2013.

[83] John H Davies. *The physics of low-dimensional semiconductors: an introduction*. Cambridge university press, 1998.

[84] John Singleton. *Band theory and electronic properties of solids*, volume 2. OUP Oxford, 2001.

[85] Daniele Guerci, Massimo Capone, and Michele Fabrizio. Exciton mott transition revisited. *Physical Review Materials*, 3(5):054605, 2019.

[86] Andrey E Miroshnichenko, Sergej Flach, and Yuri S Kivshar. Fano resonances in nanoscale structures. *Reviews of Modern Physics*, 82(3):2257–2298, 2010.

[87] Ugo Fano. Effects of configuration interaction on intensities and phase shifts. *Physical review*, 124(6):1866, 1961.

[88] Yong S Joe, Arkady M Satanin, and Chang Sub Kim. Classical analogy of fano resonances. *Physica Scripta*, 74(2):259, 2006.

[89] Albrecht Bartels, Roland Cerna, Caroline Kistner, Arne Thoma, Florian Hudert, Christof Janke, and Thomas Dekorsy. Ultrafast time-domain spectroscopy based on high-speed asynchronous optical sampling. *Review of Scientific Instruments*, 78(3), 2007.

[90] R Weber. Magnon-phonon coupling in metallic films. *Physical Review*, 169(2):451, 1968.

[91] Cassidy Berk, Mike Jaris, Weigang Yang, Scott Dhuey, Stefano Cabrini, and Holger Schmidt. Strongly coupled magnon–phonon dynamics in a single nanomagnet. *Nature communications*, 10(1):2652, 2019.

[92] Sujung Kim, Becker Sharif, Scott Dhuey, Thomas David Yuzvinsky, Weigang Yang, David Lederman, and Holger Schmidt. Engineering strong magnon–phonon coupling in single cofe nanomagnets. *Journal of Applied Physics*, 137(12), 2025.

[93] Zhen Shen, Guan-Ting Xu, Mai Zhang, Yan-Lei Zhang, Yu Wang, Cheng-Zhe Chai, Chang-Ling Zou, Guang-Can Guo, and Chun-Hua Dong. Coherent coupling between phonons, magnons, and photons. *Physical Review Letters*, 129(24):243601, 2022.

[94] Rui-Chang Shen, Jie Li, Yi-Ming Sun, Wei-Jiang Wu, Xuan Zuo, Yi-Pu Wang, Shi-Yao Zhu, and JQ You. Cavity-magnon polaritons strongly coupled to phonons. *Nature Communications*, 16(1):5652, 2025.

[95] JA Haigh, NJ Lambert, AC Doherty, and AJ Ferguson. Dispersive readout of ferromagnetic resonance for strongly coupled magnons and microwave photons. *Physical Review B*, 91(10):104410, 2015.

[96] Yi Li, Tomas Polakovic, Yong-Lei Wang, Jing Xu, Sergi Lendinez, Zhizhi Zhang, Junjia Ding, Trupti Khaire, Hilal Saglam, Ralu Divan, et al. Strong coupling between magnons and microwave photons in on-chip ferromagnet-superconductor thin-film devices. *Physical review letters*, 123(10):107701, 2019.

[97] IW Haygood, MR Pufall, ERJ Edwards, Justin M Shaw, and WH Rippard. Strong coupling of an fe-co alloy with ultralow damping to superconducting co-planar waveguide resonators. *Physical Review Applied*, 15(5):054021, 2021.

[98] IA Golovchanskiy, NN Abramov, VS Stolyarov, AA Golubov, M Yu Kupriyanov, VV Ryazanov, and AV Ustinov. Approaching deep-strong on-chip photon-to-magnon coupling. *Physical Review Applied*, 16(3):034029, 2021.

[99] Igor A Golovchanskiy, Nikolay N Abramov, Vasily S Stolyarov, Martin Weides, Valery V Ryazanov, Alexander A Golubov, Alexey V Ustinov, and Mikhail Yu Kupriyanov. Ultrastrong photon-to-magnon coupling in multilayered heterostructures involving superconducting coherence via ferromagnetic layers. *Science advances*, 7(25):eabe8638, 2021.

[100] Kaiman Lin, Xiaoxiao Sun, Florian Dirnberger, Yi Li, Jiang Qu, Peiting Wen, Zdenek Sofer, Aljoscha Soll, Stephan Winnerl, Manfred Helm, et al. Strong exciton–phonon coupling as a fingerprint of magnetic ordering in van der waals layered crsbr. *ACS nano*, 18(4):2898–2905, 2024.

[101] Limeng Ni, Uyen Huynh, Alexandre Cheminal, Tudor H Thomas, Ravichandran Shivanna, Ture F Hinrichsen, Shahab Ahmad, Aditya Sadhanala, and Akshay Rao. Real-time observation of exciton–phonon coupling dynamics in self-assembled hybrid perovskite quantum wells. *ACS nano*, 11(11):10834–10843, 2017.

[102] Alexey V Scherbakov, Alex D Carr, Tetiana L Linnik, Serhii M Kukhtaruk, Andrew D Armour, Achim Nadzeyka, Andrew W Rushforth, Andrey V Akimov, and Manfred Bayer. Hybrid coherent control of magnons in a ferromagnetic phononic resonator excited by laser pulses. *Physical Review Research*, 6(1):L012019, 2024.

[103] Chong Chen, Mingyuan Ma, Weiqi Du, Zheng Sun, Deqi Tao, Lei Han, Sulei Fu, Feng Pan, and Cheng Song. Highly sensitive surface acoustic wave magnetic field sensor based on a strongly coupled magnon-phonon system. *Advanced Functional Materials*, page e18999, 2025.

[104] Yunyoung Hwang, Liyang Liao, Jorge Puebla, Marco Brühlmann, Carlos Gonzalez-Ballestero, Kouta Kondou, Naoki Ogawa, Sadamichi Maekawa, and Yoshichika Otani. Harmonic and subharmonic magnon generation in a surface acoustic wave resonator. *arXiv preprint arXiv:2509.19706*, 2025.

[105] Dipankar Jana, Diana Vaclavkova, Rajesh Kumar Ulaganathan, Raman Sankar, Milan Orlita, Clement Faugeras, Maciej Koperski, ME Zhitomirsky, and Marek Potemski. Strong and selective magnon-phonon coupling in van der waals antiferromagnet cops _3. *arXiv preprint arXiv:2508.07412*, 2025.

[106] Daiki Hatanaka, Motoki Asano, Megumi Kurosu, Yoshitaka Taniyasu, Hajime Okamoto, and Hiroshi Yamaguchi. On-chip magnon polaron generation in mode-matched cavity magnomechanics. *arXiv preprint arXiv:2507.03577*, 2025.

[107] NL Kazanskiy, SN Khonina, and Muhammad Ali Butt. Plasmonic sensors based on metal-insulator-metal waveguides for refractive index sensing applications: A brief review. *Physica E: Low-dimensional systems and nanostructures*, 117:113798, 2020.

[108] Bin Ai, Chunyuan Song, Layne Bradley, and Yiping Zhao. Strong fano resonance excited in an array of nanoparticle-in-ring nanostructures for dual plasmonic sensor applications. *The Journal of Physical Chemistry C*, 122(36):20935–20944, 2018.

[109] Ajuan Cui, Zhe Liu, Jiafang Li, Tiehan H Shen, Xiaoxiang Xia, Zhiyuan Li, Zhijie Gong, Hongqiang Li, Benli Wang, Junjie Li, et al. Directly patterned substrate-free plasmonic "nanograter" structures with unusual fano resonances. *Light: Science & Applications*, 4(7):e308–e308, 2015.

[110] Yun Binfeng, Zhang Ruohu, Hu Guohua, and Cui Yiping. Ultra sharp fano resonances induced by coupling between plasmonic stub and circular cavity resonators. *Plasmonics*, 11(4):1157–1162, 2016.

[111] GuiQian Lin, Hui Yang, Yan Deng, Dandan Wu, Xuan Zhou, Yunwen Wu, Guangtao Cao, Jian Chen, Wanmei Sun, and Renlong Zhou. Ultra-compact high-sensitivity plasmonic sensor based on fano resonance with symmetry breaking ring cavity. *Optics express*, 27(23):33359–33368, 2019.

[112] Chia-Ming Chang and Olav Solgaard. Fano resonances in integrated silicon bragg reflectors for sensing applications. *Optics express*, 21(22):27209–27218, 2013.

[113] Jiawei Wang, Xiaobei Zhang, Ming Yan, Lei Yang, Fengyu Hou, Wen Sun, Xiaotong Zhang, Libo Yuan, Hai Xiao, and Tingyun Wang. Embedded whispering-gallery mode microsphere resonator in a tapered hollow annular core fiber. *Photonics Research*, 6(12):1124–1129, 2018.

[114] Ferenc Krausz and Mark I Stockman. Attosecond metrology: from electron capture to future signal processing. *Nature Photonics*, 8(3):205–213, 2014.

[115] Xiaodong Yang, Mingbin Yu, Dim-Lee Kwong, and Chee Wei Wong. All-optical analog to electromagnetically induced

transparency¡? format?¿ in multiple coupled photonic crystal cavities. *Physical review letters*, 102(17):173902, 2009.

[116] Nikhil Pramanik, Krishna Chaitanya Yellapragada, Suneel Singh, and P Anantha Lakshmi. Coherent control of fano resonances in a macroscopic four-mirror cavity. *Physical Review A*, 101(4):043802, 2020.

[117] GD Fuchs, VV Dobrovitski, DM Toyli, FJ Heremans, CD Weis, Thomas Schenkel, and DD Awschalom. Excited-state spin coherence of a single nitrogen–vacancy centre in diamond. *Nature Physics*, 6(9):668–672, 2010.

[118] ER MacQuarrie, TA Gosavi, NR Jungwirth, SA Bhave, and GD Fuchs. Mechanical spin control of nitrogen-vacancy centers in diamond. *Physical review letters*, 111(22):227602, 2013.

[119] VV Belykh, AR Korotneva, and DR Yakovlev. Stimulated resonant spin amplification reveals millisecond electron spin coherence time of rare-earth ions in solids. *Physical Review Letters*, 127(15):157401, 2021.

[120] Xufeng Zhang, Chang-Ling Zou, Liang Jiang, and Hong X Tang. Cavity magnomechanics. *Science advances*, 2(3):e1501286, 2016.

[121] Xufeng Zhang, Chang-Ling Zou, Liang Jiang, and Hong X Tang. Strongly coupled magnons and cavity microwave photons. *Physical review letters*, 113(15):156401, 2014.

[122] Nicolò Crescini, C Braggio, G Carugno, R Di Vora, A Ortolan, and G Ruoso. Magnon-driven dynamics of a hybrid system excited with ultrafast optical pulses. *Communications Physics*, 3(1):164, 2020.

[123] AJ Schellekens, KC Kuiper, RRJC De Wit, and B Koopmans. Ultrafast spin-transfer torque driven by femtosecond pulsed-laser excitation. *Nature communications*, 5(1):4333, 2014.

[124] Ran Cheng, Di Xiao, and Arne Brataas. Terahertz antiferromagnetic spin hall nano-oscillator. *Physical review letters*, 116(20):207603, 2016.

[125] JR Hortensius, D Afanasiev, M Matthiesen, R Leenders, R Citro, AV Kimel, RV Mikhaylovskiy, BA Ivanov, and AD Caviglia. Coherent spin-wave transport in an antiferromagnet. *Nature physics*, 17(9):1001–1006, 2021.

[126] Peng Peng, Yonghao Mi, Marianna Lytova, Mathew Britton, Xiaoyan Ding, A Yu Naumov, PB Corkum, and DM Villeneuve. Coherent control of ultrafast extreme ultraviolet transient absorption. *Nature Photonics*, 16(1):45–51, 2022.

[127] Mikhail F Limonov. Fano resonance for applications. *Advances in optics and photonics*, 13(3):703–771, 2021.

[128] Felix Godejohann. *Strong magnon-phonon coupling in a ferromagnetic nanograting*. PhD thesis, Dissertation, Dortmund, Technische Universität, 2020, 2020.

[129] Marc J Madou. *Fundamentals of microfabrication and nanotechnology, three-volume set*. CRC Press, 2018.

[130] A Guillén-Cervantes, Z Rivera-Alvarez, M López-López, E López-Luna, and I Hernández-Calderón. Gaas surface oxide desorption by annealing in ultra high vacuum. *Thin Solid Films*, 373(1-2):159–163, 2000.

[131] DE Parkes, LR Shelford, P Wadley, V Holỳ, M Wang, AT Hindmarch, G Van Der Laan, RP Campion, KW Edmonds, SA Cavill, et al. Magnetostrictive thin films for microwave spintronics. *Scientific reports*, 3(1):2220, 2013.

[132] SR Bowe. *Magnetisation dynamics in magnetostrictive nanostructures*. PhD thesis, University of Nottingham, 2017.

[133] Alisha Prasad, Junseo Choi, Zheng Jia, Sunggook Park, and Manas Ranjan Gartia. Nanohole array plasmonic biosensors: Emerging point-of-care applications. *Biosensors and Bioelectronics*, 130:185–203, 2019.

[134] Raith. Raith fib-sem velion.

[135] JK Chen, DY Tzou, and JE Beraun. A semiclassical two-temperature model for ultrafast laser heating. *International journal of heat and mass transfer*, 49(1-2):307–316, 2006.

[136] SA Turnage, JP Ligda, JU Cazamias, and CL Williams. The spall and anomalous inelastic response of galfenol to shock loading. *Journal of Applied Physics*, 131(12), 2022.

[137] Otfried Madelung. *Semiconductors: data handbook*. Springer Science & Business Media, 2004.

[138] COMSOL. Comsol multiphysics® v. 6.3.

[139] SM Kukhtaruk, AW Rushforth, F Godejohann, AV Scherbakov, and M Bayer. Transition magnon modes in thin ferromagnetic nanogratings. *Physical Review B*, 106(6):064411, 2022.

[140] DE Parkes, SA Cavill, AT Hindmarch, P Wadley, F McGee, CR Staddon, KW Edmonds, RP Campion, BL Gallagher, and AW Rushforth. Non-volatile voltage control of magnetization and magnetic domain walls in magnetostrictive epitaxial thin films. *Applied Physics Letters*, 101(7), 2012.

[141] JB Restorff, M Wun-Fogle, KB Hathaway, AE Clark, Thomas A Lograsso, and G Petculescu. Tetragonal magnetostriction and magnetoelastic coupling in FeAl, FeGa, FeGe, FeSi, FeGaAl, and FeGaGe alloys. *Journal of Applied Physics*, 111(2), 2012.

[142] Arthur E Clark, Marilyn Wun-Fogle, James B Restorff, and Thomas A Lograsso. Magnetostrictive properties of galfenol alloys under compressive stress. *Materials transactions*, 43(5):881–886, 2002.

[143] Christopher D Woodgate. Compositional order and subsequent magnetostriction in Fe 1-x Ga x (galfenol). In *Modelling Atomic Arrangements in Multicomponent Alloys: A Perturbative, First-Principles-Based Approach*, pages 155–169. Springer, 2024.

[144] Gregory Malinowski, F Dalla Longa, JHH Rietjens, PV Paluskar, R Huijink, HJM Swagten, and B Koopmans. Control of speed and efficiency of ultrafast demagnetization by direct transfer of spin angular momentum. *Nature Physics*, 4(11):855–858, 2008.

[145] Dennis Rudolf, Chan La-O-Vorakiat, Marco Battiato, Roman Adam, Justin M Shaw, Emrah Turgut, Pablo Maldonado, Stefan Mathias, Patrik Grychtol, Hans T Nembach, et al. Ultrafast magnetization enhancement in metallic multilayers driven by superdiffusive spin current. *Nature communications*, 3(1):1037, 2012.

[146] Gyung-Min Choi, Byoung-Chul Min, Kyung-Jin Lee, and David G Cahill. Spin current generated by thermally driven ultrafast demagnetization. *Nature communications*, 5(1):4334, 2014.

[147] Ilya Razdolski, Alexandr Alekhin, Nikita Ilin, Jan P Meyburg, Vladimir Roddatis, Detlef Diesing, Uwe Bovensiepen, and Alexey Melnikov. Nanoscale interface confinement of ultrafast spin transfer torque driving non-uniform spin dynamics. *Nature communications*, 8(1):15007, 2017.

[148] Quentin Remy, Julius Hohlfeld, Maxime Vergès, Yann Le Guen, Jon Gorchon, Grégory Malinowski, Stéphane Mangin, and Michel Hehn. Accelerating ultrafast magnetization reversal by non-local spin transfer. *Nature Communications*, 14(1):445, 2023.

[149] Junta Igarashi, Wei Zhang, Quentin Remy, Eva Díaz, Jun-Xiao Lin, Julius Hohlfeld, Michel Hehn, Stéphane Mangin, Jon Gorchon, and Grégory Malinowski. Optically induced ultrafast magnetization switching in ferromagnetic spin valves. *Nature Materials*, 22(6):725–730, 2023.

[150] Henning Ulrichs and Ilya Razdolski. Micromagnetic view on ultrafast magnon generation by femtosecond spin current pulses. *Physical Review B*, 98(5):054429, 2018.

[151] TL Linnik, AV Scherbakov, DR Yakovlev, X Liu, JK Furdyna, and M Bayer. Theory of magnetization precession induced by a picosecond strain pulse in ferromagnetic semiconductor (ga, mn) as. *Physical Review B—Condensed Matter and Materials Physics*, 84(21):214432, 2011.

[152] VN Kats, TL Linnik, AS Salasyuk, AW Rushforth, M Wang, P Wadley, Andrey V Akimov, SA Cavill, V Holy, AM Kalashnikova, et al. Ultrafast changes of magnetic anisotropy driven by laser-generated coherent and noncoherent phonons in metallic films. *Physical Review B*, 93(21):214422, 2016.

[153] V Besse, AV Golov, VS Vlasov, A Alekhin, D Kuzmin, IV Bychkov, LN Kotov, and VV Temnov. Generation of exchange magnons in thin ferromagnetic films by ultrashort acoustic pulses. *Journal of Magnetism and Magnetic Materials*, 502:166320, 2020.

[154] AV Scherbakov, AP Danilov, F Godejohann, TL Linnik, BA Glavin, LA Shelukhin, DP Pattnaik, M Wang, AW Rushforth, DR Yakovlev, et al. Optical excitation of single- and multimode magnetization precession in fe-ga nanolayers. *Physical Review Applied*, 11(3):031003, 2019.

[155] Claas Abert, Hossein Sepehri-Amin, Florian Bruckner, Christoph Vogler, Masamitsu Hayashi, and Dieter Suess. Fieldlike and dampinglike spin-transfer torque in magnetic multilayers. *Physical Review Applied*, 7(5):054007, 2017.

[156] AE Clark, M Wun-Fogle, JB Restorff, Kevin W Dennis, Thomas A Lograsso, and R William McCallum. Temperature dependence of the magnetic anisotropy and magnetostriction of fe100- xgax (x= 8.6, 16.6, 28.5). *Journal of Applied Physics*, 97(10), 2005.

[157] Carmine Vittoria. *Microwave properties of magnetic films*. World Scientific, 1993.

[158] Alex D Carr, Claudia Ruppert, Anton K Samusev, Giulia Magnabosco, Nicolas Vogel, Tetiana L Linnik, Andrew W Rushforth, Manfred Bayer, Alexey V Scherbakov, and Andrey V Akimov. Enhanced photon–phonon interaction in wse2 acoustic nanocavities. *ACS photonics*, 11(3):1147–1155, 2024.

[159] J Pouzet, JC Bernede, A Khellil, H Essaidi, and S Benhida. Preparation and characterization of tungsten diselenide thin films. *Thin Solid Films*, 208(2):252–259, 1992.

[160] Won Seok Yun, S. W. Han, Soon Cheol Hong, In Gee Kim, and J. D. Lee. Thickness and strain effects on electronic structures of transition metal dichalcogenides: 2h-mX_2 semiconductors (m = mo, w; x = s, se, te). *Phys. Rev. B*, 85:033305, Jan 2012.

[161] Refractive index database. `https://refractiveindex.info/?shelf=main&book=WSe2&page=Munkhbat-o`. Accessed: 02-04-2025.

[162] EM Ganapol'skii and DN Makovetskii. Generation of coherent phonons in ruby. *Solid state communications*, 15(8):1249–1252, 1974.

[163] Wenjing Yan, Andrey V Akimov, María Barra-Burillo, Manfred Bayer, Jonathan Bradford, Vitalyi E Gusev, Luis E Hueso, Anthony Kent, Serhii Kukhtaruk, Achim Nadzeyka, et al. Coherent phononics of van der waals layers on nanogratings. *Nano Letters*, 22(16):6509–6515, 2022.

[164] Qing Hu, Benjamin S Williams, Sushil Kumar, Hans Callebaut, Stephen Kohen, and John L Reno. Resonant-phonon-assisted thz quantum-cascade lasers with metal–metal waveguides. *Semiconductor science and technology*, 20(7):S228, 2005.

[165] Shang-En Wu, S Dhara, Tao-Hung Hsueh, Yi-Feng Lai, Cheng-Yu Wang, and Chuan-Pu Liu. Surface optical phonon modes in ternary aligned crystalline ingan/gan multi-quantum-well nanopillar arrays. *Journal of Raman Spectroscopy: An International Journal for Original Work in all Aspects of Raman Spectroscopy, Including Higher Order Processes, and also Brillouin and Rayleigh Scattering*, 40(12):2044–2049, 2009.

[166] M Trigo, A Bruchhausen, A Fainstein, Bernard Jusserand, and V Thierry-Mieg. Confinement of acoustical vibrations in a semiconductor planar phonon cavity. *Physical review letters*, 89(22):227402, 2002.

[167] Agnès Huynh, ND Lanzillotti-Kimura, Bernard Jusserand, Bernard Perrin, A Fainstein, ¡? format?¿ MF Pascual-Winter, Emmanuel Peronne, and A Lemaître. Subterahertz phonon dynamics in acoustic nanocavities. *Physical review letters*, 97(11):115502, 2006.

[168] Axel Bruchhausen, Raphael Gebs, Florian Hudert, Daniel Issenmann, Gregor Klatt, Albrecht Bartels, Olivier Schecker, Reimar Waitz, Artur Erbe, Elke Scheer, et al. Subharmonic resonant optical excitation of confined acoustic modes in a free-standing semiconductor membrane at ghz frequencies with a high-repetition-rate femtosecond laser. *Physical review letters*, 106(7):077401, 2011.

[169] John Cuffe, Oliver Ristow, Emigdio Chávez, Andrey Shchepetov, Pierre-Olivier Chapuis, Francesc Alzina, Mike Hettich, Mika Prunnila, Jouni Ahopelto, Thomas Dekorsy, et al. Lifetimes of confined acoustic phonons in ultrathin silicon membranes. *Physical review letters*, 110(9):095503, 2013.

[170] Chuan He, Oliver Ristow, Martin Grossmann, Delia Brick, Yuning Guo, Martin Schubert, Mike Hettich, Vitalyi Gusev, and Thomas Dekorsy. Acoustic waves undetectable by transient reflectivity measurements. *Physical Review B*, 95(18):184302, 2017.

[171] Clemens CW Ruppel. Acoustic wave filter technology–a review. *IEEE transactions on ultrasonics, ferroelectrics, and frequency control*, 64(9):1390–1400, 2017.

[172] Lei Wan, Zhiqiang Yang, Wenfeng Zhou, Meixun Wen, Tianhua Feng, Siqing Zeng, Dong Liu, Huan Li, Jingshun Pan, Ning Zhu, et al. Highly efficient acousto-optic modulation using nonsuspended thin-film lithium niobate-chalcogenide hybrid waveguides. *Light: Science & Applications*, 11(1):145, 2022.

[173] Julien Chaste, A Eichler, J Moser, G Ceballos, R Rurali, and A Bachtold. A nanomechanical mass sensor with yoctogram resolution. *Nature nanotechnology*, 7(5):301–304, 2012.

[174] Markus Aspelmeyer, Tobias J Kippenberg, and Florian Marquardt. Cavity optomechanics. *Reviews of Modern Physics*, 86(4):1391–1452, 2014.

[175] Yiwen Chu, Prashanta Kharel, William H Renninger, Luke D Burkhart, Luigi Frunzio, Peter T Rakich, and Robert J Schoelkopf. Quantum acoustics with superconducting qubits. *Science*, 358(6360):199–202, 2017.

[176] Hong Qiao, Étienne Dumur, Gustav Andersson, Haoxiong Yan, M-H Chou, Joel Grebel, Christopher R Conner, Yash J Joshi, Jacob M Miller, Rhys G Povey, et al. Splitting phonons: Building a platform for linear mechanical quantum computing. *Science*, 380(6649):1030–1033, 2023.

[177] Aaron D O'Connell, Max Hofheinz, Markus Ansmann, Radoslaw C Bialczak, Mike Lenander, Erik Lucero, Matthew Neeley, Daniel Sank, H Wang, Martin Weides, et al. Quantum ground state and single-phonon control of a mechanical resonator. *Nature*, 464(7289):697–703, 2010.

[178] Immo Söllner, Leonardo Midolo, and Peter Lodahl. Deterministic single-phonon source triggered by a single photon. *Physical review letters*, 116(23):234301, 2016.

[179] Davide Boschetto, Leandro Malard, Chun Hung Lui, Kin Fai Mak, Zhiqiang Li, Hugen Yan, and Tony F Heinz. Real-time observation of interlayer vibrations in bilayer and few-layer graphene. *Nano letters*, 13(10):4620–4623, 2013.

[180] Changxiu Li, Alexey V Scherbakov, Pedro Soubelet, Anton K Samusev, Claudia Ruppert, Nilanthy Balakrishnan, Vitalyi E Gusev, Andreas V Stier, Jonathan J Finley, Manfred Bayer, et al. Coherent phonons in van der waals mose2/wse2 heterobilayers. *Nano Letters*, 23(17):8186–8193, 2023.

[181] Pedro Soubelet, Andrés A Reynoso, Alejandro Fainstein, Karol Nogajewski, Marek Potemski, Clément Faugeras, and Axel E Bruchhausen. The lifetime of interlayer breathing modes of few-layer 2h-mose 2 membranes. *Nanoscale*, 11(21):10446–10453, 2019.

[182] Maxim K Zalalutdinov, Jeremy T Robinson, Jose J Fonseca, Samuel W LaGasse, Tribhuwan Pandey, Lucas R Lindsay, Thomas L Reinecke, Douglas M Photiadis, James C Culbertson, Cory D Cress, et al. Acoustic cavities in 2d heterostructures. *Nature communications*, 12(1):3267, 2021.

[183] Andrey Yu Klokov, Nikolay Yu Frolov, Andrey I Sharkov, Sergey N Nikolaev, Maxim A Chernopitssky, Semen I Chentsov, Mikhail V Pugachev, Aliaksandr I Duleba, Alexey V Shupletsov, Vladimir S Krivobok, et al. 3d hypersound microscopy of van der waals heterostructures. *Nano Letters*, 22(5):2070–2076, 2022.

[184] Jake DG Greener, Andrey V Akimov, VE Gusev, ZR Kudrynskyi, Peter H Beton, Zakhar D Kovalyuk, Takashi Taniguchi, Kenji Watanabe, AJ Kent, and Amalia Patanè. Coherent acoustic phonons in van der waals nanolayers and heterostructures. *Physical Review B*, 98(7):075408, 2018.

[185] Wenjing Yan, Andrey V Akimov, Joseph A Page, Mark T Greenaway, Alexander G Balanov, Amalia Patanè, and Anthony J Kent. Nondestructive picosecond ultrasonic probing of intralayer and van der waals interlayer bonding in α-and β-in2se3. *Advanced Functional Materials*, 31(50):2106206, 2021.

[186] Yiyu Xia, Zhongdong Han, Kenji Watanabe, Takashi Taniguchi, Jie Shan, and Kin Fai Mak. Superconductivity in twisted bilayer wse2. *Nature*, 637(8047):833–838, 2025.

[187] Sajedeh Manzeli, Dmitry Ovchinnikov, Diego Pasquier, Oleg V Yazyev, and Andras Kis. 2d transition metal dichalcogenides. *Nature Reviews Materials*, 2(8):1–15, 2017.

[188] Battulga Munkhbat, Piotr Wróbel, Tomasz J Antosiewicz, and Timur O Shegai. Optical constants of several multilayer transition metal dichalcogenides measured by spectroscopic ellipsometry in the 300–1700 nm range: high index, anisotropy, and hyperbolicity. *ACS photonics*, 9(7):2398–2407, 2022.

[189] F Dybała, MP Polak, J Kopaczek, P Scharoch, Kedi Wu, Sefaattin Tongay, and R Kudrawiec. Pressure coefficients for direct optical transitions in mos2, mose2, ws2, and wse2 crystals and semiconductor to metal transitions. *Scientific reports*, 6(1):26663, 2016.

[190] Ellis Thompson, Emma Manzella, Ethan Murray, Madelaine Pelletier, Jacob Stuligross, Brian C Daly, Seng Huat Lee, and R Redwing. Picosecond laser ultrasonic measurements of interlayer elastic properties of 2h-mose2 and 2h-wse2. *Materials Today Chemistry*, 18:100369, 2020.

[191] Alan dos Santos da Silva and João Henrique Zimnoch dos Santos. Stöber method and its nuances over the years. *Advances in Colloid and Interface Science*, 314:102888, 2023.

[192] Min Jae Shin and Young Jae Shin. Stacking of 2d materials containing a thin layer of hexagonal boron nitride using polycaprolactone. *Journal of the Korean Physical Society*, 78(11):1089–1094, 2021.

[193] Max Born and Emil Wolf. *Principles of optics: electromagnetic theory of propagation, interference, and diffraction of light*. Macmillan, 1959.

[194] R Ziebold, T Witte, M Hübner, and Rainer G Ulbrich. Direct observation of fermi-pressure-driven electron-hole plasma expansion in gaas on a picosecond time scale. *Physical Review B*, 61(24):16610, 2000.

[195] Chunwei Hsu, Riccardo Frisenda, Robert Schmidt, Ashish Arora, Steffen Michaelis De Vasconcellos, Rudolf Bratschitsch, Herre SJ van der Zant, and Andres Castellanos-Gomez. Thickness-dependent refractive index of 1l, 2l, and 3l mos2, mose2, ws2, and wse2. *Advanced optical materials*, 7(13):1900239, 2019.

[196] Vitalyi Gusev. Laser hypersonics in fundamental and applied research. *Acustica*, 82:S–37, 1996.

[197] Sujay B Desai, Gyungseon Seol, Jeong Seuk Kang, Hui Fang, Corsin Battaglia, Rehan Kapadia, Joel W Ager, Jing Guo, and Ali Javey. Strain-induced indirect to direct bandgap transition in multilayer wse2. *Nano letters*, 14(8):4592–4597, 2014.

[198] Garima Gupta and Kausik Majumdar. Fundamental exciton linewidth broadening in monolayer transition metal dichalcogenides. *Physical Review B*, 99(8):085412, 2019.

[199] Thuc T Mai, Kevin F Garrity, Amber McCreary, Joshua Argo, Jeffrey R Simpson, Vicky Doan-Nguyen, Rolando Valdés Aguilar, and Angela R Hight Walker. Magnon-phonon hybridization in 2d antiferromagnet mnpse3. *Science advances*, 7(44):eabj3106, 2021.

[200] Jiaming Luo, Shuyi Li, Zhipeng Ye, Rui Xu, Han Yan, Junjie Zhang, Gaihua Ye, Lebing Chen, Ding Hu, Xiaokun Teng, et al. Evidence for topological magnon–phonon hybridization in a 2d antiferromagnet down to the monolayer limit. *Nano letters*, 23(5):2023–2030, 2023.

[201] AS Salasyuk, AV Rudkovskaya, AP Danilov, BA Glavin, SM Kukhtaruk, M Wang, AW Rushforth, PA Nekludova, SV Sokolov, AA Elistratov, et al. Generation of a localized microwave magnetic field by coherent phonons in a ferromagnetic nanograting. *Physical Review B*, 97(6):060404, 2018.

[202] Albrecht Bartels, Thomas Dekorsy, Heinrich Kurz, and Klaus Köhler. Coherent zone-folded longitudinal acoustic phonons in semiconductor superlattices: excitation and detection. *Physical review letters*, 82(5):1044, 1999.

[203] Aishi Yamamoto, Tomobumi Mishina, Yasuaki Masumoto, and Masaaki Nakayama. Coherent oscillation of zone-folded phonon modes in gaas-alas superlattices. *Physical review letters*, 73(5):740, 1994.

[204] Mini circuits. *SMA connector Datasheet*, 2025.

[205] Juan P Dehollain, JJ Pla, E Siew, KY Tan, AS Dzurak, and A Morello. Nanoscale broadband transmission lines for spin qubit control. *Nanotechnology*, 24(1):015202, 2012.

[206] JV Jäger, AV Scherbakov, BA Glavin, AS Salasyuk, RP Campion, AW Rushforth, DR Yakovlev, AV Akimov, and M Bayer.

Resonant driving of magnetization precession in a ferromagnetic layer by coherent monochromatic phonons. *Physical Review B*, 92(2):020404, 2015.

[207] SI Tamura, DC Hurley, and JP Wolfe. Acoustic-phonon propagation in superlattices. *Physical Review B*, 38(2):1427, 1988.

[208] Ioffe institute. Nsm database.

[209] TD Skinner, H Kurebayashi, D Fang, D Heiss, AC Irvine, AT Hindmarch, M Wang, AW Rushforth, and AJ Ferguson. Enhanced inverse spin-hall effect in ultrathin ferromagnetic/normal metal bilayers. *Applied Physics Letters*, 102(7), 2013.

[210] Manuel Langer, Rodolfo A Gallardo, Tobias Schneider, Sven Stienen, Alejandro Roldán-Molina, Ye Yuan, Kilian Lenz, Jürgen Lindner, Pedro Landeros, and Jürgen Fassbender. Spin-wave modes in transition from a thin film to a full magnonic crystal. *Physical Review B*, 99(2):024426, 2019.

[211] M Langer, K Wagner, T Sebastian, René Hübner, J Grenzer, Yutian Wang, T Kubota, T Schneider, S Stienen, K Lenz, et al. Parameter-free determination of the exchange constant in thin films using magnonic patterning. *Applied Physics Letters*, 108(10), 2016.

[212] M Langer, F Röder, RA Gallardo, T Schneider, S Stienen, Christophe Gatel, R Hübner, L Bischoff, K Lenz, J Lindner, et al. Role of internal demagnetizing field for the dynamics of a surface-modulated magnonic crystal. *Physical Review B*, 95(18):184405, 2017.

[213] SA Cavill, DE Parkes, J Miguel, SS Dhesi, KW Edmonds, RP Campion, and AW Rushforth. Electrical control of magnetic reversal processes in magnetostrictive structures. *Applied Physics Letters*, 102(3), 2013.

[214] C Bayer, SO Demokritov, B Hillebrands, and AN Slavin. Spin-wave wells with multiple states created in small magnetic elements. *Applied Physics Letters*, 82(4):607–609, 2003.

[215] K Yu Guslienko, SO Demokritov, B Hillebrands, and AN Slavin. Effective dipolar boundary conditions for dynamic magnetization in thin magnetic stripes. *Physical Review B*, 66(13):132402, 2002.

[216] RW Chantrell and AN Slavin. Dipolar localization of quantized spin-wave modes in thin rectangular magnetic elements. *Physical Review B*, 68(2):024422, 2003.

[217] BA Kalinikos and AN Slavin. Theory of dipole-exchange spin wave spectrum for ferromagnetic films with mixed exchange boundary conditions. *Journal of Physics C: Solid State Physics*, 19(35):7013, 1986.

[218] BA Kalinikos, MP Kostylev, NV Kozhus, and AN Slavin. The dipole-exchange spin wave spectrum for anisotropic ferromagnetic films with mixed exchange boundary conditions. *Journal of Physics: Condensed Matter*, 2(49):9861, 1990.

[219] C Bayer, J Jorzick, B Hillebrands, SO Demokritov, R Kouba, R Bozinoski, AN Slavin, K Yu Guslienko, DV Berkov, NL Gorn, et al. Spin-wave excitations in finite rectangular elements of ni 80 fe 20. *Physical Review B—Condensed Matter and Materials Physics*, 72(6):064427, 2005.

Appendix

A1. The Phase Change of a Driven Harmonic Oscillator

Beginning with the equation for a damped, driven harmonic oscillator, as is the case in Chapter 2.

$$\frac{d^2x}{dt^2} + \gamma\frac{dx}{dt} + \omega_0^2 x = F_0 sin(\omega t) \tag{97}$$

Here, γ describes the damping, ω_0 is the resonant frequency of the harmonic oscillator, ω is the frequency of the driving force, and F_0 describes the amplitude of the driving force. To solve this equation, we can use an anzats of the form:

$$x(t) = Acos(\omega t + \phi) \tag{98}$$

which is the real part of

$$x(t) = Ae^{i(\omega t+\phi)}. \tag{99}$$

This is a solution of 97. Which is inserted into the differential equation leads to

$$A = \frac{F_0 e^{i\phi}}{(\omega_0^2 - \omega^2) + i\omega\gamma} \tag{100}$$

The denominator of this equation is of the form of a complex number, so A can be rewritten as:

$$A = \frac{F_0 e^{i\phi}}{re^{i\theta}} = \frac{F_0}{r}e^{i(\phi-\theta)}. \tag{101}$$

This requires that $r = \sqrt{(\omega_0^2 - \omega^2)^2 + (b\omega)^2}$ and $\theta = tan^{-1}(b\omega/\omega_0^2 - \omega^2)$. To ensure the amplitude is a real number $\phi = -\theta$. Therefore, when the phase angle ϕ is plotted as a function of ω/ω_0, shown in Figure A1. The phase angle changes the oscillator from being in-phase with the driving force when $\omega << \omega_0$ to being in quadrature at the resonance of the oscillator to finally being out-of-phase when $\omega >> \omega_0$.

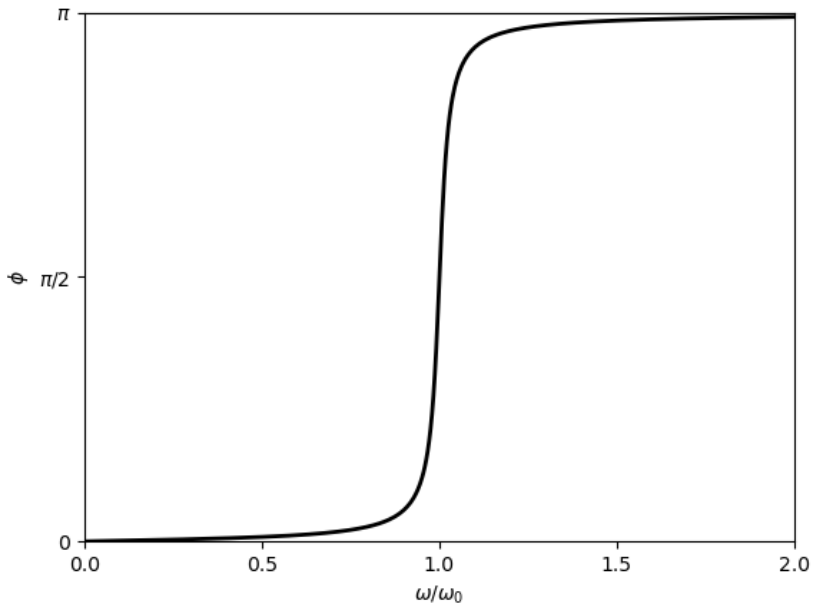


Figure A1: The phase between the driving force and the oscillator. The system begins with the oscillator and the drive being in-phase, and then the phase changes to be out-of-phase when the drive frequency is greater than the oscillator resonant frequency.

A2. Further Microwave Experimental Figures

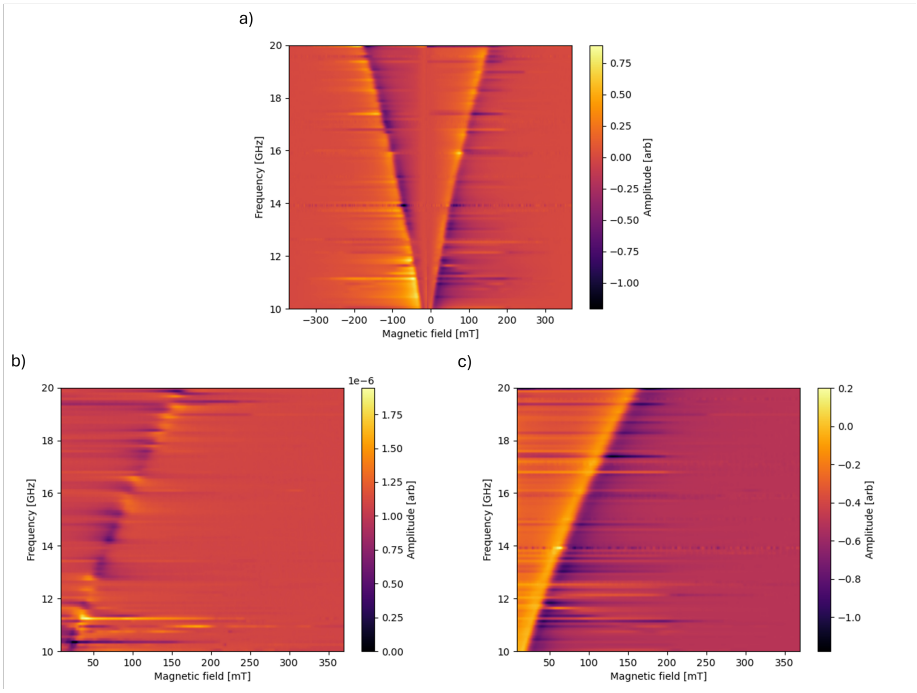


Figure A2: The different analysis methods applied to the data collected for the control device C1, which was produced from sample S2 and the device was fabricated at 90° to the crystal edge. In this case, the field was applied at 45° to the magnetic bar. a) The fitting method results. b) The addition method results. c) The subtraction method results.

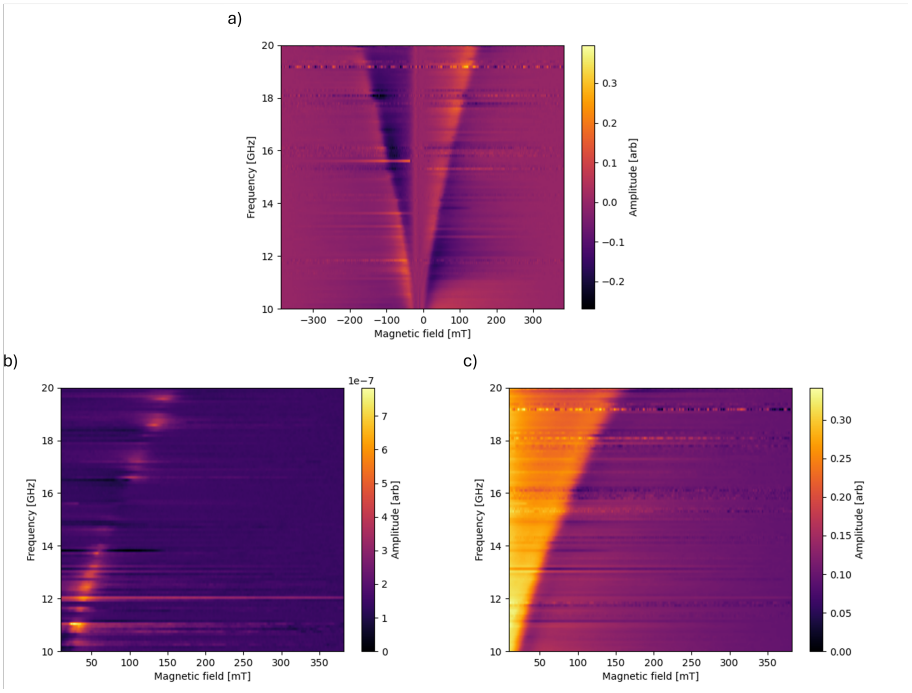


Figure A3: The different analysis methods applied to the data collected for the nanograting device G2, which was produced from sample S2 and the device was fabricated at 90° to the crystal edge. In this case, the field was applied at 45° to the magnetic bar. a) The fitting method results. b) The addition method results. c) The subtraction method results.

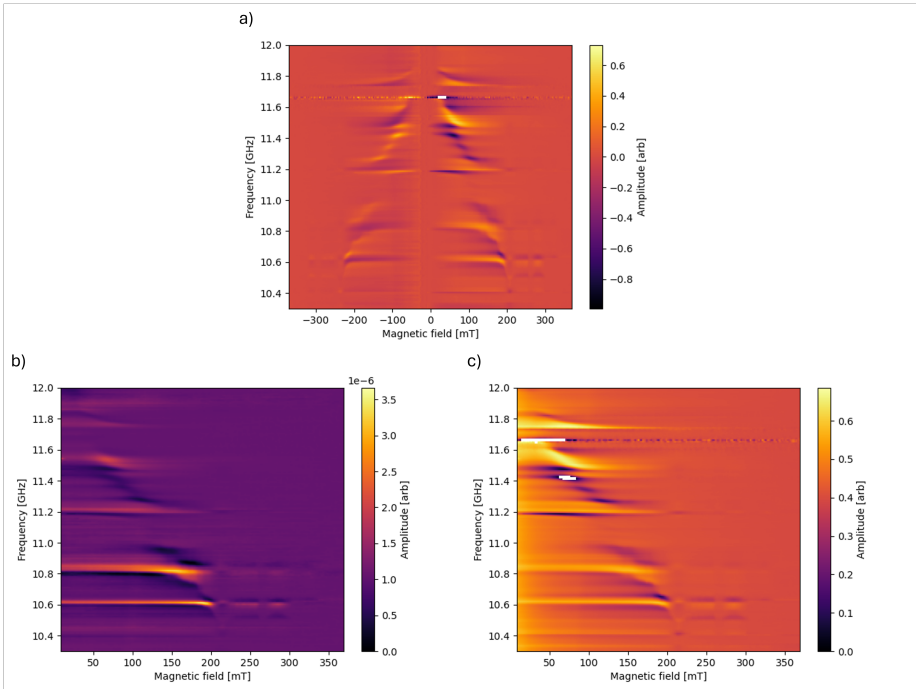


Figure A4: The different analysis methods applied to the data collected for the nanograting device G2, which was produced from sample S2 and the device was fabricated at 90° to the crystal edge. In this case, the field was applied at 90° to the magnetic bar. a) The fitting method results. b) The addition method results. c) The subtraction method results.

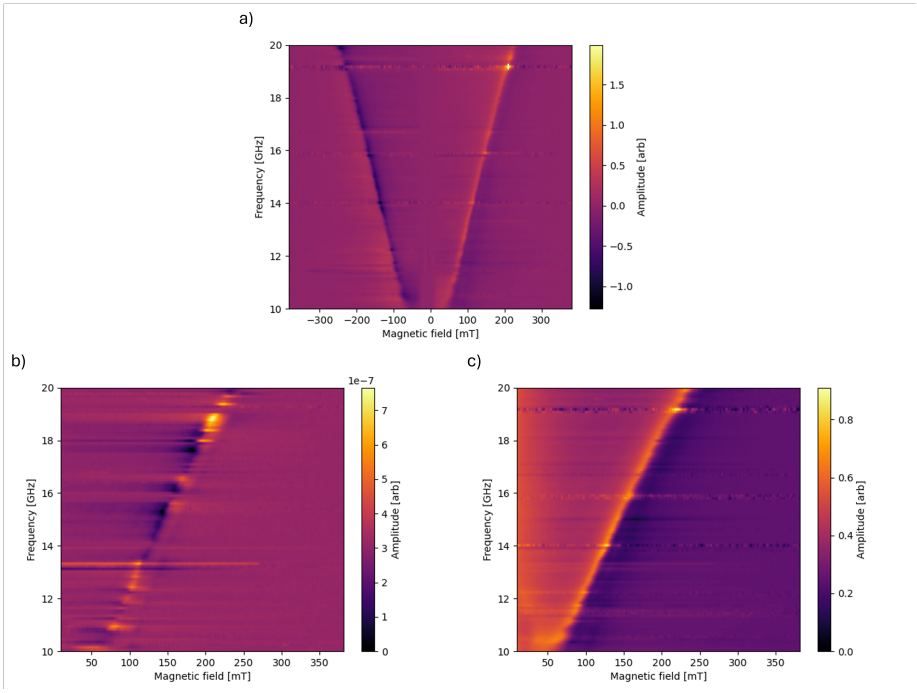


Figure A5: The different analysis methods applied to the data collected for the nanograting device G1, which was produced from sample S2 and the device was fabricated at 45° to the crystal edge. In this case, the field was applied at 45° to the magnetic bar. a) The fitting method results. b) The addition method results. c) The subtraction method results.

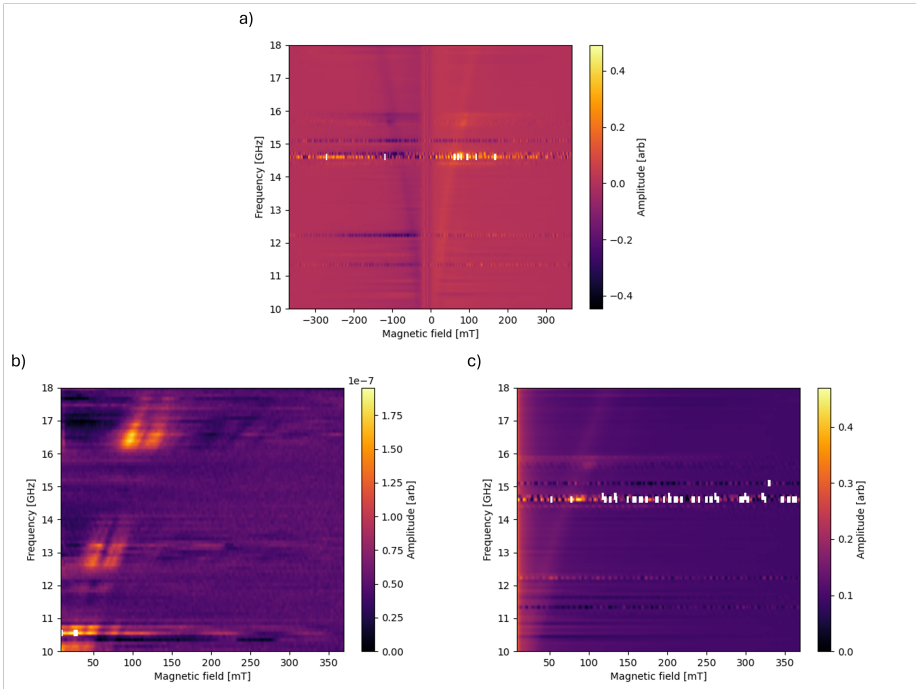


Figure A6: The different analysis methods applied to the data collected for the nanograting device G1, which was produced from sample S2 and the device was fabricated at 45° to the crystal edge. In this case, the field was applied at 90° to the magnetic bar. a) The fitting method results. b) The addition method results. c) The subtraction method results.

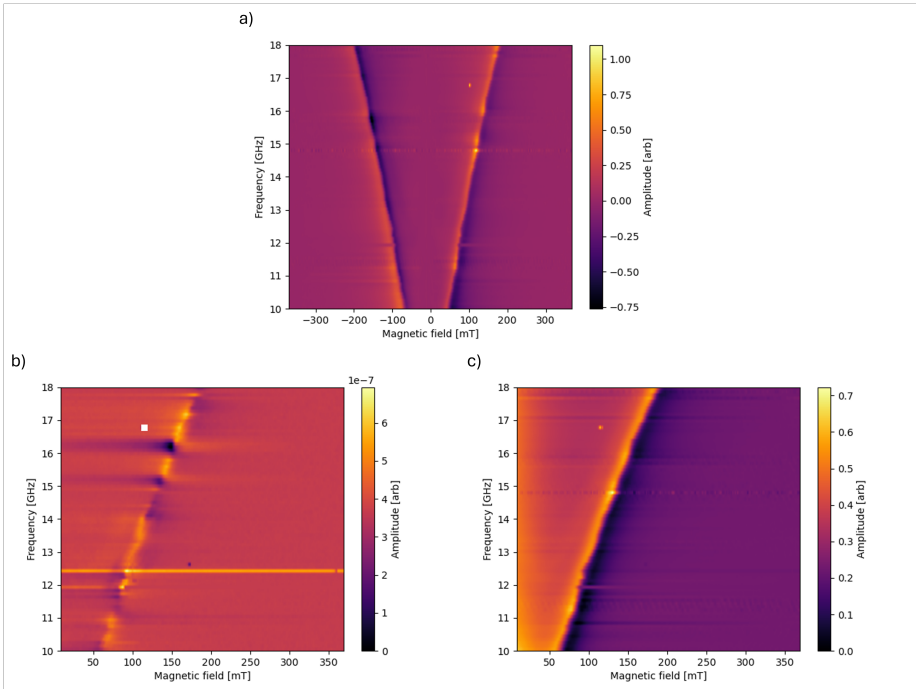


Figure A7: The different analysis methods applied to the data collected for the control device C3, which was produced from sample S1 and the device was fabricated at 45° to the crystal edge. In this case, the field was applied at 45° to the magnetic bar. a) The fitting method results. b) The addition method results. c) The subtraction method results.

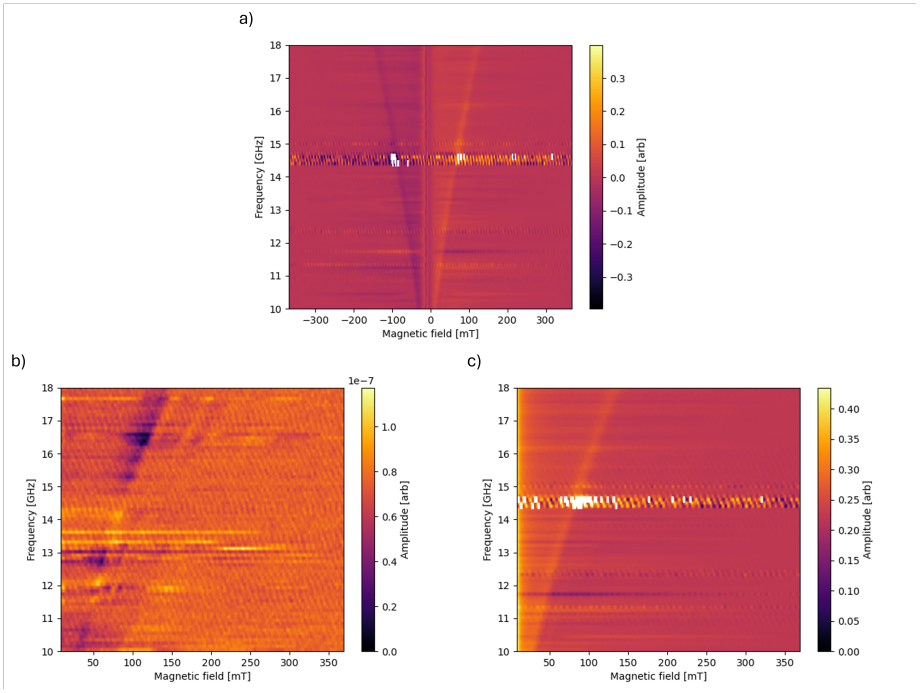


Figure A8: The different analysis methods applied to the data collected for the control device C3, which was produced from sample S1 and the device was fabricated at 45° to the crystal edge. In this case, the field was applied at 90° to the magnetic bar. a) The fitting method results. b) The addition method results. c) The subtraction method results.

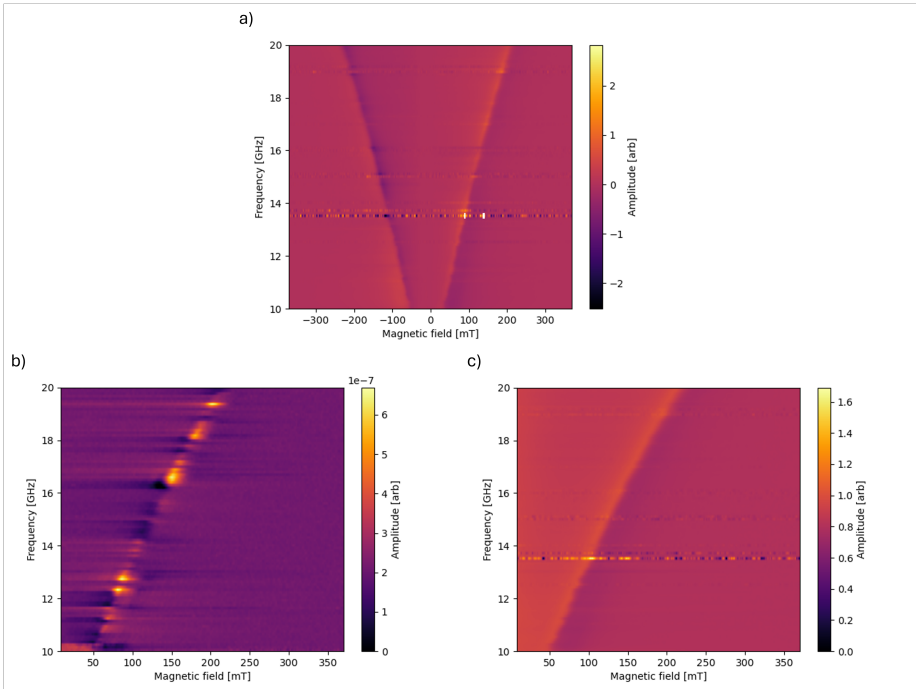


Figure A9: The different analysis methods applied to the data collected for the nanograting device G3, which was produced from sample S1 and the device was fabricated at 45° to the crystal edge. In this case, the field was applied at 45° to the magnetic bar. a) The fitting method results. b) The addition method results. c) The subtraction method results.

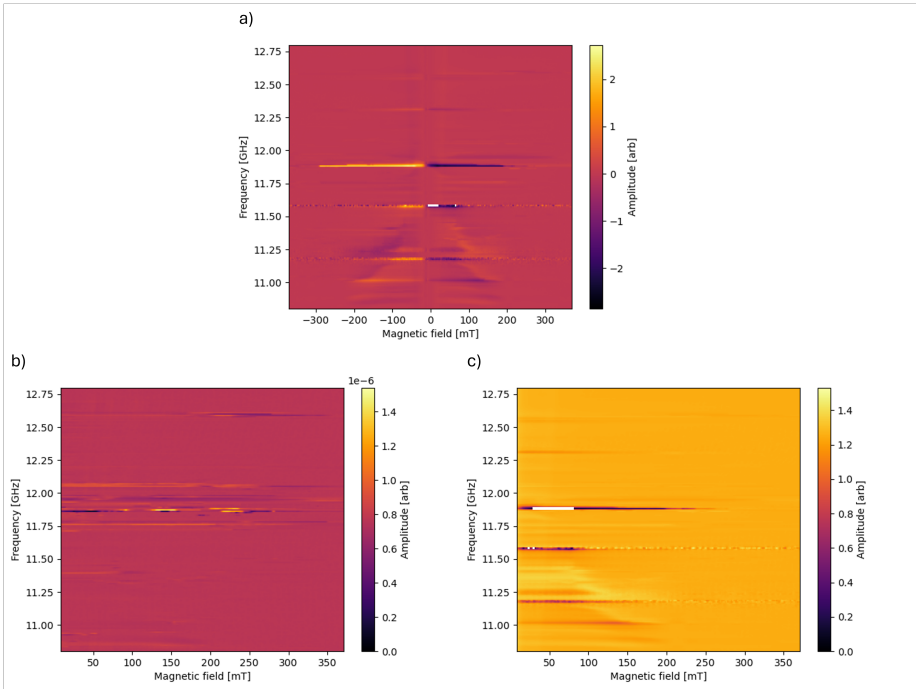


Figure A10: The different analysis methods applied to the data collected for the nanograting device G3, which was produced from sample S2 and the device was fabricated at 45° to the crystal edge. In this case, the field was applied at 90° to the magnetic bar. a) The fitting method results. b) The addition method results. c) The subtraction method results.

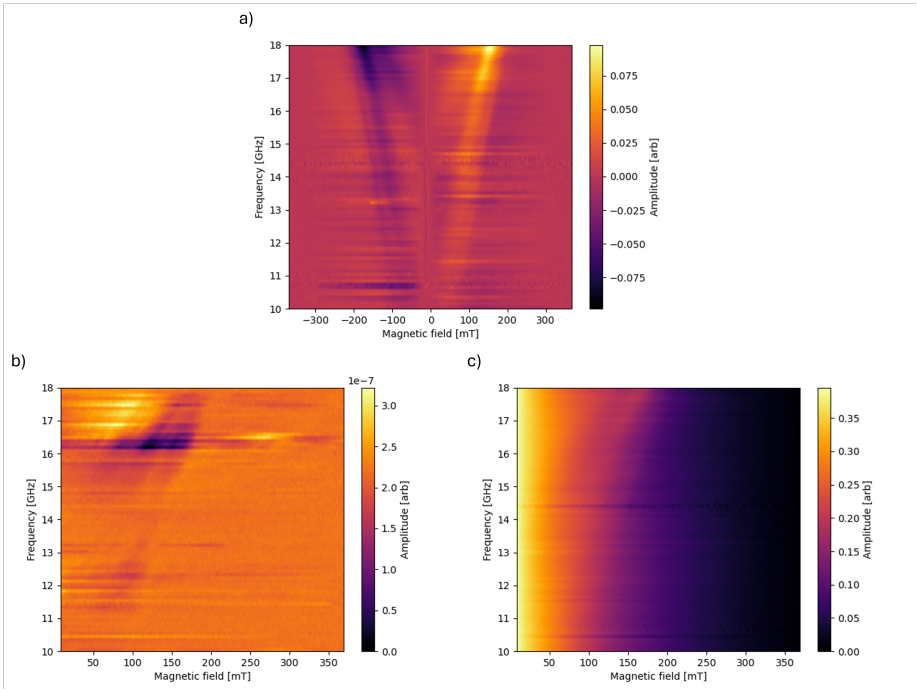


Figure A11: The different analysis methods applied to the data collected for the control device C5, which was produced from sample S4 and the device was fabricated at 45° to the crystal edge. In this case, the field was applied at 45° to the magnetic bar. a) The fitting method results. b) The addition method results. c) The subtraction method results.

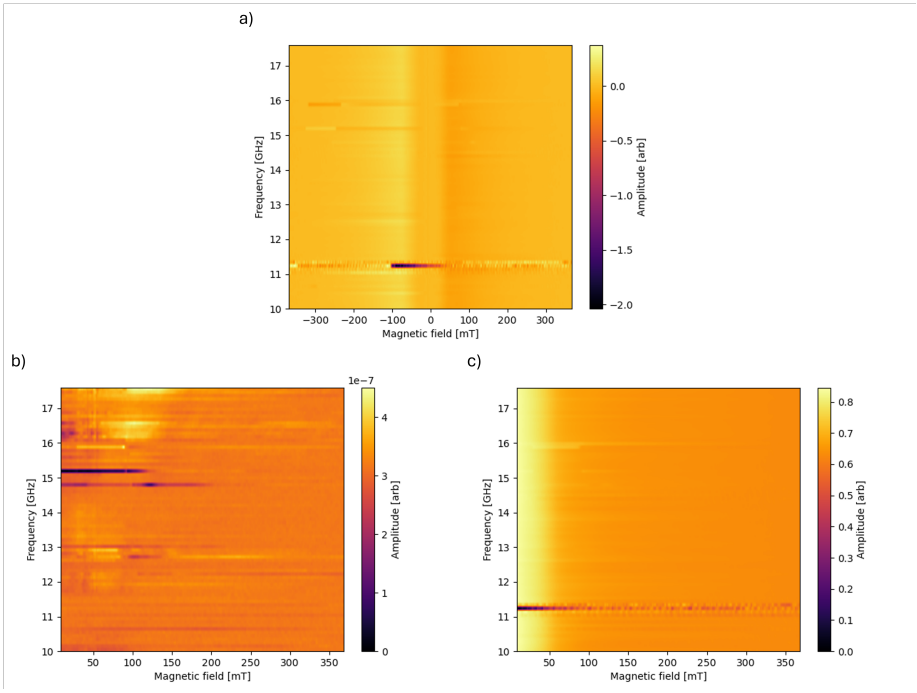


Figure A12: The different analysis methods applied to the data collected for the control device C5, which was produced from sample S4 and the device was fabricated at 45° to the crystal edge. In this case, the field was applied at 90° to the magnetic bar. a) The fitting method results. b) The addition method results. c) The subtraction method results.

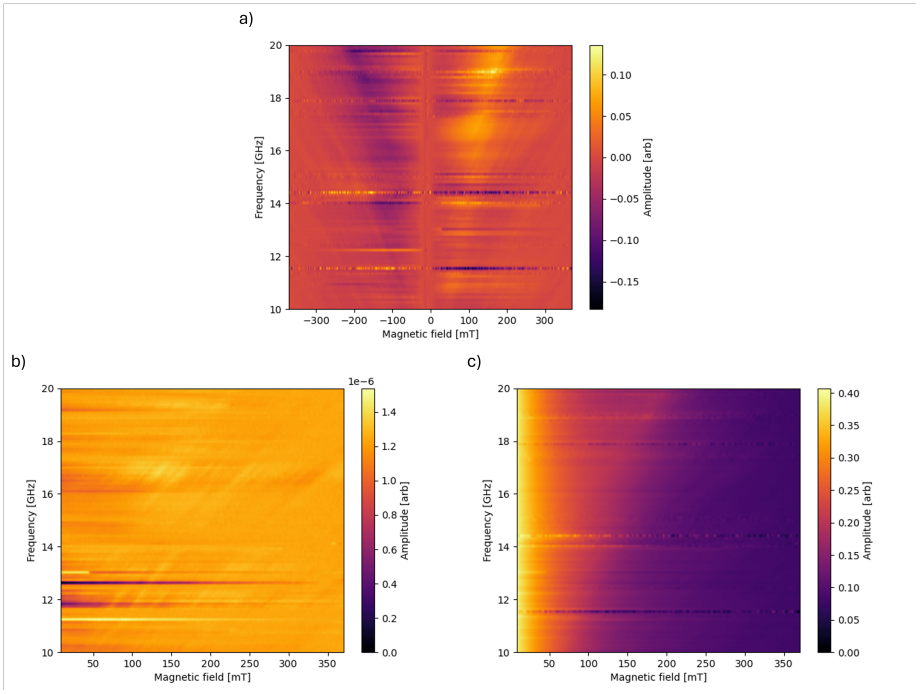


Figure A13: The different analysis methods applied to the data collected for the superlattice device SL1, which was produced from sample S3 and the device was fabricated at 45° to the crystal edge. In this case, the field was applied at 45° to the magnetic bar. a) The fitting method results. b) The addition method results. c) The subtraction method results.

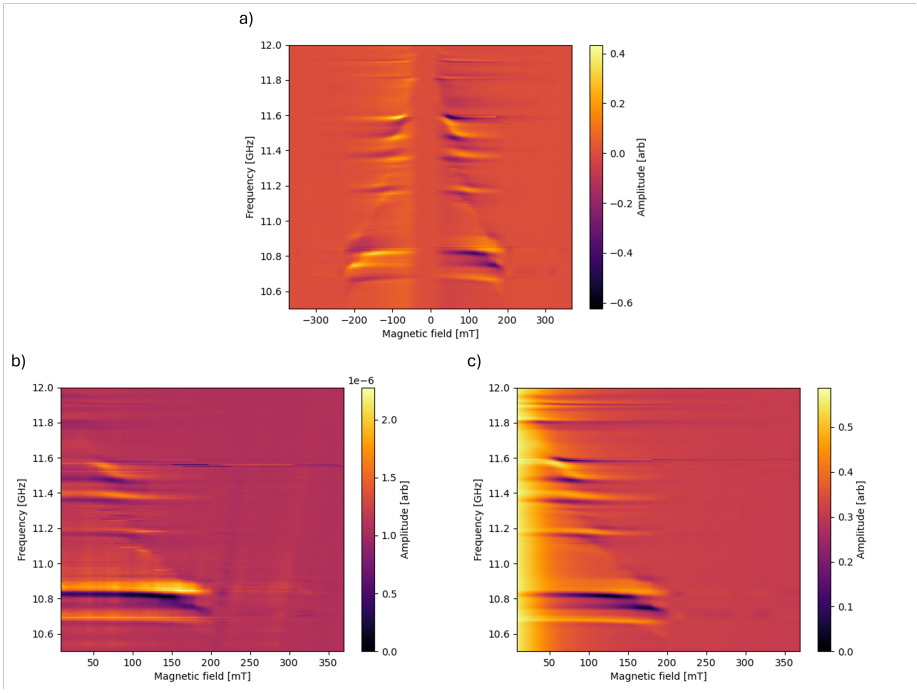


Figure A14: The different analysis methods applied to the data collected for the superlattice device SL1, which was produced from sample S3 and the device was fabricated at 45° to the crystal edge. In this case, the field was applied at 90° to the magnetic bar. a) The fitting method results. b) The addition method results. c) The subtraction method results.

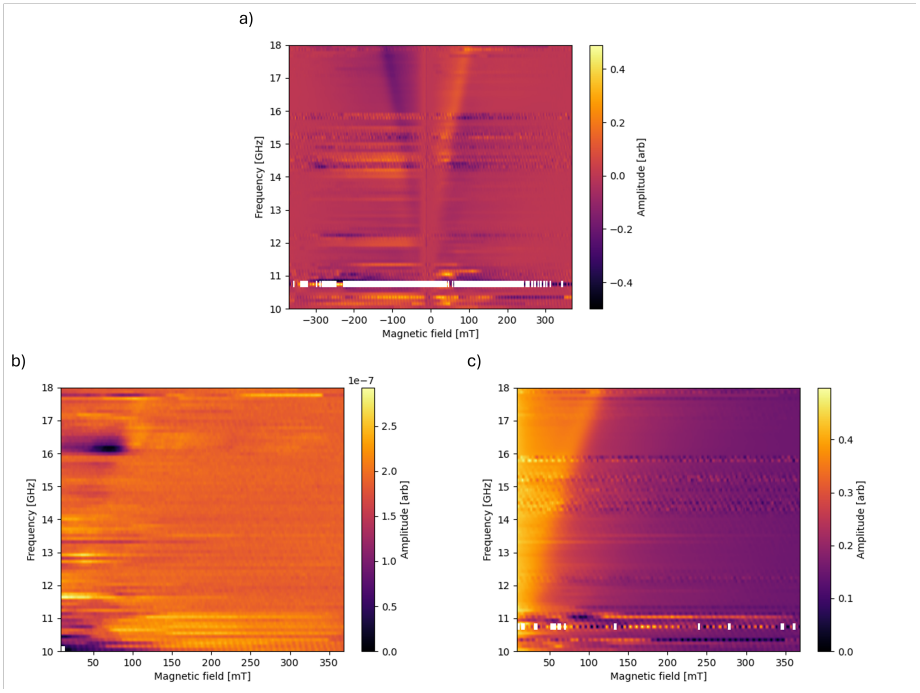


Figure A15: The different analysis methods applied to the data collected for the control device C6, which was produced from sample S4 and the device was fabricated at 90° to the crystal edge. In this case, the field was applied at 45° to the magnetic bar. a) The fitting method results. b) The addition method results. c) The subtraction method results.

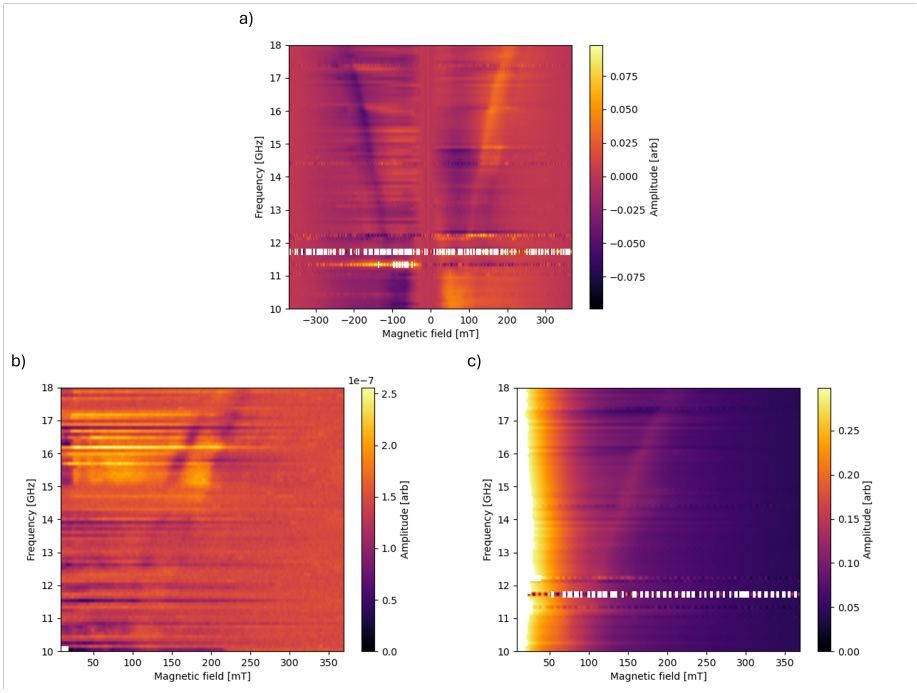


Figure A16: The different analysis methods applied to the data collected for the control device C6, which was produced from sample S4 and the device was fabricated at 90° to the crystal edge. In this case, the field was applied at 90° to the magnetic bar. a) The fitting method results. b) The addition method results. c) The subtraction method results.

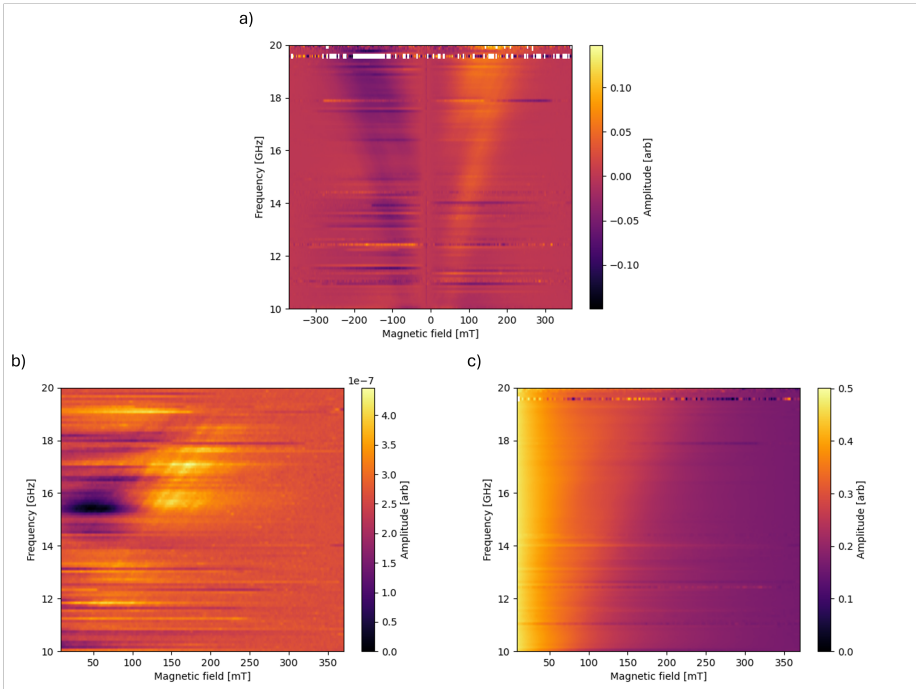


Figure A17: The different analysis methods applied to the data collected for the superlattice device SL2, which was produced from sample S3 and the device was fabricated at 90° to the crystal edge. In this case, the field was applied at 45° to the magnetic bar. a) The fitting method results. b) The addition method results. c) The subtraction method results.

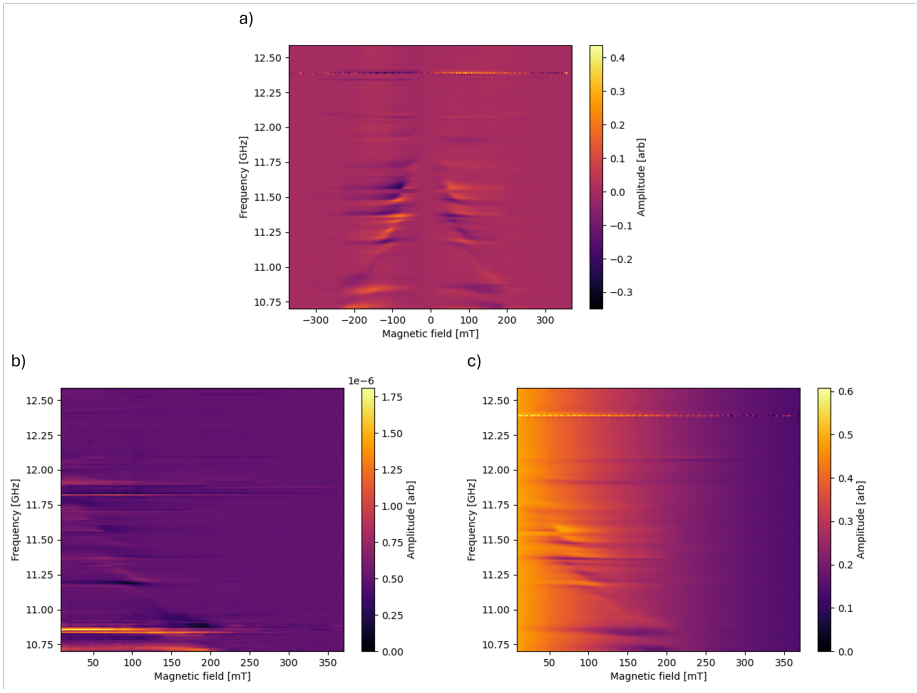


Figure A18: The different analysis methods applied to the data collected for the superlattice device SL2, which was produced from sample S3 and the device was fabricated at 90° to the crystal edge. In this case, the field was applied at 90° to the magnetic bar. a) The fitting method results. b) The addition method results. c) The subtraction method results.

A3. Further Microwave Simulation Figures

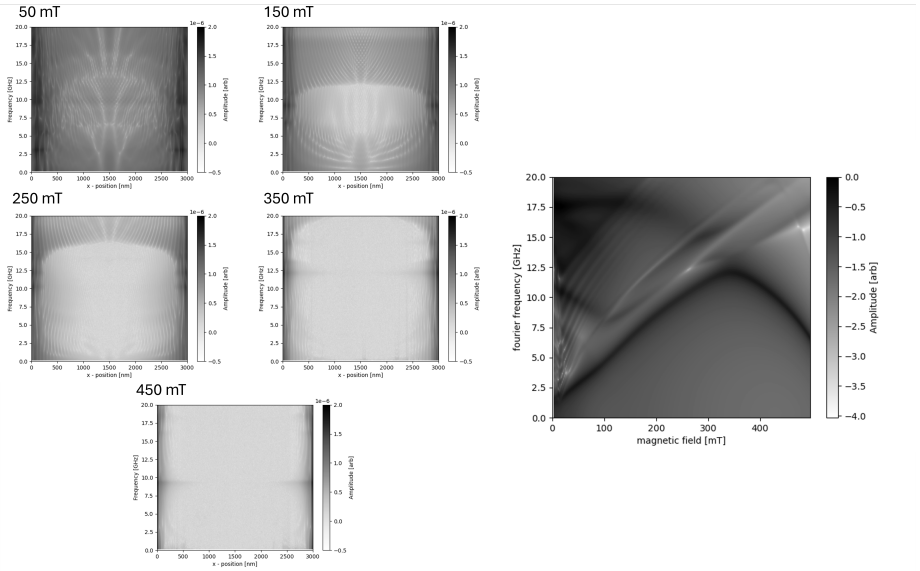


Figure A19: The spatial distribution of the magnon modes across the width of the device, showing the intermediate field values not shown in the main text. The Amplitude of the edge modes is much greater than the centre modes; however, there are examples of modes that extend into the centre region. The structure of the modes in the centre of the bar is clearly complex in nature.